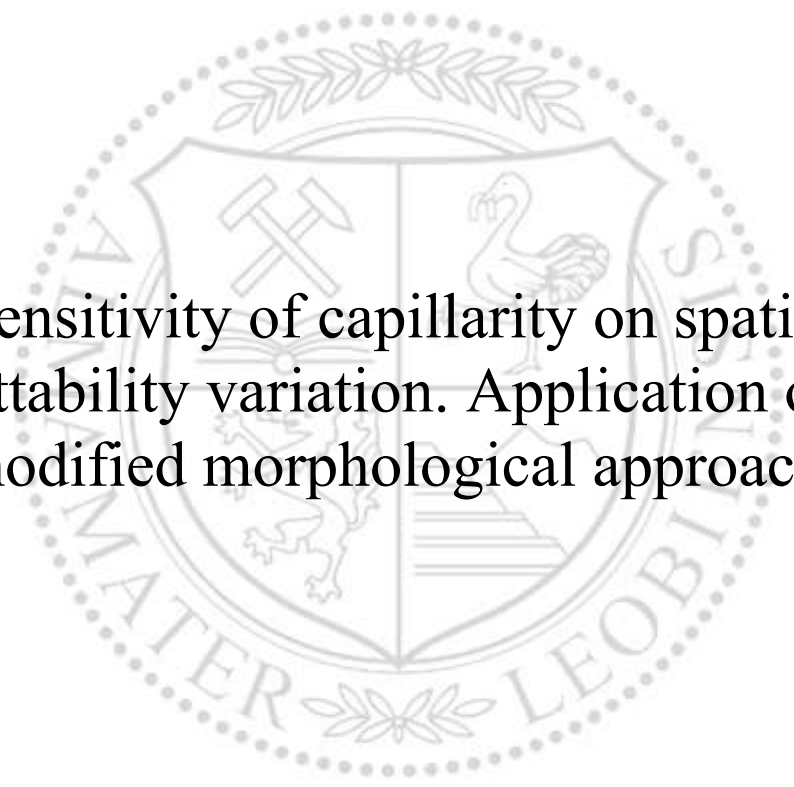




Chair of Reservoir Engineering

Master's Thesis



Sensitivity of capillarity on spatial wettability variation. Application of a modified morphological approach.

Mario Stefan Dragovits, BSc

September 2021



**EIDESSTATTLICHE ERKLÄRUNG**

Ich erkläre an Eides statt, dass ich diese Arbeit selbständig verfasst, andere als die angegebenen Quellen und Hilfsmittel nicht benutzt, und mich auch sonst keiner unerlaubten Hilfsmittel bedient habe.

Ich erkläre, dass ich die Richtlinien des Senats der Montanuniversität Leoben zu "Gute wissenschaftliche Praxis" gelesen, verstanden und befolgt habe.

Weiters erkläre ich, dass die elektronische und gedruckte Version der eingereichten wissenschaftlichen Abschlussarbeit formal und inhaltlich identisch sind.

Datum 22.09.2021

---

Unterschrift Verfasser/in  
Mario Stefan Dragovits

Mario Dragovits

Master Thesis 2021

Supervisor: Univ.-Prof. Dipl.-Phys. Dr.rer.nat. Holger Ott

Co-supervisor: Dipl.-Ing. Pit Arnold

# Sensitivity of capillarity on spatial wettability variation

Application of a modified morphological approach

*To my parents and my beloved Silvia...*

## Declaration

I hereby declare that except where specific reference is made to the work of others, the contents of this dissertation are original and have not been published elsewhere. This dissertation is the outcome of my own work using only cited literature.



Name, 22 September 2021

## Acknowledgments

First, I would like to thank Prof. Holger Ott. Not only for the opportunity to work for you but also for the sincere trust you placed in me from day one. You are not only a decidedly good teacher but also a good person. Thank you for all the discussions and your support throughout my entire master's program.

I also want to thank Pit Arnold. You were always there for me, regardless of whether it was about my studies or not. You have been by my side for years and always share your knowledge with me and give me strength and courage in difficult times, thus I owe you to a large extent why I am where I am today. I thank you from the bottom of my heart for every conversation, every discussion, and every piece of advice you gave me. You introduced me to the field of DRP and thoroughly supported and challenged me. To put it simply, you are not just my mentor, but a true friend and brother.

I would also like to thank all my work and study colleagues. I want to thank Boris Jammerneegg for the training in Python and all the advice and tips for solid use. I would like to thank Bianca Brandstätter for all the countless hours that we have studied together and that have made the master a little easier. I would like to thank Lobel Danicic for all the discussions on GeoDict. Special thanks also go to Martin Tschiedl, Thore Lindemann and Maximilian Hofstätter, and everyone else in our great troop. You have always strengthened my back and at times also gave me the necessary pressure not to lose focus.

Last but not least, I would like to thank my family and my beloved Silvia for always being there for me, for all the opportunities and support, and all the love I get from them.

## Abstract

The field of Digital Rock Physics (DRP) aims to compute fluid displacement processes in rock directly on the imaged rock's pore space, resulting in capillary pressure and relative permeability saturation functions. Therefore, DRP has the potential to replace time-consuming and labor-intensive laboratory SCAL (Special Core Analysis) experiments. Thereby, one of the major targets is to compute those saturation functions in a time and cost-competitive way. In order to achieve a macroscopically representative description, the respective pore-scale fluid distributions must be realistic. A common and computationally attractive method of obtaining these distributions is the morphological approach. However, the applicability of the morphological methods has reached limits with respect to the imbibition saturation range and a realistic description of wettability alteration. Therefore, new innovative solutions are required.

Recently and in collaboration with the software developer, qualitatively new features have been implemented in the commercial simulation toolbox GeoDict. The new features allow to extend the simulation capability from spontaneous to forced imbibition, to introduce multiple contact angles, and contact angle distributions with different spatial correlations. Those features now allow to simulate the total saturation range and to determine uncertainties. The present MSc thesis investigates whether or not those features reflect a physically meaningful behavior. For this purpose, a digital twin of a sandstone sample was exposed to different conditions with regard to the number of contact angles and their associated spatial distribution in each simulation case covered. The results show that this new approach enables the computation of forced imbibition processes, and hence extending the achievable saturation range. On the other hand, the results point out the exerted influence of varying contact angle distribution and spatial variation. The corresponding modifications always introduce an alteration of the prevailing wetting conditions, which in turn is captured correctly within the simulation processes and resulting in computed capillary pressure curves depicting the corresponding trends according to the altered wetting conditions. Ultimately, the results provide information on the most influential parameters of these implementations and show the general trend to the right physical behavior.

## Zusammenfassung

Das Forschungsfeld der „Digital Rock Physics“ (DRP) zielt darauf ab, Flüssigkeitsverdrängungsprozesse innerhalb eines Gesteins direkt auf dem abgelichteten Porenraum dieses Gesteins zu berechnen. Dies wiederum führt zu der Möglichkeit die entsprechenden Sättigungsfunktionen von Kapillardruck und der relativen Permeabilität zu kalkulieren. Somit zeigt das Gebiet der DRP das Potenzial, zeit- und arbeitsintensive SCAL-Experimente (Special Core Analysis) aus dem Labor zu ersetzen. Dabei besteht eines der Hauptziele darin, diese Sättigungsfunktionen zeit- und konkurrenzfähig zu berechnen. Um eine makroskopisch repräsentative Beschreibung zu erreichen, müssen die jeweiligen Fluidverteilungen im Porenbereich realistisch sein. Ein gängiges und rechnerisch attraktives Verfahren zum Erhalten dieser Verteilungen ist der morphologische Ansatz. Da jedoch die Anwendbarkeit der morphologischen Methoden hinsichtlich des Imbibitionssättigungsbereichs und einer realistischen Beschreibung der Benetzbarkeitsänderung an Grenzen stößt, sind neue innovative Lösungen gefragt.

Kürzlich wurden in Zusammenarbeit mit dem Softwareentwickler qualitativ neue Features in die kommerzielle Simulations-Toolbox GeoDict implementiert. Diese neuen Funktionen ermöglichen es zum einen, die Simulationsfähigkeit von spontaner zu erzwungener Imbibition zu erweitern, und zum anderen mehrere Kontaktwinkel und Kontaktwinkelverteilungen mit unterschiedlichen räumlichen Korrelationen einzuführen. Diese Funktionen erlauben es nun, den gesamten Sättigungsbereich zu simulieren und Unsicherheiten zu bestimmen. Die vorliegende Masterarbeit untersucht, ob diese neuen Funktionen ein physikalisch sinnvolles Verhalten widerspiegeln. Um diesen Zweck zu erfüllen, wurde ein digitaler Zwilling einer Sandsteinprobe in jedem untersuchten Simulationsfall unterschiedlichen Bedingungen hinsichtlich der Anzahl der Kontaktwinkel und ihrer zugehörigen räumlichen Verteilung ausgesetzt.

Die Ergebnisse zeigen, dass dieser neue Ansatz die Berechnung von forcierten Imbibitionsprozessen ermöglicht und damit den erreichbaren Sättigungsbereich erweitert. Darüber hinaus geben sie Aufschluss über den ausgeübten Einfluss einer unterschiedlichen Kontaktwinkelverteilung und räumlichen Variation. Die



entsprechenden Modifikationen führen immer zu einer Änderung der vorherrschenden Benetzungsbedingungen, die wiederum in den Simulationsprozessen korrekt erfasst werden, und zur Berechnung von Kapillardruckkurven führen, die die respektiven Trends entsprechend den geänderten Benetzungsbedingungen darstellen. Letztlich geben die Ergebnisse Auskunft über die einflussreichsten Parameter dieser Implementierungen und zeigen den generellen Trend zum richtigen physikalischen Verhalten.



## Table of Contents

|  |           |
|--|-----------|
| <b>Chapter 1: Introduction</b> .....                     | <b>17</b> |
| 1.1 Background and Context .....                         | 17        |
| 1.2 Scope and Objectives .....                           | 19        |
| <b>Chapter 2: Literature Review</b> .....                | <b>21</b> |
| 2.1 Major petrophysical principles .....                 | 21        |
| 2.2 Digital Rock Physics .....                           | 25        |
| 2.3 Saturation dependent simulation .....                | 26        |
| 2.4 The morphological approach .....                     | 27        |
| 2.5 State of the Art .....                               | 30        |
| <b>Chapter 3: Workflow</b> .....                         | <b>33</b> |
| 3.1 GeoDict .....  | 33        |
| 3.2 Distribute Contact Angle (DCA) .....                 | 35        |
| 3.3 Turn Oil Rock Surface to new Materials (TORS) .....  | 37        |
| 3.4 Capillary Pressure Hysteresis (CPH) .....            | 39        |
| 3.5 Surface Area Analysis .....                          | 44        |
| <b>Chapter 4: Results and Discussion</b> .....           | <b>45</b> |
| 4.1 Utilized structure .....                             | 46        |
| 4.2 Case A: Single solid material .....                  | 47        |
| 4.3 Case B: Single to multiple solid materials .....     | 55        |
| 4.4 Case C: Multiple solid materials .....               | 59        |
| 4.5 Case D: Multiple solid materials, differing RS ..... | 66        |
| 4.6 Case E: Distinct spatial separation .....            | 74        |
| <b>Chapter 5: Conclusion</b> .....                       | <b>79</b> |
| 5.1 Summary .....  | 79        |
| 5.2 Future work .....                                    | 81        |
| <b>Chapter 6: References</b> .....                       | <b>83</b> |



## List of Figures

|  |     |
|--|-----|
| Figure 2-1 Contact Angle (CA) between water (WP) and gas (NWP).....  | 22  |
| Figure 2-2 Differing CA in an oil-water system, showing the transition from completely WW (left) to completely OW (right). .....   | 22  |
| Figure 2-3 Capillary pressure curve, showing the typical capillary functions. ....   | 24  |
| Figure 2-4 Visualization of the morphological approach for a single CA case. ....  | 29  |
| Figure 2-5 Visualization of the morphological approach for a multiple CA case. ....  | 30  |
| Figure 3-1 DCA algorithm input parameters.....   | 35  |
| Figure 3-2 Visualization of the DCA process: (left) binary input structure, (right) output structure with one additional solid phase distributed into the preexisting phase. ....            | 36  |
| Figure 3-3 Possible Arrangements: (A) DCA algorithm resulting in 2 solid materials, (B) combining the DCA algorithm with ProcessGeo and LayerGeo to generate 4 solid materials.....          | 36  |
| Figure 3-4 TORS algorithm input parameters. ....   | 37  |
| Figure 3-5 PSD considering 50 % PSC. ....  | 38  |
| Figure 3-6 TORS output: (A) structure after primary Drainage, (B) Structure after spontaneous Imbibition including newly generated OW material (black), resulting from the TORS process..... | 39  |
| Figure 3-7 CPH algorithm input parameters.....   | 40  |
| Figure 3-8 Location of WP and NWP reservoirs and the corresponding invading phase according to the process, defined in the CPH algorithm. ....   | 41  |
| Figure 3-9 CPH algorithm: Resulting capillary pressure curve of the possible hysteresis cycle.....   | 42  |
| Figure 3-10 Pressure drop in the transition from spontaneous to forced imbibition process.....   | 43  |
| Figure 3-11 Spatial alterations of WP and NWP boundary condition reservoirs. ....  | 43  |
| Figure 4-1 Digital twin of the Sandstone sample: (left): only solid material visible (grey), (right): solid material (grey) and water-saturated pore space (blue). ....                      | 46  |
| Figure 4-2 2D representation of the original structure. ....   | 46  |
| Figure 4-3 Case A, Scenario A1, Results. ....  | 48  |
| Figure 4-4 Exemplified wettability index. ....   | 49  |
| Figure 4-5 Case A, Scenario A2, Results. ....  | 51  |
| Figure 4-6 Case A, Scenario A3, Results. ....  | 52  |
| Figure 4-7 Case A, Scenario A4, zoomed-in Results. ....  | 53  |
| Figure 4-8 Utilized structures for Case B. ....  | 55  |
| Figure 4-9 Case B, Scenario B1, Results. ....  | 58  |
| Figure 4-10 Comparison of scenario C1 and A1. ....   | 60  |
| Figure 4-11 Comparison of scenario C2 and A3. ....   | 62  |
| Figure 4-12 Case C, utilized structure before (left) and after (right) the applied TORS algorithm. ....  | 63  |
| Figure 4-13 Comparison of scenario C3 and C2.....  | 65  |
| Figure 4-14 Utilized structures for Case D. ....   | 67  |
| Figure 4-15 Case D, Scenario D1, Results. ....   | 69  |
| Figure 4-16 Case D, Scenario D2, Results. ....   | 71  |
| Figure 4-17 Case D, Scenario D3, Utilized structures.....  | 72  |
| Figure 4-18 Case D, Scenario D3, Results. ....   | 73  |
| Figure 4-19 Case E, utilized structures. ....  | 74  |
| Figure 4-20 Case E, Scenario E1, Results. ....   | 77  |
| Figure 6-1 Step 1.....   | A-1 |
| Figure 6-2 Step 2.....   | A-2 |
| Figure 6-3 Step 3.....   | A-2 |
| Figure 6-4 Influence of PSC value on newly introduced Solid material. ....   | A-5 |

|   |     |
|---|-----|
| Figure 6-5 Case A, Scenario A4, Results, full view. ....        | B-1 |
| Figure 6-6 Case D, Scenario D2, Results on structure D 10.....  | B-2 |
| Figure 6-7 Case D, Scenario D2, Results on structure D 500..... | B-2 |

## List of Tables

|  |     |
|--|-----|
| Table 1 Case A, Scenario A1. ....                                      | 47  |
| Table 2 Wettability indices Scenario A1. ....                          | 49  |
| Table 3 Case A, Scenario A2. ....                                      | 50  |
| Table 4 Occurring changes & WI for Scenario A2. ....                   | 50  |
| Table 5 Case A, Scenario A3. ....                                      | 51  |
| Table 6 Wettability indices Scenario A3. ....                          | 52  |
| Table 7 Case A, Scenario A4. ....                                      | 53  |
| Table 8 Solid material composition for Scenario B. ....                | 56  |
| Table 9 Case B, Scenario B1. ....                                      | 56  |
| Table 10 Occurring changes & WI for Scenario B1. ....                  | 57  |
| Table 11 Case C, Scenario C1. ....                                     | 59  |
| Table 12 Comparison of Scenario A1 & C1. ....                          | 60  |
| Table 13 Case C, Scenario C2. ....                                     | 61  |
| Table 14 Comparison of Scenario A3 & C2. ....                          | 61  |
| Table 15 Case C, Scenario C3. ....                                     | 63  |
| Table 16 Comparison of Scenario C2 & C3. ....                          | 64  |
| Table 17 Case D, DCA input parameters of the utilized structures. .... | 66  |
| Table 18 Case D, Scenario D1. ....                                     | 67  |
| Table 19 Occurring changes & WI for Scenario D1. ....                  | 68  |
| Table 20 Case D, Scenario D2. ....                                     | 69  |
| Table 21 Average difference between the simulation on D10 & D500. .... | 70  |
| Table 22 Case D, Scenario D3. ....                                     | 72  |
| Table 23 Case E, Scenario E2. ....                                     | 75  |
| Table 24 Wettability indices Scenario E1. ....                         | 76  |
| Table 25 Surface Area Analysis, DCA algorithm. ....                    | A-3 |
| Table 26 Surface Area Analysis after TORS, 50 % PSC. ....              | A-4 |
| Table 27 Surface Area Analysis after TORS, varying PSC. ....           | A-5 |





## Abbreviations

|     |                     |
|-----|---------------------|
| WP  | Wetting Phase       |
| NWP | Non-Wetting Phase   |
| CA  | Contact Angle       |
| IFT | Interfacial Tension |
| WW  | Water-wet           |
| OW  | Oil-wet             |
| WI  | Wettability Index   |



# Chapter 1

## Introduction

In the era of digitalization, more and more areas in the petroleum industry increasingly rely on digital tools. Especially in the field of laboratory work, many digital processes are now used, to facilitate and accelerate the determination of material properties and flow behaviors. The computer-based digital rock physics (DRP) revolves around numerous techniques and approaches, based on pore-scale modeling. Aiming to further improve the understanding of fundamental physical principles and to gain insight into micro scale relationships. Among other things, the close relation of capillary pressure and corresponding saturation is subjected to multiple investigations. Thereby, one of the essential targets is to compute multi-phase flow saturation functions in a time and cost-competitive way. However, the efficient computation of functions related to negative capillary pressure, namely the branches of forced imbibition and spontaneous drainage, has repeatedly proven difficult to date. Since the complex nature of the processes can currently only be implemented in a computer program to a limited extend.

### 1.1 Background and Context

To realistically compute multi-phase flow saturation functions, the respective fluid distributions within the porous media, represented by the utilized structure, are a crucial factor. In general, there are two major approaches used to obtain these distributions. On the one hand, the full physics model, which directly computes these distributions on the imaged rock's pore space and thereby relies on the implementation of fundamental physics. The occurring downside is the expensiveness of the related computations, resulting in limited applicability. On the other hand, methods like the Lattice-Boltzmann model (LBM) can lead to an effective reproduction of displacement

processes. In contrast to the full physics model, it is solved by means of the Boltzmann equation rather than Navier-Stokes. Unfortunately, these methods are far too time-consuming to realistically introduce a variation of important petrophysical parameters, hence also possessing limited usage. Contrarily, approaches such as pore network modeling (PNWM) prove to be computationally effective, but rather deal with abstract representations of the pore structure. Thus, rather solving analytical equations than the parent equations like Navier-Stokes and Lattice-Boltzmann.

A widespread method used to also obtain fluid distributions is the morphological approach, introducing a combination of the respective advantages of both. The approach works as the full physics model by utilizing the actual pore space and uses suited computation methods to effectively model the displacement processes. The approach has proven to date its good approximation potential for pore-scale fluid distributions regarding primary drainage and spontaneous imbibition simulations. However, the applicability of the approach has so far met limitations when the aim is to determine the saturation-dependent functions related to negative capillary pressure.

The simulation toolbox GeoDict, used throughout this thesis, also relies on the employment of this approach and has also proven its potential to compute reliable results for primary drainage and spontaneous imbibition. Recently and in collaboration with the software developer, a set of new features has been implemented promising the potential to overcome the current hurdle. On the one hand, those new features provide the possibility to introduce multiple contact angles and contact angle distributions with different spatial correlation. On the other hand, those provide the ability to apply a specific sequence of simulation runs with a specialized set of boundary conditions. As a result, the forced imbibition can be conducted as alleged drainage to enable the process.

Accordingly, a new approach, which combines the morphological procedures of both, imbibition, and drainage, is presented in this thesis. Serving the intention to describe the forced imbibition process for a water flooding scenario. Consequently, this approach is increasing the simulation capabilities and the accessible saturation range. Furthermore, the introduction of varying wetting conditions, based on multiple contact angles, gives the possibility to test whether the approach behaves physically in a reasonable way.

## 1.2 Scope and Objectives

In this thesis, a sensitivity analysis is conducted to check whether the provided set of implementations follow correct physical trends for the extended saturation ranges. More precisely, a digital structure was modified, showing altering wetting conditions through a variation of the contact angle ranges, distributions, and spatial variations. These structure modifications are exposed to different simulation scenarios and conditions to cover a broad range of possibilities and to capture potential uncertainties.

This thesis examines whether this new approach is a practical solution to effectively compute a forced imbibition process. Furthermore, it investigates how the modification of contact angles, and their spatial variation affects the corresponding simulation results.



# Chapter 2

## Literature Review

To get a better understanding of this work, this chapter is giving a summary of major petrophysical principles and is providing an overview of state-of-the-art approaches.

### 2.1 Major petrophysical principles

In the following, the major petrophysical principles all around the capillary pressure functions are described. These descriptions refer to given fundamentals and clarify the terminology used throughout this thesis.

#### 2.1.1 Wettability and contact angle

Wettability displays the tendency of a fluid phase to be in contact with a solid surface in the presence of another fluid phase. In the case of two coexisting immiscible fluids, such as oil and water, the more attracted phase is called the wetting phase (WP), while the other is called the non-wetting phase (NWP). Thereby, the WP fluid determines the corresponding terminology of the environment. Hence, in case water is the WP the environment is termed water-wet (WW), and in case oil is the WP, the appropriate term is oil-wet (OW). The angle at which the WP, surrounded by the NWP, contacts the solid material is known to be the contact angle (CA).

The English physician and physicist Thomas Young laid the foundation for all further research on this field in 1805 with his famous definition of the contact angle and the associated Young's equation. His definition refers to a system in which a drop of liquid, surrounded by gas, sits on a solid surface. He defines the CA to be the angle at the phase boundary between the individual phases (Young, 1805). As this is about liquid and solid phases, the arising tensions at the respective phase boundaries play a

decisive role. Figure 2-1 illustrates the CA ( $\theta$ ) and the related tensions, according to Young's definition.

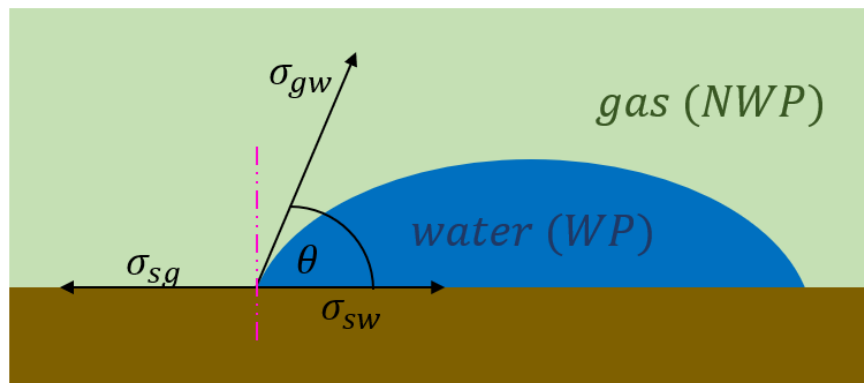


Figure 2-1 Contact Angle (CA) between water (WP) and gas (NWP).

As illustrated in Figure 2-1, wettability can be understood as a balance between interfacial ( $\sigma_{gw}$ ) and surface tensions ( $\sigma_{sg}$ ;  $\sigma_{sw}$ ). The related horizontal balance results in equation (1), known as Young's equation (Young, 1805).

$$\sigma_{sg} = \sigma_{sw} + \sigma_{gw} \cos \theta \quad (1)$$

Rearranging the above equation (1) results in the corresponding contact angle given by equation (2).

$$\cos \theta = \frac{\sigma_{sg} - \sigma_{sw}}{\sigma_{gw}} \quad (2)$$

In the case of a completely WW environment, the water will tend to spread out on the solid surface and displace the oil. Consequently, the oil phase will tend to minimize its surface area to the water by forming a droplet and will bead up, resulting in a CA of zero. For completely oil-wet (OW) conditions this phenomenon occurs vice versa. In case the environment is not considered to be strongly OW or WW, typically the terms intermediate wet (IW) or neutral wet (NW) are used. For such an NW case, the force balance between the solid and the two fluids results in a certain contact angle between the corresponding fluid and the solid surface. Figure 2-2 show these phenomena.

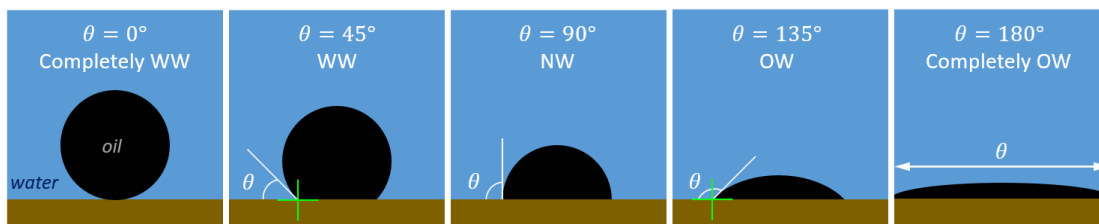


Figure 2-2 Differing CA in an oil-water system, showing the transition from completely WW (left) to completely OW (right).



Consequently, the local wettability state, based on varying CA and its distribution within a porous media, is strongly influencing the displacement behavior and capabilities. According to the local balance of tensions, a displacement process takes place as long as it is favorable. For a porous medium this cannot be observed globally, but more on a pore-by-pore basis (Blunt, 2017).

### 2.1.2 Capillary Pressure

A porous media, saturated with two or more immiscible fluids, is subjected to the influences of capillary forces. The interfacial tension ( $\sigma$ ) between the immiscible fluids is causing a curvature on the interface, and therefore introducing a pressure difference across this interface, generally known as the capillary pressure ( $P_c$ ). However, the extent of capillary pressure also depends on additional factors (Brown, 1951).

One of the most famous equations relating capillary pressure, interfacial forces, and the corresponding curvature is the Young-Laplace equation (3). The equation was derived independently by both Thomas Young and Pierre-Simon Laplace in 1805 and therefore bears the double name to honor both scientists.

The Equation links capillary pressure to the interaction of the interface with a solid surface, by considering the IFT between the two phases, the corresponding contact angle ( $\theta$ ), and the curvature radius of the fluid interface ( $r$ ) (Laplace, 1805; Young, 1805).

$$P_c = \frac{2 \sigma \cos(\theta)}{r} \quad (3)$$

For use in pore-scale physics the above equation, specifically the meaning of ( $r$ ), is subjected to a certain assumption. Typically, the entry points of a pore are deemed with the pore throat radius, by assuming it to be a circular opening with a specific radius. Through this consideration, a limiting criterion is established, allowing the NWP only to enter a pore having a pore throat diameter that is at least equal to ( $r$ ). Thus, equation (3) results in the minimum required pressure for the NWP to enter a pore and to displace the resident WP. Consequently, displacing the WP from any other pore, with a smaller pore throat diameter, is only possible at higher pressure.

### 2.1.3 Drainage and Imbibition

The capillary pressure functions, known as drainage and imbibition, generate a link between capillary pressure and saturation. This link relates the arising capillary pressure between two immiscible fluids in a porous media to the corresponding saturation of the media by those fluids. Thereby, these functions depend on the

process of how the respective saturations are achieved. Typically, the drainage process describes the injection of NWP, hence increasing the NWP saturation while simultaneously decreasing the WP saturation. In contrast to the imbibition, which describes the increase of the WP saturation while decreasing the NWP saturation (Dumore & Schols, 1974).

The typical basic sequence of those capillary functions, which is also utilized in the context of this thesis, known as capillary hysteresis, is the following:

- I. Primary Drainage (displacing NWP, displaced WP)
- II. Spontaneous Imbibition (displacing WP, displaced NWP)
- III. Forced Imbibition
- IV. Spontaneous Drainage
- V. Forced Drainage

Figure 2-3 illustrates these five capillary functions within a capillary pressure curve. Therein indicating whether the respective process is spontaneous or forced, and the corresponding process direction.

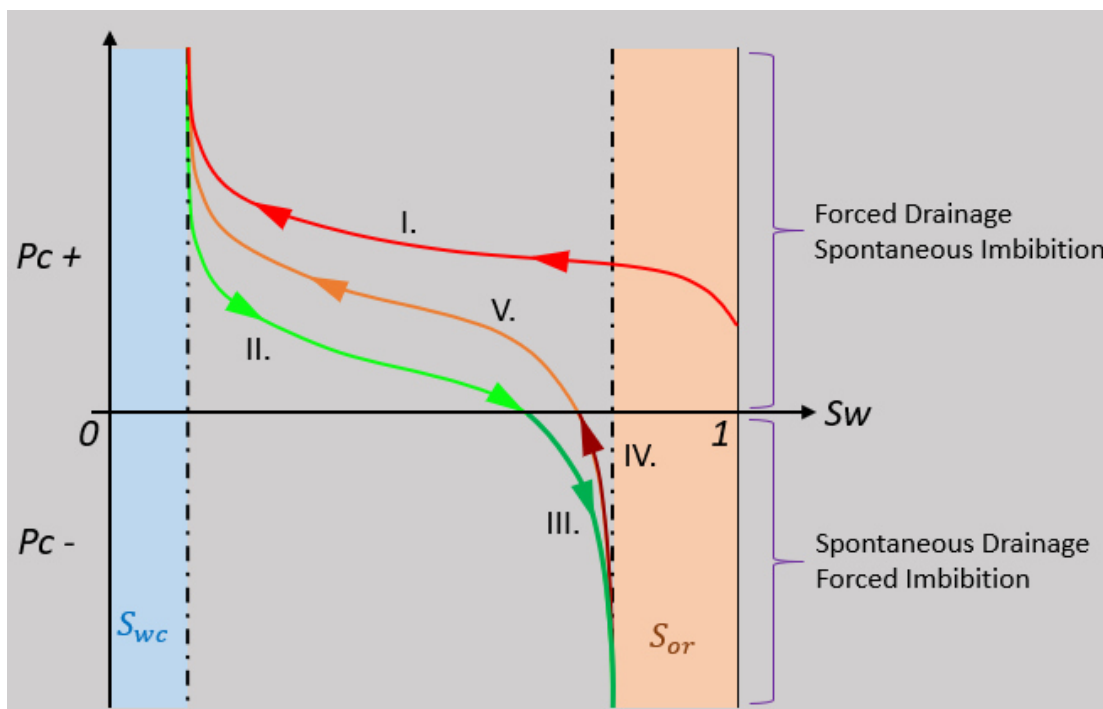


Figure 2-3 Capillary pressure curve, showing the typical capillary functions.

In general, the original initial state of a reservoir is assumed to be WW, hence the pore space is initially filled with water ( $S_w = 1$ ). Through the primary Drainage, oil as the initial NWP is migrating into the reservoir and displaces the resident water, ultimately down to the connate water saturation ( $S_{wc}$ ). This saturation ( $S_{wc}$ ) is the starting point

for the Imbibition. This part is split into two categories, the spontaneous and forced part of the Imbibition, depending on the capillary pressure. So long as  $P_c$  is positive, the WP, in this case water, is sucked into the pore space until the point at which the capillary pressure drops below zero and the process transfers to the forced part. This pressure drop into the negative describes a pressure change resulting in the WP pressure being higher than the NWP pressure, thereby forcing the WP into the reservoir. The forced Imbibition continues to decrease the NWP saturation down to the residual saturation, for oil as NWP the residual oil saturation ( $S_{or}$ ).

This process is followed by the secondary Drainage, consisting out of a spontaneous and forced part, starting at ( $S_{or}$ ). The spontaneous and forced part for the secondary Drainage again depends upon the capillary pressure and conversely follows the same principles as the Imbibition.

## 2.2 Digital Rock Physics

In the era of digitalization, more and more areas in the petroleum industry increasingly rely on digital tools. Many digital methods are now used, especially in the field of laboratory work, since the experimental determination of material properties requires a lot of time and effort. DRP offers the possibility to make these determinations easier and faster and offers additional insights into physics. In addition, it offers the possibility to examine hypothetical scenarios and uncertainties. This computer-related field of work utilizes digital structure models of reservoir rocks gained from modern image generation processes. Such as X-ray computed tomography (CT). DRP is a rapidly developing topic offering a variety of advantages, such as faster core analyzes, repeatability, and the wide range usage of physical simulations. A comprehensive insight into the field of DRP is provided by the team around Andrä in their Digital Rock Physics benchmarks (Andrä et al., 2013). According to them, a typical DRP workflow includes image acquisition and reconstruction, image processing, image segmentation, and simulation on the segmented image.

### 2.2.1 DRP workflow

One of the most common methods of non-destructive pore-scale image acquisition and reconstruction is the micro-scale x-ray computed tomography ( $\mu$ CT). This technique generates a stack of grey scale images that reflect the inner structure of a rock sample. A detailed description of this application in geoscience can be found in the publication by F. Mees and colleagues (Mees et al., 2003).

As a next step, the stack of grey scale images needs to be further processed to minimize the influence of undesired side effects, such as noise or ring artifacts. The numerous types of such effects and their causes are summed up in (Boas & Fleischmann, 2012).

The processing step utilizes various types of filtering techniques to enhance the image quality, such as applying the non-local means technique to reduce occurring noise. This technique is thoroughly described by (Pardo, 2011). After processing the image stack is subjected to the segmentation step, which is basically a recognition and marking process to clearly distinguish between pore space and present material phases within the sample. The core aspect of the segmentation is to apply a specific set of threshold values to the grey scale image histogram to separate the individual phases according to their grey values. A full-scale survey on the related techniques is provided by Sankur (Sankur, 2004), and insight into a multi-level threshold approach can be found in Cuevas paper (Cuevas et al., 2010).

Once the segmentation is done, the image stack shows precisely defined sections and values so that a suited computer program can now create a detailed 3D model of the structure. This digital twin of the rock sample now serves as the basis for the desired numerical simulations. For this thesis, the chair of Reservoir Engineering at the Montanuniversität Leoben provided a digital twin of a sandstone sample, therefore setting the starting point of this work.

## 2.3 Saturation dependent simulation

One of the major targets in DRP is the effective and realistic computation of multi-phase flow saturation functions. To achieve these realistic computations, the respective fluid distributions within the porous media are a crucial factor. Therefore, the close relation of capillary pressure and corresponding saturation is subjected to multiple investigations. The three most essential models associated with this determination are the following:

- I. Lattice-Boltzmann Model (LBM)
- II. Pore Network Model (PNWM)
- III. Morphology Model (MM)

All three modeling techniques rely on different approaches, but the common dominator is the direct relationship between effective hydraulic properties and the rudimentary geometry of the pore space, found in the porous media (Vogel et al., 2005).

The MM is named after the approach with which the respective fluid distributions are determined, the so-called morphological approach (MA). Since the software selected for this thesis uses this approach, it is discussed in more detail in the following section. To gain knowledge on the other mentioned methods, refer to (Shan & Chen, 1993) and (Chen & Doolen, 1998) for the LBM method, and (Fatt, 1956), (Blunt, 2001), and (Wang et al., 2021) for a general overview on the PNWM approach.

## 2.4 The morphological approach

The word morphology comes from Greek and is made up of the words “*morphe*” and “*logos*”, which translates to “*the theory of form*”, thus the name itself already reveals one of the core aspects. This approach is based on the use of a digital rock structure generated by modern imaging techniques (a digital twin). The determination of the individual phase saturation distributions in a multi-phase flow scenario is achieved by direct simulation on the imaged pore space. Hence, considering its underlying geometry.

The morphological approach is a frequently utilized method to determine the saturation conditions in a digital porous medium and as used in this theses is based on the publication of Hilpert and Miller (Hilpert & Miller, 2001). The publication reveals a detailed insight into the approach itself and the corresponding mathematical operations. In the following, an overview of the underlying working principle is provided, and all the following information is related to the corresponding publication.

The development intends to properly simulate a primary drainage curve, where each saturation point on the curve is acquired in a three-step procedure involving:

- a) Morphological erosion of the pore space,
- b) Connected components analysis,
- c) Dilation of the corresponding phase.

The approach employs a digital twin, with the bottom being connected to an NWP reservoir and the top being connected to a WP reservoir.

To determine the saturation distribution of the invading NWP, the algorithm starts with the morphological erosion of the pore space. Followed by a connectivity check of the NWP still connected to the NWP reservoir. Resulting in the actual proportion of the pore space filled with NWP, hence the NWP saturation.

To achieve the desired distribution of WP and NWP, the modeling algorithm is based on the following procedure:

- (1) The whole digital structure is saturated with the WP, and the NWP is in the corresponding reservoir at the bottom of the structure. Capillary pressure, at this point, is zero.
- (2) At the next stage, the capillary pressure is gradually increased. An exploration sphere is implemented, and the respective diameter is calculated via Laplace's equation for a spherical interface:  $p^c = \frac{4\gamma}{D_s}$  (with  $\gamma = \text{IFT}$ ).
- (3) The purpose of the sphere is to check for newly accessible pore space to the NWP. As a criterion, the movement of the NWP must be possible without intersecting the solid material from an NWP saturated position to an adjacent WP saturated or partially saturated position. Each position within the fully NWP saturated part of the structure is subjected to this check until an equilibrium is reached.
- (4) With the equilibrium reached, the NWP saturation is calculated.
- (5) The algorithm calculates for the next point on the curve by starting again at step (2).

This publication is based on a 2D scenario and is one of the first attempts at the method. It serves as a starting point for all further investigations, modifications, and applications in this field.

The application of the morphological approach in modern DRP is primarily utilizing 3D scenarios based on digital twins, which are still based on the same erosion and dilation processes. The following Figure 2-4 and Figure 2-5 display the corresponding procedure, for both single and multiple CA scenarios, using a simplified 2D representation.

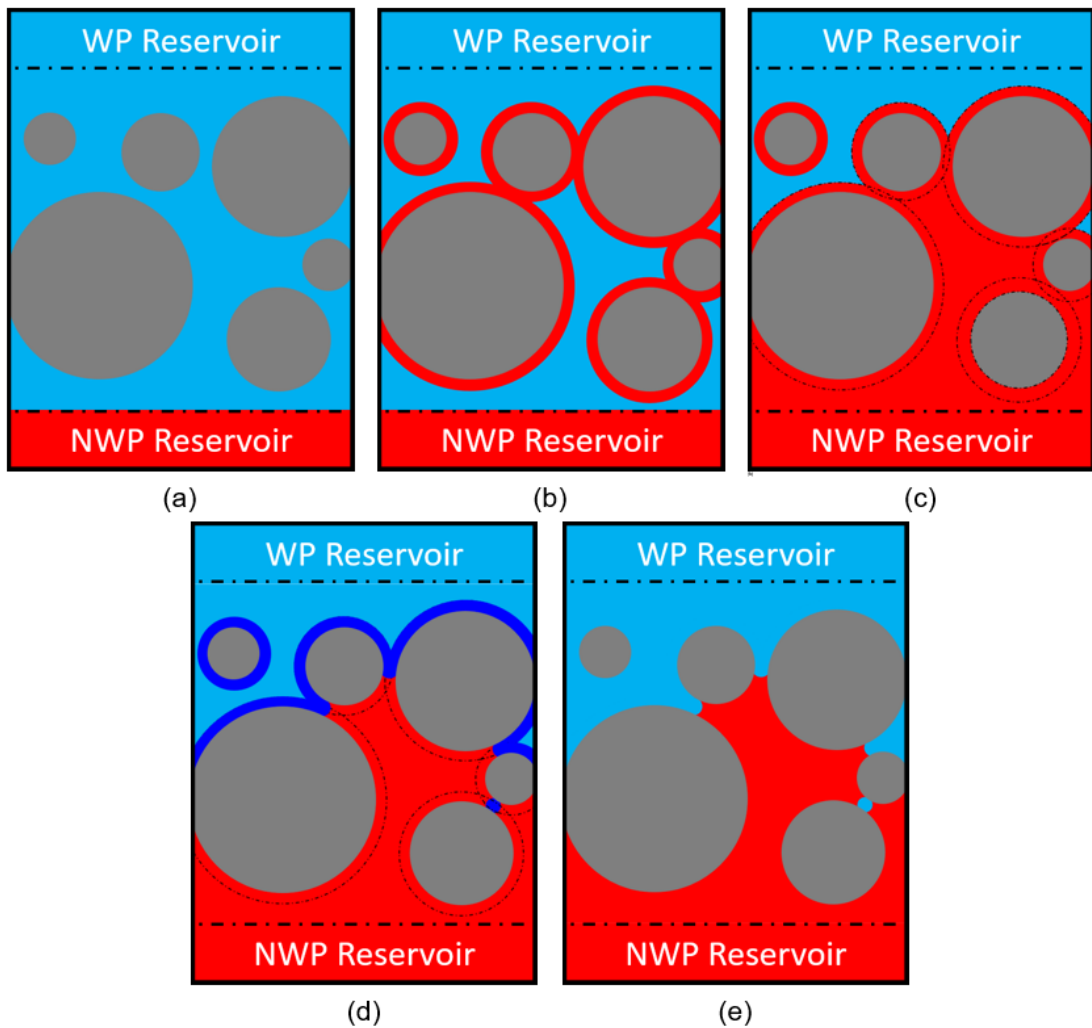
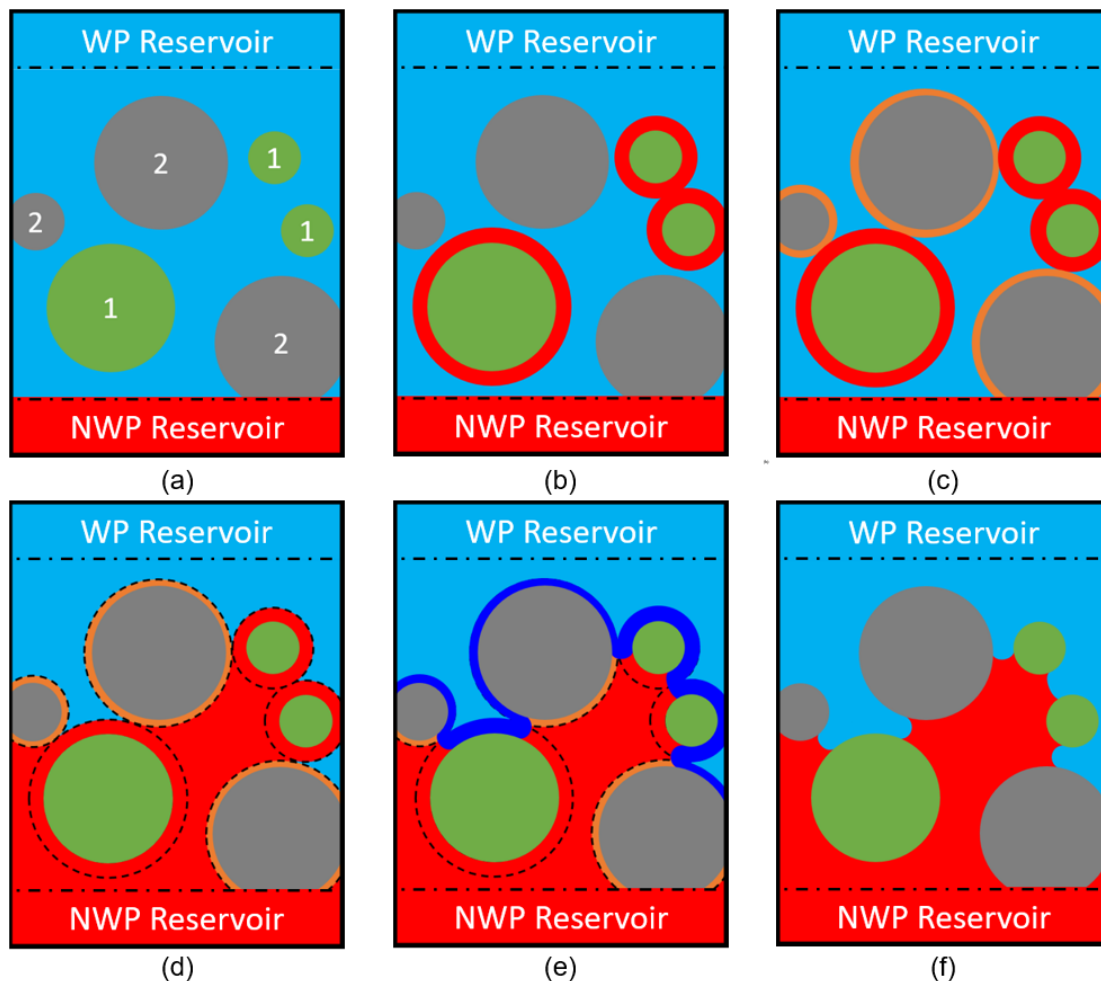


Figure 2-4 Visualization of the morphological approach for a single CA case.

Figure 2-4 exemplifies the method for a scenario with one solid material (gray) and consequently one prevalent CA, as well as the NWP reservoir being connected to the bottom and the WP reservoir to the top. Part (a) illustrates the starting point with the pore space fully saturated with water (blue) and the NWP only being in the corresponding reservoir at the bottom. As a first step (b) the solid material is dilated all around by a specific value ( $r$ ), illustrated by the (red) circles. For a 3D scenario, these circles must be understood as spheres. The dilation step is followed by a connectivity check (c) to determine the amount of invading NWP still connected to the NWP reservoir. The movement criterion here is that the invading phase cannot cross the intersections introduced by the dilation step, to ensure the connection to the NWP reservoir. As the last step, the pore space is eroded by the same value ( $r$ ) as the dilation before (d). Since this erosion relates to the entire pore space, major intersection points in narrow spots can introduce residuals.

This last step results in the proportion pore space filled with NWP, visualized in (e).

The procedure for a scenario with multiple CA, hence multiple solid materials, follows mainly the same principles. Such a scenario is exemplified in *Figure 2-5*, for a simple case of two prevalent solid materials.



*Figure 2-5 Visualization of the morphological approach for a multiple CA case.*

Part (a) displays the starting point of the method with the water-saturated pore space (blue) and the two individual solid materials (green [1], grey [2]). As a difference to the single CA scenario, the dilation step is now conducted first for all of material 1 by the value ( $r$ ) shown in (b), and then for all of material 2 by  $(r) \times \cos(\theta)$  shown in (c). The connectivity check (d) and erosion step (e) follow the same principle as previously described and result in the final proportion of pore space filled with NWP (f).

## 2.5 State of the Art

The computation of multi-phase flow saturation functions is a crucial area of investigation in the field of DRP. Much has happened in this field over the last decades and with increased computational power and efficiency, more and more promising



methods and corresponding results are available. However, there are always limits to this research, both in the computational area and in the correct, or believed to be correct, implementation of the underlying physical processes. The already mentioned work of Hilpert and Miller (Hilpert & Miller, 2001) shows that the morphological approach is particularly suitable for modeling quasi-static drainage scenarios. Their corresponding simulation data is in good agreement with experimental data. In comparison to the LBM approach, their model is cost-competitive, requires less memory and CPU time, and can handle larger domains. On the downside is the restriction to quasi-static conditions and the limitation to a constant contact angle introducing a completely WW scenario.

In addition, a study on capillary hysteresis for both LBM and MA (Ahrenholz et al., 2008), underlines the suitability of MA in regard to primary and secondary drainage simulations. Their results show good data agreement, but also state deviations for the first imbibition. These deviations exist not only between the two approaches and the comparison with experimental data but also with data collected by (Pan et al., 2004), who also investigate two-phase flow in porous media using the LBM approach. Especially the structural element of MA for the imbibition branch is complicated, thus leading to considerable changes. Previous studies focusing on capillary-viscous flow simulations, which are very computationally intensive, again emphasize a reasonable agreement for both drainage and imbibition simulations on a digital twin (D. Koroteev et al., 2014; Ferrari & Lunati, 2013; Vogel et al., 2005).

A paper focusing on quasi-static simulation (Berg et al., 2016), which is less computationally intensive, states that MA provides a good approximation of pore-scale fluid distribution for drainage simulations, but not for imbibition. Since the quasi-static morphological approaches cannot predict the corresponding distribution of the pore-scale saturation for imbibition. Another previous study (Hussain et al., 2014) using the MA method to determine fluid distribution on the pore scale in combination with quasi-static flow simulations gives results in good agreement with measurements on the Darcy scale. An interesting study by the team around Schulz (Schulz et al., 2015) presents an extension to the MA by implementing a spatial distribution of CA. The implementation of multiple CA results in the ability also to cover not completely WW scenarios, and their modification shows no significant influence on computational effects. Their results show that the capillary pressure is scaled as a function of CA, by  $1/\cos\theta$ , which additionally confirms a proposal from a previously conducted inquiry again by Schulz (Schulz et al., 2007). However, this investigation is limited to 2D scenarios but explicitly states that an application for a 3D case is roughly the same.



# Chapter 3

## Workflow

This section provides a more detailed insight into the simulation toolbox GeoDict and the working principle of the three newly implemented features. It is important to understand the underlying mechanisms enabled by them, their specific introduced nomenclature, and the way they are used throughout this thesis.

### 3.1 GeoDict

The simulation toolbox GeoDict from the Math2Market GmbH offers various modules that enable a wide range of simulations in the field of DRP. For this thesis, the computation of the capillary pressure curves is of particular interest. The SatuDict module and the corresponding extensions, which apply the morphological approach described in section 2.4, promise a potential solution to the topic.

#### 3.1.1 SatuDict

This thesis is based on the simulations conducted with the SatuDict module and the three newly implemented extensions. This section provides a short overview of the underlying working principles. All the following Information refers to the SatuDict User Guide (Math2Market GmbH).

One of the basic processes within the SatuDict module is the computation of capillary pressure curves on a digital twin. Thereby, the module applies the pore morphological approach to determine how two different fluid phases distribute within the porous media. More precisely, the module computes the stationary distribution of WP and NWP at a particular capillary pressure.

The applicability depends upon three assumptions:

- I. Negligibility of gravitational and viscous forces, compared to capillary forces.
- II. Existence of well-defined CA's between the solid surfaces and phase boundaries, hence a homogeneous material.
- III. A two-phase system.

A system meeting the three criteria is reducing the given scenario to a purely geometrical task. Thereby, simply expressing the accessible pore space for the NWP according to the Young- Laplace equation in the following form:

$$r = \frac{2\sigma}{P_c} \cos \alpha$$

With  $\sigma$  being the interfacial tension,  $\alpha$  the contact angle,  $r$  the minimum radius, and  $P_c$  the capillary pressure. The SatuDict module can compute two main types of displacement processes:

**Drainage:** This process is defined as an invasion of the NWP which displaces the WP. Thereby, a pore is only accessible to the NWP if the capillary pressure reaches or exceeds the threshold pressure, which is defined by the pore throat. In each step it is checked which pores are accessible to the NWP according to the current capillary pressure. As soon as no more pores are accessible, the pressure is increased to overcome the next smaller pore throats.

**Imbibition:** This process is defined as an invasion of the WP that displaces the NWP. The imbibition starts at the last step of drainage, and thus at the last reached pressure and saturation. Thereby the displacement starts with the small pores first.

The final distributions of WP and NWP for these two processes depend heavily on the prevailing pore and pore throat size distributions within the structure. Furthermore, a phase is considered as residual when disconnected from the respective reservoir.

For a capillary pressure simulation in SatuDict, four main groups of parameters need to be specified:

- a. Saturation Experiment: Defining whether drainage or imbibition is simulated.
- b. Constituent materials: Defining the material properties of the existing phases, in terms of IFT, CA, and type of WP and NWP.
- c. Boundary conditions: Defining the locations of the WP and NWP reservoirs.
- d. Solver parameters: Parameters for the numerical simulation, such as the interface step size. Which specifies the allowed movement of the invading interface within one simulation step.

### 3.1.2 SatuDict extension

SatuDict is suitable to simulate primary Drainage and spontaneous Imbibition scenarios. However, dealing with the forced part of a imbibition and the spontaneous part of a drainage is more complex. To overcome this hurdle, Math2Market provides a specific set of implementations. These three new algorithms enable the effective simulation of a forced Imbibition and spontaneous Drainage and allow a variation of wetting conditions within the system. Since those implementations are of significant importance to this thesis, they are described in detail in the following sections.

## 3.2 Distribute Contact Angle (DCA)

The DCA algorithm enables CA distributions within a single solid without changing the pore structure. This algorithm utilizes a binary input structure and distributes sub-regions into the preexisting model as a new material phase. The input structure must fulfill a specific arrangement of constituent materials, where Material ID 00 is defined as pore space, and Material ID 01 as solid material. Hence, the resulting structure, obtained by the DCA algorithm, consists out of three materials. Material ID 00 still being the pore space, Material ID 01 being the remaining part of the preexisting solid material, and Material ID 02 being the newly introduced solid material.

The extend of these new subregions is based on a gaussian distribution, with the implemented value following the typical bell shape. Correspondingly the resulting length and diameter of the introduced gaussian fields cluster around the specified value but may vary according to standard deviation.

To cover different options of material arrangements, this algorithm comes along with four adjustable parameters, shown in Figure 3-1.

|   |                                   |
|---|-----------------------------------|
| Desired Oil-Wet Region Size / (m)             | <input type="text" value="3e-5"/> |
| Desired Oil-Wet Solid Volume Percentage / (%) | <input type="text" value="25"/>   |
| New Material ID                               | <input type="text" value="02"/>   |
| Random Seed                                   | <input type="text" value="42"/>   |

Figure 3-1 DCA algorithm input parameters.

The “*Desired Oil-Wet Region Size*” determines the overall extent of the generated Gaussian fields, which form the basis of the new material. Those Gaussian Fields are the introduced sub-regions where the approximate radius equals the entered value. Adjusting the “*Desired Oil-Wet Solid Volume Percentage*” sets the volumetric amount of the new implemented material dependent on the preexisting solid material.

The “*New Material ID*” specifies the assigned Material ID for the new material. The “*Random Seed*” produces different sequences of random numbers, ultimately generating different realizations of a specified structure.

Figure 3-2 exemplifies this procedure on the example of implementing 50 % new solid material with a desired oil-wet region-size of 100  $\mu\text{m}$  and a random seed of 42. Thereby the left image represents the binary input structure, and the right image displays the output structure, including the newly generated material [Solid 2 (new)].

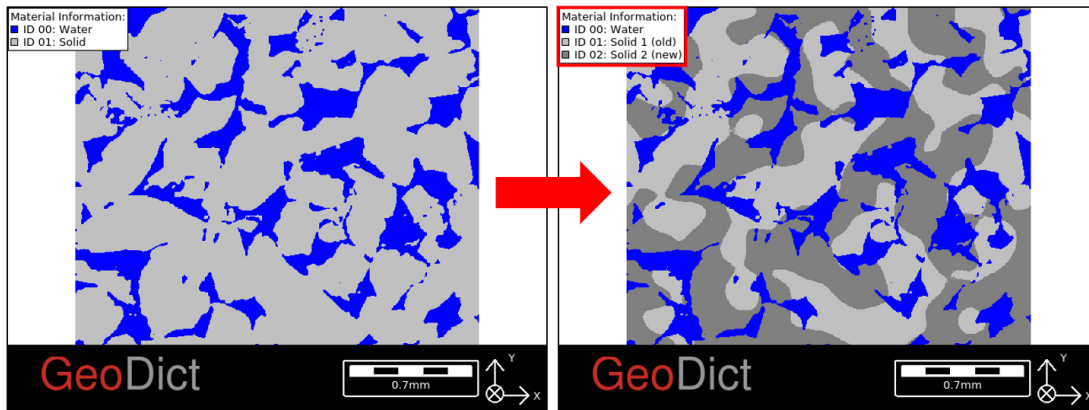


Figure 3-2 Visualization of the DCA process: (left) binary input structure, (right) output structure with one additional solid phase distributed into the preexisting phase.

When using the DCA algorithm in combination with the GeoDict Modules ProcessGeo and LayerGeo, it is possible to generate a structure consisting out of up to four solid materials. The corresponding results for both a case with 2 solid materials (A) and 4 solid materials (B) are shown in Figure 3-3.

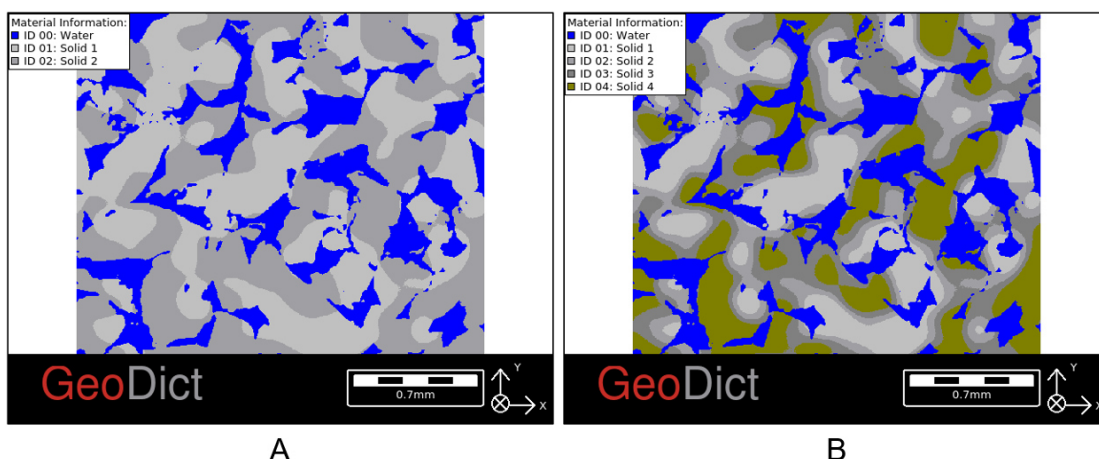


Figure 3-3 Possible Arrangements: (A) DCA algorithm resulting in 2 solid materials, (B) combining the DCA algorithm with ProcessGeo and LayerGeo to generate 4 solid materials.

Depending on how the individual parameters are set it is possible to create a specific transitioning sequence among the newly generated solid materials. The example

shown in the right part of Figure 3-3 represents a smooth transition from the first solid material (ID 01) to the fourth solid material (ID 04). Each solid material contacts only one other solid material. When altering region size and random seed, the combination results in different distributions of the individual solid materials.

A detailed description of how combining the DCA algorithm with the two other GeoDict modules which allow the implementation of up to four solid materials with a smooth transition is provided in appendix section A.1.

### 3.3 Turn Oil Rock Surface to new Materials (TORS)

The forced Imbibition can only take place if the solid materials contain both WW and OW regions. To establish the existence of both wetting conditions, this TORS algorithm is applied before the spontaneous imbibition, when the structure is mainly saturated with oil (NWP).

This algorithm determines at which points the oil is in contact with the solid material and generates precisely at these points a new solid material. This new material is assigned with an also adjustable CA. Throughout this thesis, this CA is referred to as the turning CA, which is above  $90^\circ$  to establish the OW condition. Figure 3-4 shows the input parameters of the TORS algorithm.

Figure 3-4 TORS algorithm input parameters.

To determine the contact points between the respective phases and the solid material, the WP and NWP fluids must first be defined in the “Fluids” section. Here it is possible to use GeoDict’s material database to cover different scenarios with different fluid phases. For the simplest approach, a water-oil system should satisfy the purpose and it the one used throughout this thesis.

Depending on the simulated scenario, based on the number of preexisting solid materials in the used structure (1 solid material, or up to 4 solid materials), there are two possibilities. Either the TORS algorithm generates one new solid phase for all oil-

solid interfaces with one assigned CA or up to four individual new solid phases each with its own assigned CA.

The final adjustment limits the volume of pore space considered for this oil-solid contact conversions. This limitation is based on a pore size distribution (PSD) of the entire structure and sets the specified value as a threshold value over the distribution. Consequently, setting the “*Volume of pore space considered*” (PSC) value to (X), implies that only the defined (X %) of the pore space is considered for generating the new surface contact material. Figure 3-5 illustrates this process on the example of 50 % PSC on the PSD of the utilized sandstone structure.

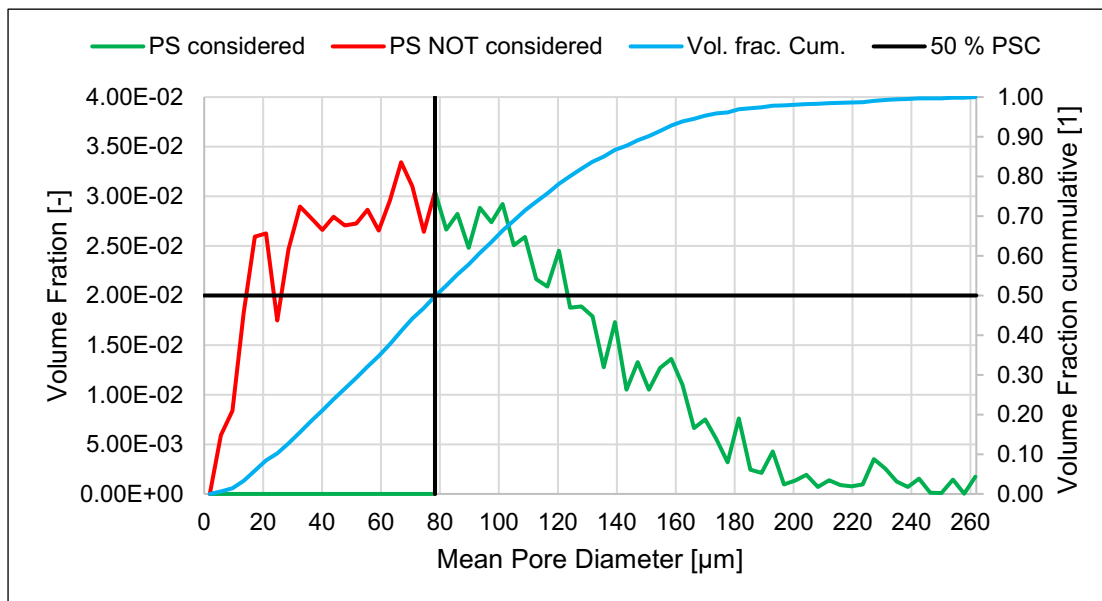


Figure 3-5 PSD considering 50 % PSC.

With all input parameters set to the desired scenario, the TORS algorithm runs through the following 8 steps:

- (1) Computing the distance from the oil phase into all other phases.
- (2) Computing the distance from the water phase, including the residual water, into all other phases.
- (3) Loading the two computed distance fields.
- (4) Subtraction of the oil distance field from the water distance field.
- (5) Thresholding the new field at zero.
- (6) Replacing the solid voxel of the original structure with the above results.
- (7) Changing the newly generated material characteristics to solid and adding label information.
- (8) Saving the generated structure according to the “Result geometry name”.



Figure 3-6 illustrates this process using a simple case with one solid material present in the input structure. The TORS parameters are set according to Figure 3-4, with water being the WP and oil being the NWP. The oil-rock contacts are turned into one new material with a CA of  $140^\circ$  and a PSC of 50%. The left side (A) displays the structure after primary drainage. The right side (B) shows the same structure after spontaneous imbibition, including the newly generated OW material (black) resulting from the TORS process.

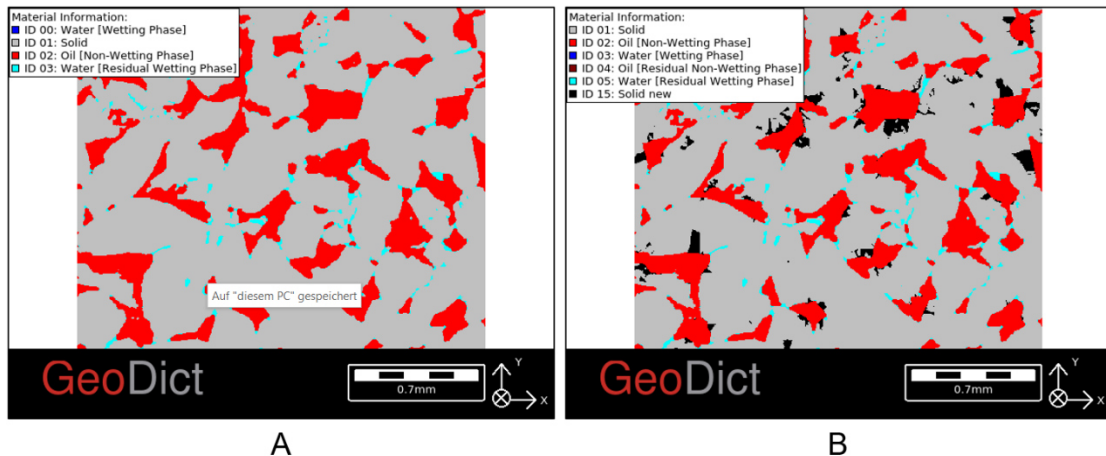


Figure 3-6 TORS output: (A) structure after primary Drainage, (B) Structure after spontaneous Imbibition including newly generated OW material (black), resulting from the TORS process.

Thereby, the amount of the newly generated material depends heavily on the PSC parameter. The higher the parameter is set the more pore space is considered. As a result, the considered contact areas between solid and oil increase and thus increase the amount. This algorithm can either be used independently or by selecting the appropriate checkbox in the third and final algorithm described in the next section.

### 3.4 Capillary Pressure Hysteresis (CPH)

The CPH algorithm is intended to lay the foundation for simulating a capillary pressure hysteresis, including the forced part of an imbibition and spontaneous part of a drainage. According to Math2Market, the CPH algorithm is capable to simulate:

- I. Primary drainage.
- II. First imbibition (spontaneous and forced).
- III. Secondary drainage (spontaneous and forced).

To fulfill this task, and especially to overcome the hurdle regarding the processes related to negative capillary pressures, the CPH algorithm relies on a special approach. The algorithm utilizes not only the output structure obtained by the DCA algorithm but

also the SatuDict Module, described in section 3.1.1, with a specific sequence of executed runs and a specialized set of boundary conditions. Furthermore, the TORS algorithm plays an important role, since a forced Imbibition can only take place if the solid materials contain both WW and OW regions. The most special feature of this algorithm is its capability to implement multiple CA. A structure consisting out of up to four solid materials can be provided with up to four different CA's, whether in the WW or OW range. In addition, by taking advantage of the TORS algorithm, again up to four turning CA's can be introduced, resulting in a possible consideration of up to 8 different CA's in one simulation. Figure 3-7 shows the corresponding input parameters of the CPH algorithm, highlighting the multiple CA section.

The screenshot shows the input parameters for the CPH algorithm. The 'Fluid Parameters' section is highlighted with a red box, indicating the multiple contact angle (CA) settings. The parameters are as follows:

| Parameter  | Value                               |
|--|-------------------------------------|
| Surface Tension / (N/m)  | 0.03                                |
| Contact Angle for Material ID 1 / (*)  | 40                                  |
| Contact Angle for Material ID 2 / (*)  | 40                                  |
| Contact Angle for Material ID 3 / (*)  | 40                                  |
| Contact Angle for Material ID 4 / (*)  | 40                                  |
| Turn Oil-Rock Contacts into non-wetting phase (after Drainage - before Imbibition) | <input checked="" type="checkbox"/> |
| Oil-Rock contacts into:  | one material and CA                 |
| Contact Angle for new Material / (*)   | 140                                 |
| Limit to oil-rock surfaces in large pores  | <input checked="" type="checkbox"/> |
| Volume of pore space considered / (%)  | 50                                  |

Figure 3-7 CPH algorithm input parameters.

As shown in Figure 3-7, there are five main groups of parameters to specify the desired simulation. Those groups are:

- Fluids: defining WP and NWP.
- Fluid parameters: defining the individual CA and the IFT.
- TORS: as described in section 3.3.
- Dynamic pore morphology method: as described in section 3.1.1.
- Hysteresis steps: defining the considered drainage steps.

For correct usage of this algorithm, it is important to maintain a specific sequence of constituent materials on the utilized structure. The material ID 00 is always required to represent the saturated pore space. As shown in Figure 3-7 the up to four assignable CA are coupled to a specific material ID. Furthermore, it is necessary to keep the

interface steps size constant to achieve comparable results. For a structure meeting the constituent criteria, and with all parameters defined, the CPH algorithm runs through up to five SatuDict simulations, depending on the selected hysteresis steps. The individual simulations differ primarily in the location of the WP and NWP reservoirs and depending on the computed process (drainage or imbibition), the corresponding invading phase. To extend the simulation possibilities by both, the forced imbibition and spontaneous drainage branch, the CPH algorithm utilizes a simple approach. Thereby, the forced imbibition is conducted as a drainage process, with the WP and NWP reservoirs set up accordingly. But prior to the run, the invading phase (NWP) is reassigned to be water instead of oil. For the spontaneous drainage, this approach follows the same principle, with the difference that a spontaneous imbibition setup is utilized. And again, prior to the run, the corresponding invading phase (WP) is reassigned to be oil instead of water. Figure 3-8 illustrates these boundary conditions for the five possible scenarios.

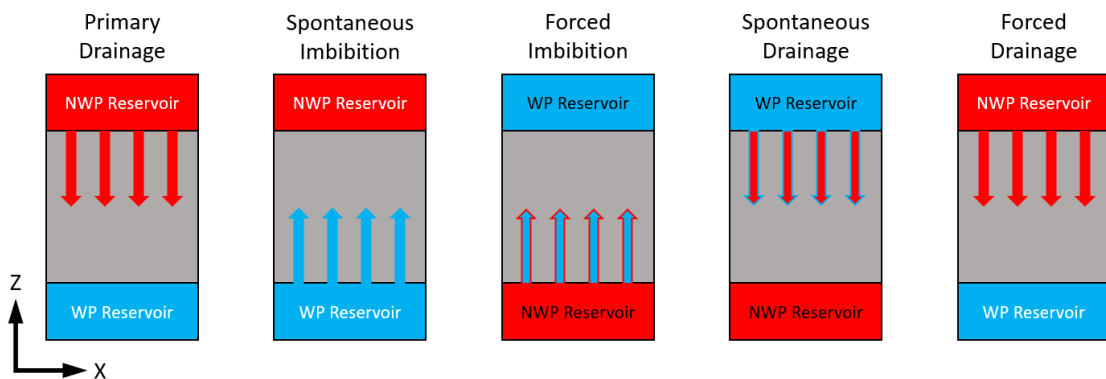


Figure 3-8 Location of WP and NWP reservoirs and the corresponding invading phase according to the process, defined in the CPH algorithm.

As a starting point, the entire structure is saturated with water. The CPH algorithm starts with the simulation of the primary drainage. As described before, the simulations are stepwise procedures where the WP and NWP are stationary distributed. For each step, these distributions change according to the respective capillary pressure.

Through the primary drainage simulation oil as NWP is forced into the structure and displacing the present water to the connate water saturation. Resulting in the utilized structure being mainly saturated with NWP. The resulting WP and NWP distributions of the last step of the primary drainage are the starting point for the up following procedure.

Now, depending on the defined case, the algorithm is either applying the TORS algorithm to generate OW regions or directly continuing with the spontaneous

imbibition in case oil wet contact angles are already present. The spontaneous imbibition is then directly followed by the forced imbibition run, with the last step forming the corresponding starting point. In case the “compute secondary drainage” box is checked, the algorithm continues with two more runs. The spontaneous drainage, starting at the last step of the forced imbibition, and the forced drainage continuing after the spontaneous drainage. Figure 3-9 displays the results of the CPH algorithm running through the described hysteresis cycle.

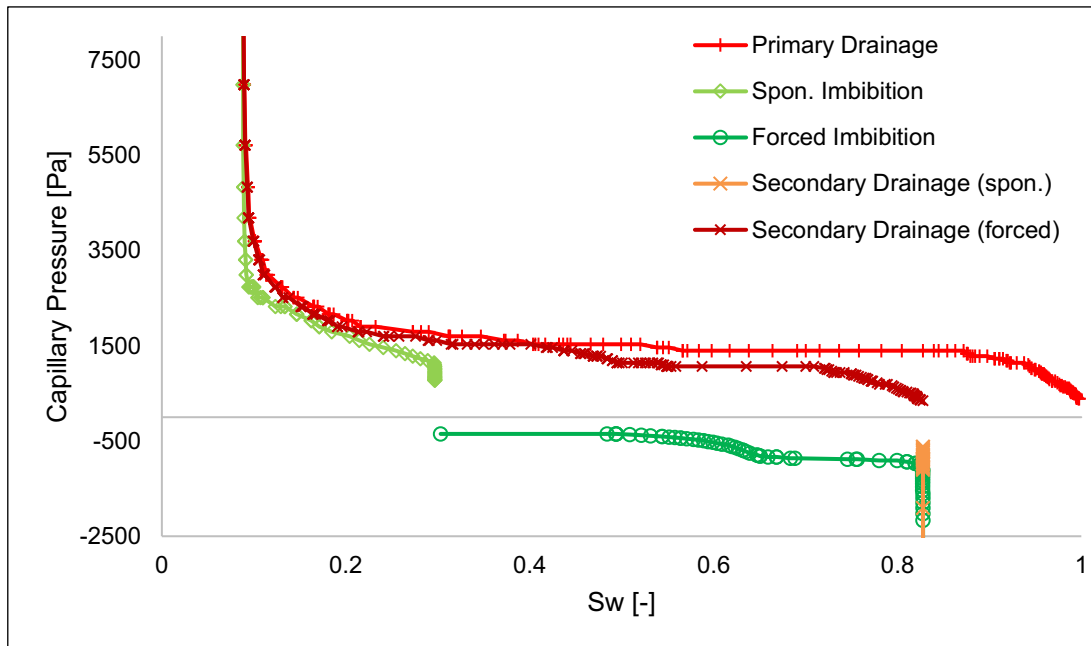


Figure 3-9 CPH algorithm: Resulting capillary pressure curve of the possible hysteresis cycle.

These simulations show that this new approach can model the capillary pressure functions for the forced imbibition and spontaneous drainage process. Furthermore, Figure 3-9 shows that the computed hysteresis cycle from primary drainage to secondary drainage, follows the correct physical principles, as described in section 2.1.3. The sudden drop in pressure during the transition from spontaneous imbibition to forced imbibition is striking. This pressure drop relates to the folding of the WP meniscus that occurs when the WP pressure is higher than the NWP pressure. Which in turn corresponds to the point from which the water must be forced into the structure. This phenomenon can also be observed in the visualizations of the respective structures from the two processes. While the structure from the last step of the spontaneous imbibition shows an inwardly directed meniscus for the WP ( $P_{WP} < P_{NWP}$ ), the structure from the first step of the forced part shows an outwardly directed WP meniscus ( $P_{WP} > P_{NWP}$ ). Figure 3-10 visualizes this occurrence on the recently

computed capillary pressure curve. Therein highlighting both the last step of the spontaneous imbibition and the first step of the forced imbibition.

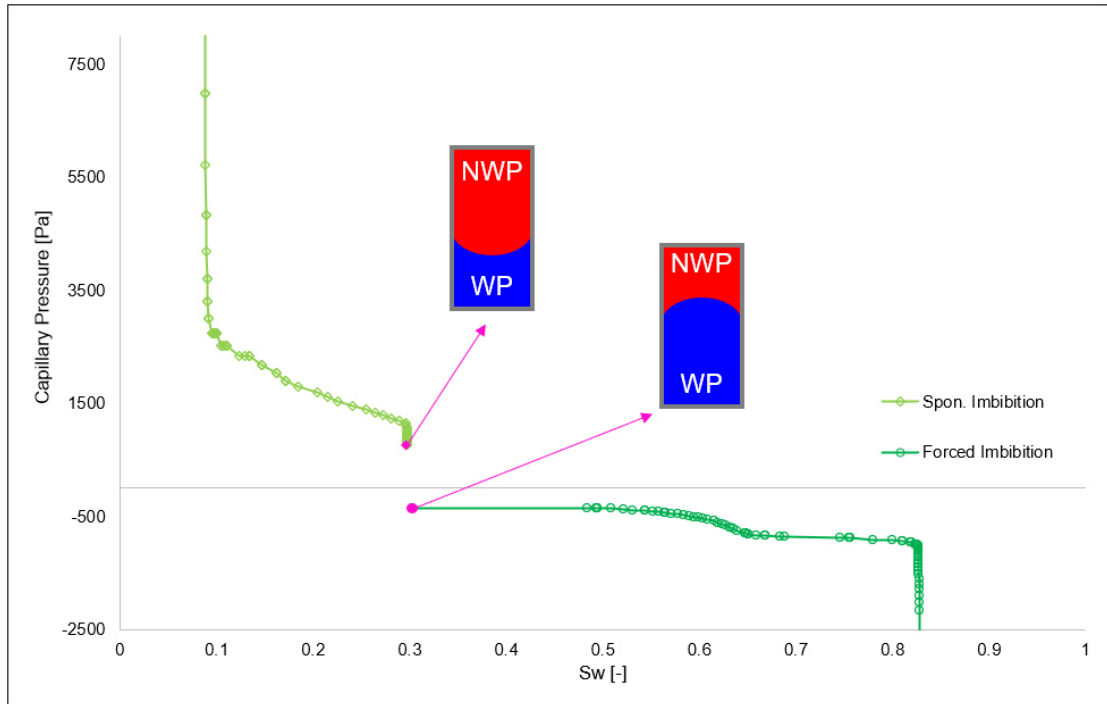


Figure 3-10 Pressure drop in the transition from spontaneous to forced imbibition process.

To cover a flooding scenario from all directions, the CPH algorithm is adapted in terms of WP and NWP reservoir locations, resulting in six possible invasion directions, visualized by Figure 3-11.

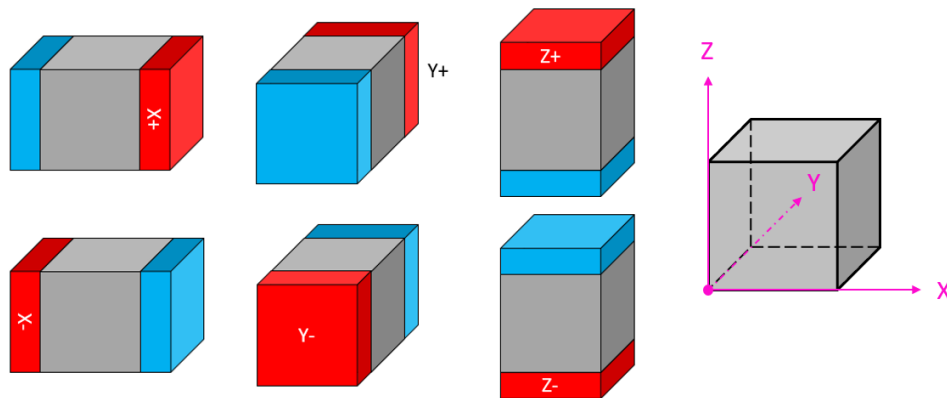


Figure 3-11 Spatial alterations of WP and NWP boundary condition reservoirs.

Each of the individual representations shows the spatial variation of the boundary reservoirs. Later on, the named direction (Z+, Z-, X+, X-, Y+, Y-) corresponds to the NWP reservoir and therefore determines the flow direction for drainage and imbibition processes.

### 3.5 Surface Area Analysis

As both, the DCA and the TORS algorithm, change the volumetric composition of the solid materials, the question of surface area constellation remains to be clarified.

This constellation plays a decisive role in the simulations, as it reflects the amount of possible contact between the saturated pore space and the respective solid materials assigned with individual CAs.

A surface area analysis of several structure modifications used in this thesis and based on the DCA algorithm has shown a direct relationship between the implemented SVP value and the resulting surface area constellation. Additionally, this effect is independent of the implemented region size and whether the structure consists of two, three, or four solid materials. The results of this analysis are provided in Table 25 in appendix section A.2.

However, this relationship does not apply to the TORS algorithm. Therein, the decisive parameter is the implemented PSC value, described in section 3.3. After applying the TORS algorithm, further analysis of both the SVP and surface area constellations reveals the strong influence of the PSC parameter. Implementing 50 % PSC in the TORS algorithm always results in the same percentages for SVP and surface area for the newly introduced OW material, regardless of the utilized structure. The SVP of the new material is always around 5 %, which corresponds to a surface share of around 12 % for each case. Only changing the implemented PSC value results in differing constellations. The results of this analysis are provided in Table 26, Table 27, and Figure 6-4 in appendix section A.2.

# Chapter 4

## Results and Discussion

This section provides information on all the simulation cases of this thesis. Including a description of the used structures, the implemented and varying parameters, as well as their associated results. As described in section 2.1, the CA is a key parameter for saturation-dependent processes. Especially considering its value, the existing number of individual CA, and the spatial distribution within a porous media. To precisely investigate these influences on a saturation-dependent simulation, several simulations are conducted with corresponding modifications of the mentioned parameters. In general, five main experimental setups are covered:

- I. Case A: Single solid material.
- II. Case B: Single to multiple solid materials.
- III. Case C: Multiple solid materials.
- IV. Case D: Multiple solid materials, differing region sizes.
- V. Case E: Distinct spatial separation.

Within these, the essential parameters described in sections 3.2, 3.3, and 3.4 are altered to cover a broad spectrum of possibilities and to gain knowledge on the potential of the implementations. The following sub-sections describe the individual covered scenarios of all five setups and present the related influences and simulation results. Since the forced imbibition branch is of major interest, the applied simulation sequence for all cases is:

- a. Primary Drainage
- b. Spontaneous Imbibition
- c. Forced Imbibition

**Each case is set to be a water flood, hence always water as WP and oil as NWP.**

## 4.1 Utilized structure

The chair of Reservoir Engineering at the Montanuniversität Leoben provided a digital twin of a Sandstone sample to achieve the objective of this thesis. All discussed simulations are conducted on this structure. The corresponding dimensions are 600 x 600 x 600 voxel with a resolution of 3.82  $\mu\text{m}$ , and the volumetric composition shows 26.31 % pore space, hence porosity, and 73.69 % solid material. Figure 4-1 provides a 3D visualization of the original digital twin.

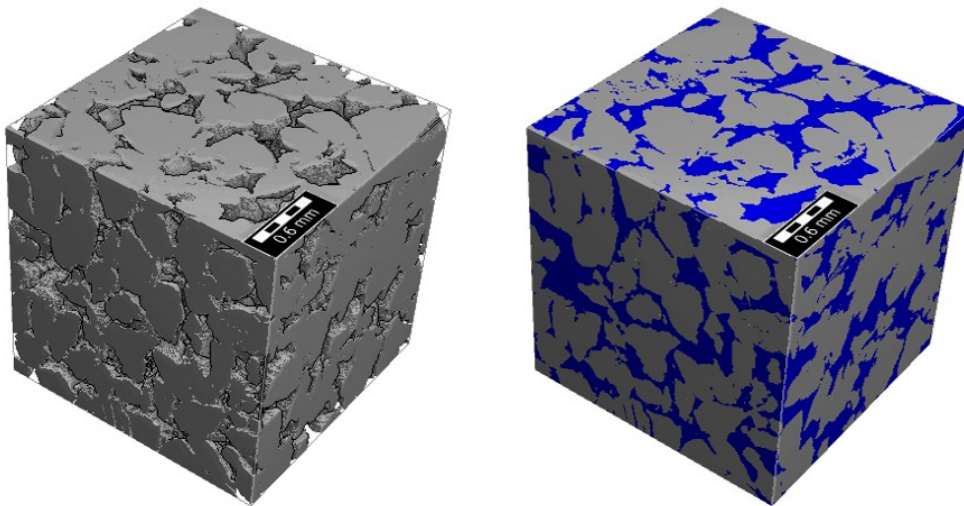


Figure 4-1 Digital twin of the Sandstone sample: (left): only solid material visible (grey), (right): solid material (grey) and water-saturated pore space (blue).

Figure 4-2 provides a 2D visualization of the original structure, depicting the water-saturated pore space in blue and the solid material in grey.

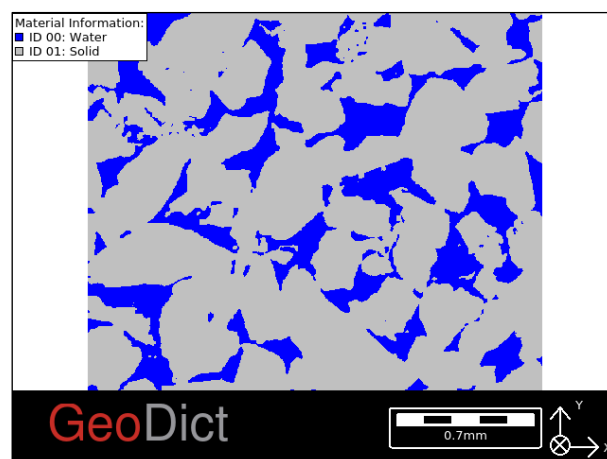


Figure 4-2 2D representation of the original structure.

This structure forms the basis for all adaptations based on the DCA algorithm, described in section 3.2.



## 4.2 Case A: Single solid material

The first setup can be understood as a base case, as it uses the original structure consisting out of pore space and one solid material. This case is primarily investigating the working principle of the TORS and CPH algorithms. Thereby, clarifying the associated boundary conditions, influences, and limitations using this simple setup. Case (A) is subjected to four different scenarios with varying conditions. The following tables and figures present both, the implemented parameters of each scenario and the corresponding results.

### 4.2.1 Simulated scenarios

The first scenario is investigating the effects of the TORS algorithm by altering the related PSC percentage. This percentage is expected to exert the strongest influence on the simulations, according to its working principle (section 3.3). Therefore, these first simulations are intended to determine whether this algorithm follows the correct physical principles and results in the related trends. Table 1 enlists the simulations conditions.

Table 1 Case A, Scenario A1.

| A1: Varying PSC. |    |         |      |                |
|------------------|----|---------|------|----------------|
| Name:            | CA | turn CA | PSC  | NWP reservoir: |
| A1.1             | 10 | 140     | 1 %  | Z+             |
| A1.2             |    |         | 50 % |                |
| A1.3             |    |         | 75 % |                |
| A1.4             |    |         | 99 % |                |

As expected, the results of these simulations show the strong influence of the PSC value on the computed capillary pressure curves. As the value is included in the TORS algorithm, the impact is only visible for the imbibition branch and not affecting the primary drainage. Especially the two extreme cases, (A1.1) and (A1.4), show that a physically realistic behavior is reflected.

The implementation of 1 % PSC (A1.1) is hardly considering any pore space for the generation of new OW material, and ultimately the present wetting conditions are not altered. Thus, resulting in a capillary pressure curve with a strong WW trend. This trend is indicated by both, a higher zero-crossing saturation, hence the spontaneous imbibition reaching a higher  $S_w$  value, and higher residual oil saturation.

On the other hand, implementing 99 % PSC is taking almost the entire pore space into account and thus clearly changing the predominant wetting conditions to strongly OW.

Hence the resulting capillary pressure curve depicts a corresponding OW trend. This trend is indicated by a low zero-crossing saturation and low residual oil saturation. Which in turn reflects the physically correct behavior for strongly OW environments.

Accordingly, the two cases in between, with 50 % PSC (A1.2) and 75 % PSC(A1.3), also follow the right trend. Increasing the implemented PSC value is decreasing the outreach of the spontaneous imbibition more towards the left side of the diagram. Hence the resulting curves present a more moderate WW behavior for (A1.2) and a more OW behavior for (A1.3). The corresponding simulation results of scenario A1 are illustrated in Figure 4-3.

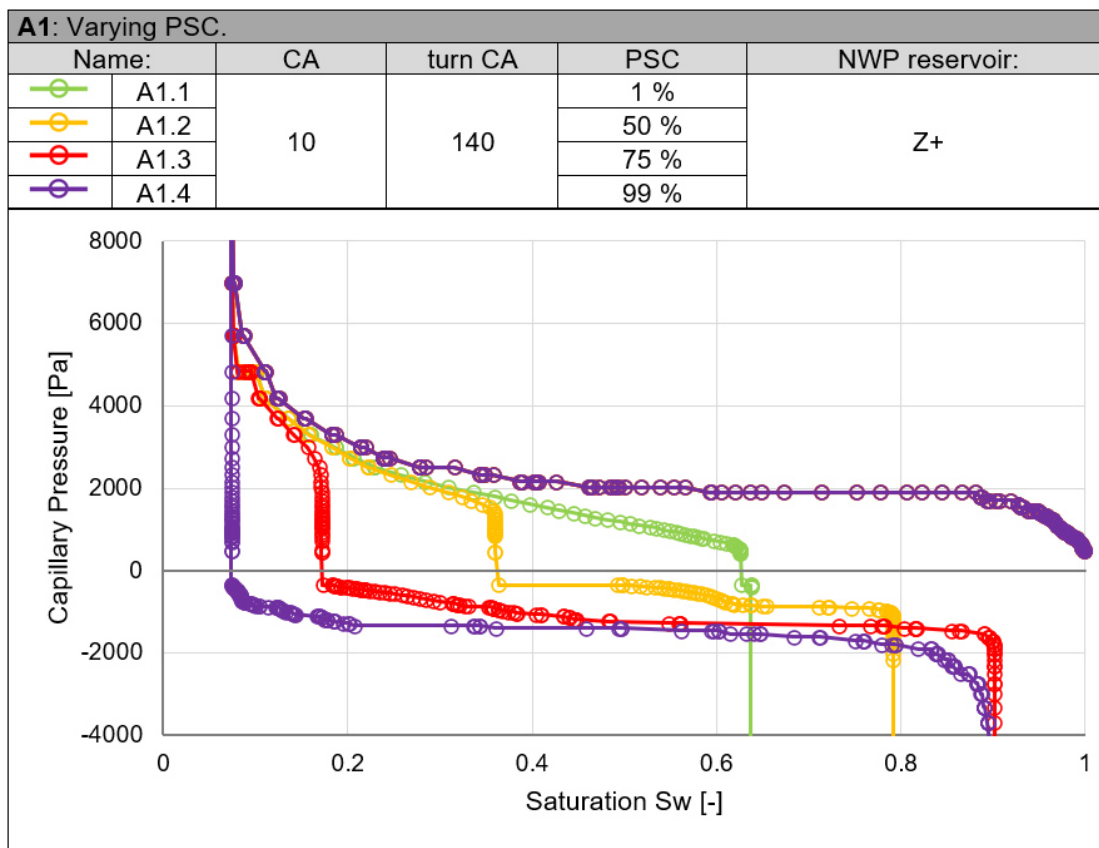


Figure 4-3 Case A, Scenario A1, Results.

Also, the corresponding wettability indices (WI) show the correct trends for decreasing WW tendency with increasing PSC value. Thereby, the respective ratios of the area underneath the spontaneous imbibition curve, and the area above the forced imbibition curve represent the increasing amount of work required to replace the oil with water. As long as the area under the spontaneous imbibition curve is larger than the area above the forced imbibition curve, this index is positive and thus indicates a WW environment. Equally sized areas result in an index of approximately zero (NW). In case the area above the forced imbibition is larger, the resulting negative index

indicates an OW environment. Figure 4-4 exemplifies these areas on the computed capillary pressure curve from simulation (A1.2). As for this curve, the area underneath the spontaneous imbibition curve is still larger than the area above the forced imbibition, the resulting WI is positive and thus indicates a WW environment.

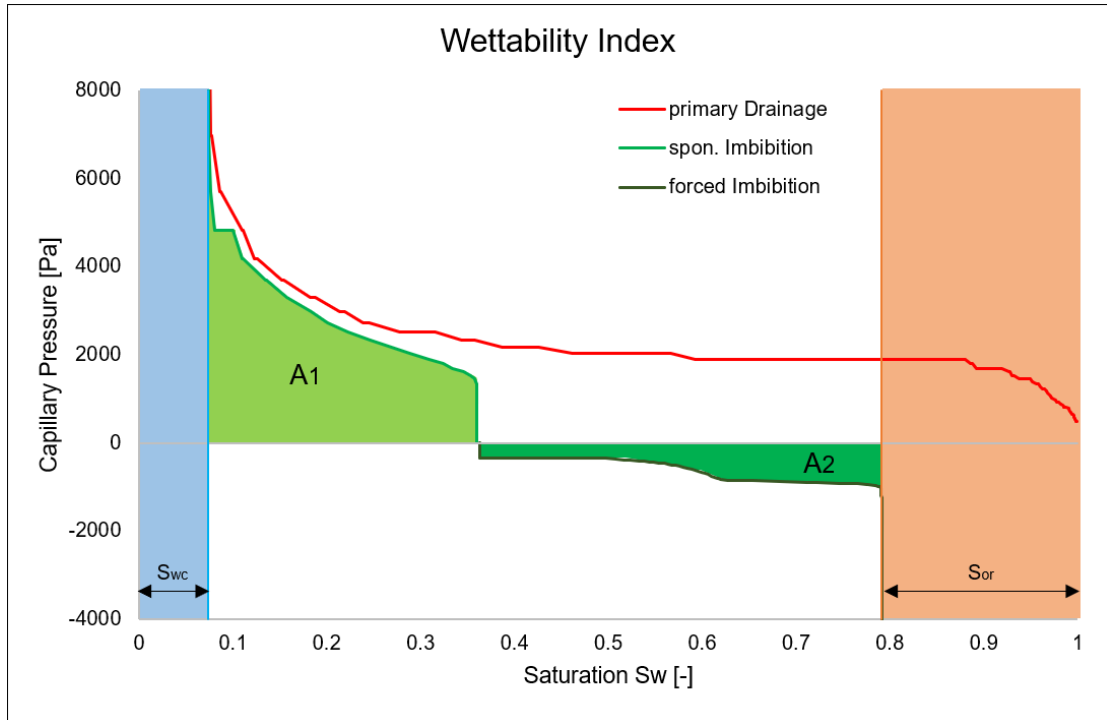


Figure 4-4 Exemplified wettability index.

The approximate WI's of the respective simulations are provided in Table 2. These values show a transition from a high positive index for the strong WW conditions (A1.1) to a high negative index for the strong OW conditions (A1.4). Hence, this transition is depicting the correct physical behavior.

Table 2 Wettability indices Scenario A1.

| Name: | A <sub>1</sub> | A <sub>2</sub> | A <sub>1</sub> /A <sub>2</sub> | WI                                   |
|-------|----------------|----------------|--------------------------------|--------------------------------------|
| /     | [ Area ]       | [ Area ]       | [ - ]                          | Log(A <sub>1</sub> /A <sub>2</sub> ) |
| A1.1  | 1161.68        | 3.60           | 322.78                         | 2.51                                 |
| A1.2  | 821.06         | 261.37         | 3.14                           | 0.50                                 |
| A1.3  | 377.37         | 816.05         | 0.46                           | -0.33                                |
| A1.4  | 0.71           | 1251.43        | 0.001                          | -3.24                                |

The next scenario analyses the influences related to the angular range of the implemented CA. As this range is reflecting the wetting conditions, described in section 2.1.1, it is expected to observe trend changes with increasing value. Table 3 enlists the implemented parameters for this scenario.

Table 3 Case A, Scenario A2.

| A2: Varying CA. |     |         |     |                |
|-----------------|-----|---------|-----|----------------|
| Name:           | CA  | turn CA | PSC | NWP reservoir: |
| A2.1            | 0°  | 140°    | 50% | Z+             |
| A2.2            | 10° |         |     |                |
| A2.3            | 40° |         |     |                |
| A2.4            | 60° |         |     |                |

As expected, the simulation results of this scenario show trend in the right direction. Increasing the implemented CA value, from 0° (A2.1) to 60° (A2.4), is decreasing the overall WW tendency. The prevailing wetting conditions shift more towards a more moderate WW environment. This decrease in WW tendency is depicted by three features on the respective curves:

- I. A decreasing pressure plateau of the primary drainage. So, the part of the curve in which the water saturation strongly decreases but the pressure remains constant or almost constant.
- II. A decrease in the occurring zero-crossing saturation, so the point where the spontaneous imbibition transfers to the forced imbibition.
- III. A decrease in residual oil saturation.

In addition, the calculated WI's of these simulations support the decreasing trend of the WW tendency through decreasing indices with increasing implemented CA. Table 4 contains the associated values of the three decreasing characteristics and the respective indices.

Table 4 Occurring changes &amp; WI for Scenario A2.

| Occurring changes:   |                                       |                    |            |                       |
|----------------------|---------------------------------------|--------------------|------------|-----------------------|
| Simulation:          | Plateau h [ $S_w$ 0.50 – $S_w$ 0.85]: | $S_{zero-cross}$ : | $S_{or}$ : |                       |
| Name:                | [ Pa ]                                | [ 1 ]              | [ 1 ]      |                       |
| A2.1                 | 1952.7                                | 0.36               | 0.20       |                       |
| A2.2                 | 1932.8                                | 0.36               | 0.20       |                       |
| A2.3                 | 1417.5                                | 0.30               | 0.17       |                       |
| A2.4                 | 810.9                                 | 0.20               | 0.12       |                       |
| Wettability Indices: |                                       |                    |            |                       |
| Name:                | $A_1$                                 | $A_2$              | $A_1/A_2$  | WI                    |
|                      | [ Area ]                              | [ Area ]           | [ - ]      | $\text{Log}(A_1/A_2)$ |
| A2.1                 | 864.16                                | 258.25             | 3.35       | 0.52                  |
| A2.2                 | 821.06                                | 261.37             | 3.14       | 0.50                  |
| A2.3                 | 389.08                                | 302.37             | 1.29       | 0.11                  |
| A2.4                 | 99.34                                 | 362.75             | 0.27       | -0.56                 |

Figure 4-5 visualizes the resulting capillary pressure curves, which illustrate the decreasing WW tendency.

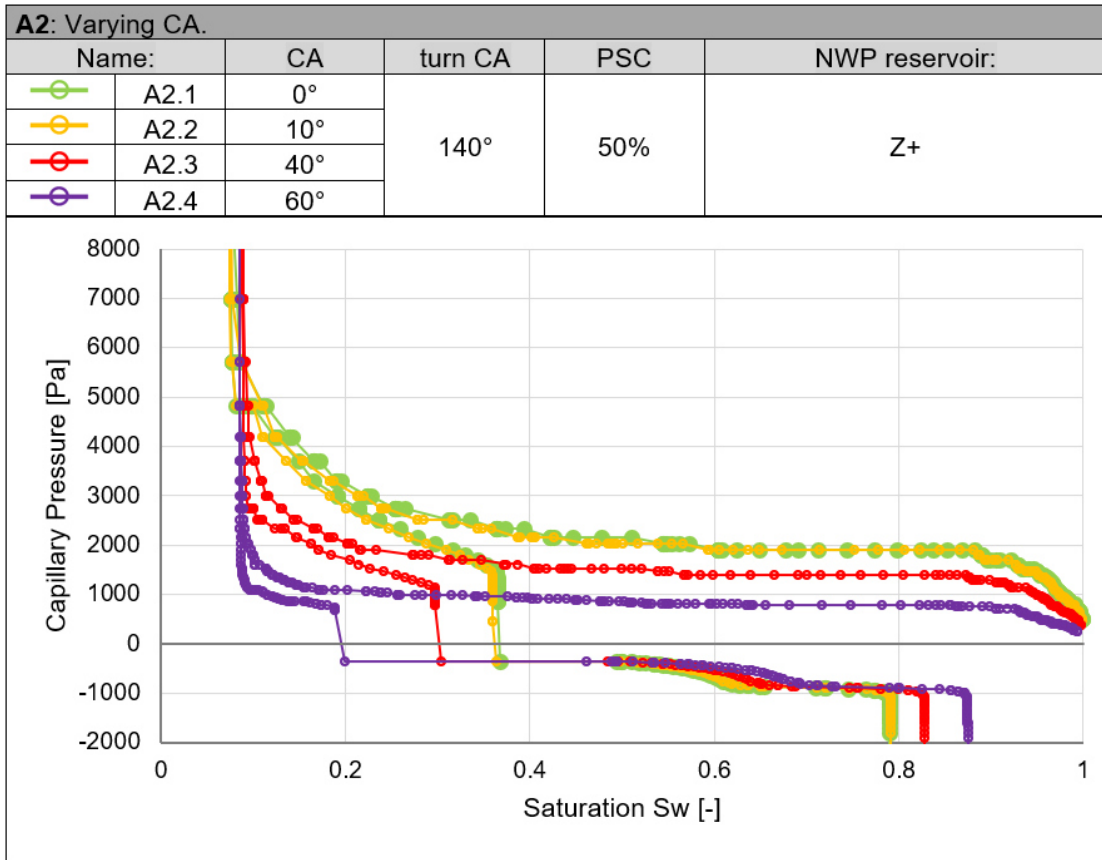


Figure 4-5 Case A, Scenario A2, Results.

Since these are exclusively WW conditions, the simulations follow the correct physical behavior. This in turn is shown correctly on the resulting capillary pressure curves and corresponds to the changes and WI values shown.

As a next step, the influence of the turning CA is investigated by scenario A3. Table 5 provides the corresponding input parameters to the simulations.

Table 5 Case A, Scenario A3.

| A3: Varying turn CA. |     |         |     |                |
|----------------------|-----|---------|-----|----------------|
| Name:                | CA  | turn CA | PSC | NWP reservoir: |
| A3.1                 | 10° | 120°    | 50% | Z+             |
| A3.2                 |     | 140°    |     |                |
| A3.3                 |     | 170°    |     |                |

As for this scenario exclusively, the turning CA is altered the simulation results show, as expected, no change on the computed primary drainage curve. This observation makes perfect sense since the turning CA is part of the TORS algorithm, which only

influences the imbibition branch. The main differences can be observed for the forced part of the imbibition. Increasing the turning CA increases the areas above the forced imbibition curve, thus indicating more and more work that is required to displace the oil through the water. Since for this scenario an increase in the implemented values corresponds to an increasing OW tendency of the newly introduced material, these observations tend towards the correct behavior. The stronger the oil phase is attracted to the new material the more work is required to displace it. Accordingly, the first simulation (A3.1) requires less energy to remove the oil due to the weaker attraction. The corresponding WI introduces a stronger WW tendency than in the other two simulations since the area above the forced imbibition curve is smaller. Which, for this scenario, is leading to lower residual oil saturation. The respective indices are provided in Table 6, and Figure 4-6 visualizes the simulation results.

Table 6 Wettability indices Scenario A3.

| Name: | A <sub>1</sub> | A <sub>2</sub> | A <sub>1</sub> /A <sub>2</sub> | WI                                   |
|-------|----------------|----------------|--------------------------------|--------------------------------------|
| /     | [ Area ]       | [ Area ]       | [ - ]                          | Log(A <sub>1</sub> /A <sub>2</sub> ) |
| A3.1  | 821.06         | 106.21         | 7.73                           | 0.89                                 |
| A3.2  | 821.06         | 261.37         | 3.14                           | 0.50                                 |
| A3.3  | 821.06         | 487.17         | 1.69                           | 0.23                                 |

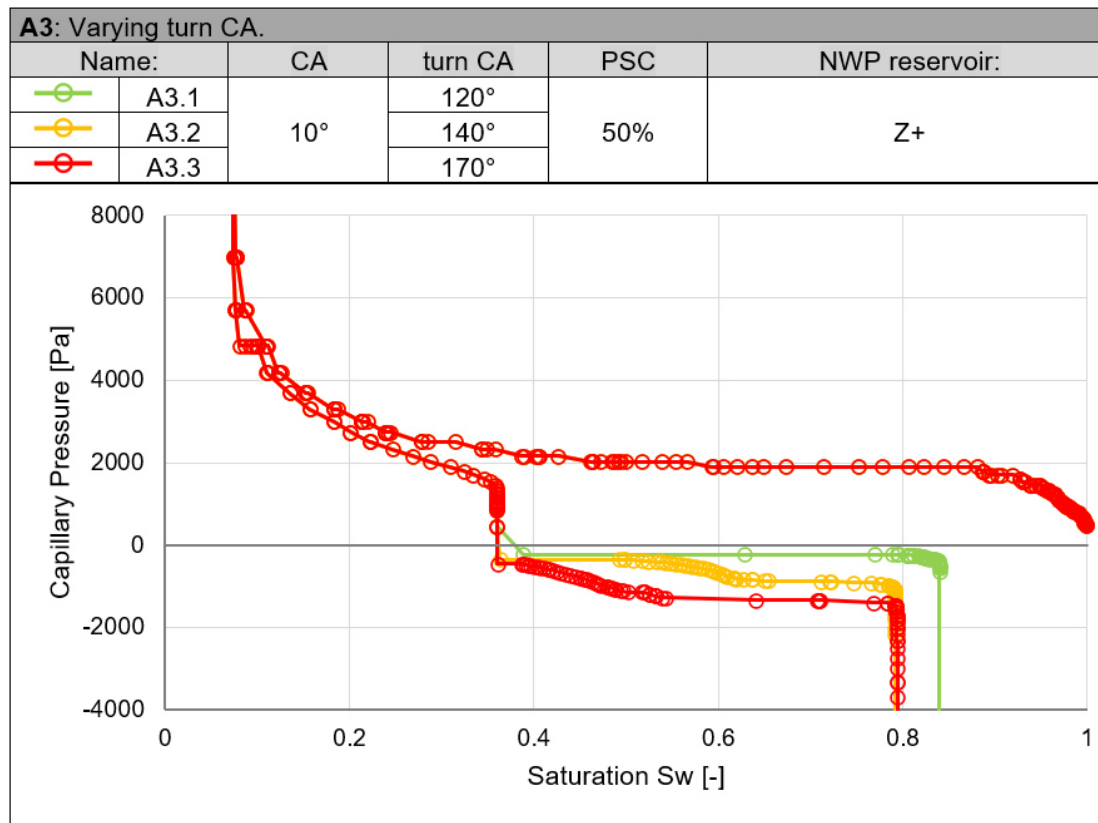


Figure 4-6 Case A, Scenario A3, Results.

The final examination for Case A is exposing the utilized structure to different locations of the NWP reservoir, hence changing the process directions. The details of the respective simulations of this scenario are enlisted in Table 7.

Table 7 Case A, Scenario A4.

| A4: Varying NWP reservoir. |     |         |     |                |
|----------------------------|-----|---------|-----|----------------|
| Name:                      | CA  | turn CA | PSC | NWP reservoir: |
| A4.1                       | 40° | 140°    | 50% | Z+             |
| A4.2                       |     |         |     | X+             |
| A4.3                       |     |         |     | Y+             |

The computed results can hardly be distinguished for this scenario. One possible reasoning could be the nature of the rock type used. The utilized sandstone is quite homogenous and well-sorted. Hence the homogeneity is shrinking the range of pore throats and consequently the possible range of capillary pressures. Although, a slight difference at the beginning of the primary drainage is observable. These differing invasion steps are likely to be related to the somewhat altered initial conditions. For this reason, Figure 4-7 illustrates the simulation results tailored to the early stages of the primary drainage.

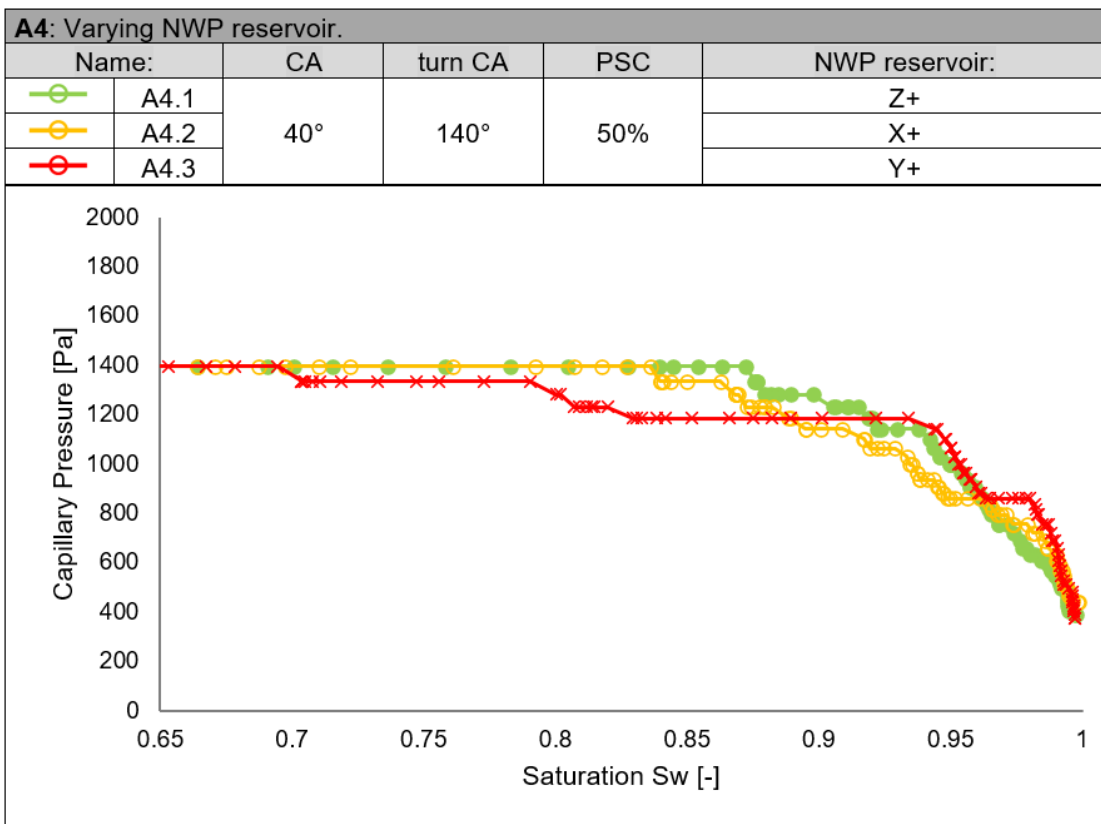


Figure 4-7 Case A, Scenario A4, zoomed-in Results.

The results from case (A) show that the implemented PSC value has the strongest influence on the simulations. Increasing its value introduces more OW material and thus significantly changing the wettability. The implemented CA and turn CA also show an influence on the simulation. A change in the respective CAs to more WW or OW conditions show the corresponding effect in the results. These effects are captured by the right trend in terms of residual saturations, pressure plateau heights for the primary drainage and zero crossing in the imbibition curve. Furthermore, the respective wettability indices show the right trend. In contrast, the spatial modifications of the boundary layers show only minor influence due to the homogeneity of the structure.



### 4.3 Case B: Single to multiple solid materials

To investigate the influence of the spatial distribution of multiple CA within the porous media, case B introduces four simulations on four different structures. These consist out of one, two, three, and four present solid materials with the associated number of varying CA.

#### 4.3.1 Utilized structure

For this case, in addition to the original structure, three more are generated by taking advantage of the DCA algorithm, described in section 3.2. The applied DCA parameters for all three are the following:

- Region size: 100  $\mu\text{m}$ .
- Random Seed: 42.

The exact procedure to generate these structures with multiple solid materials is explained in appendix section A.1.

Figure 4-8 provides 2D visualizations of all four structures, along with the related legend and perspective.

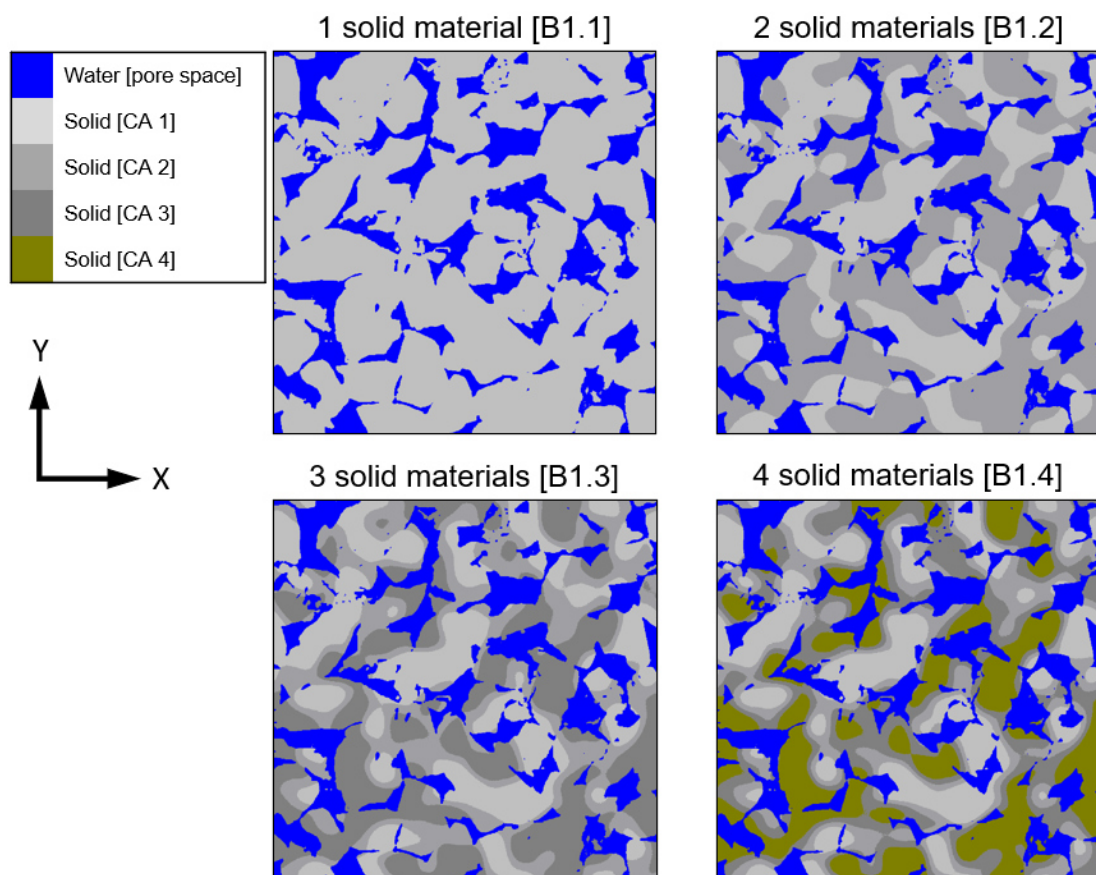


Figure 4-8 Utilized structures for Case B.

The spatial distribution of the solid materials follows a smooth transitioning trend. Each solid phase is only in contact with one other solid phase, but all of them are somewhere contacting the pore space. This occurrence is important so all the implemented CA within the CPH algorithm exert their influence on the computation.

According to the working principle of the DCA algorithm, explained in section 3.2, only the composition of the solid material is altered, and the volume of the pore space is kept constant. The respective solid compositions are listed in Table 8.

*Table 8 Solid material composition for Scenario B.*

| Structure: | Solid materials: | Volumetric share of each material: |
|------------|------------------|------------------------------------|
| B1.1       | 1                | 100 %                              |
| B1.2       | 2                | 50 %                               |
| B1.3       | 3                | 33 %                               |
| B1.4       | 4                | 25                                 |

### 4.3.2 Simulated scenarios

Table 9 presents the details of the simulation scenario for Case B. To keep the scenario simple, the turning CA, the PSC, and the process direction is kept constant, to observe the impact of the implemented value and number of CA.

*Table 9 Case B, Scenario B1.*

| B1: Multiple CA. |      |      |      |      |         |      |                |
|------------------|------|------|------|------|---------|------|----------------|
| Name:            | CA 1 | CA 2 | CA 3 | CA 4 | turn CA | PSC  | NWP reservoir: |
| B1.1             | 10°  | /    | /    | /    | 140°    | 50 % | Z+             |
| B1.2             | 10°  | 30°  | /    | /    |         |      |                |
| B1.3             | 10°  | 30°  | 45°  | /    |         |      |                |
| B1.4             | 10°  | 30°  | 45°  | 60°  |         |      |                |

The simulation results show that the introduction of additional solid materials and their associated CA still follows the correct physical behavior. The increase in the number of solids present and thus the CAs present influences the prevailing wetting conditions. These altered conditions are captured correctly in the respective computed capillary pressure curves. The deliberate increase in the angular range by increasing the number of solid materials from just one solid at 10 ° (B1.1) to four solids in the range from 10 ° to 60 ° (B1.4) reduces the observable WW behavior.

As before for scenario (A2), this decreasing tendency is represented by a decrease in the plateau height of the primary drainage, a decreasing zero-crossing saturation in

the imbibition curve, and a decrease in the residual oil saturation. But in this case, the decrease that occurs is not so great compared to (A2) (B1.1 = A2.2).

This observation is directly related to the number of CA present and the selected angular range of this scenario. On the one hand, the results are influenced by the direct relationship between SVP and surface area in the DCA algorithm and the constant SVP and surface area of the newly introduced material after the TORS algorithm.

These relations are described in section 3.5. Thus, for each utilized structure the individual solid materials, and the assigned CAs, have a balanced influence on the simulations. Which is based on the uniform distribution and the equal share of surface area. On the other hand, the angle range considered introduces weaker or more moderate WW tendency with each additional solid material, which leads to a corresponding trend.

In addition, this decreasing WW tendency is underpinned by the analysis of the respective wettability indices. Increasing the number of solid materials with their associated CAs decreases the area below the spontaneous part of the imbibition and increases the area above the forced part. Thus, with each additional solid, the energy required to displace the oil increases, which results in a lower WI.

Table 10 contains information on the decreasing characteristics and the respective WI values.

*Table 10 Occurring changes & WI for Scenario B1.*

| Occurring changes:   |                                       |          |                    |                       |
|----------------------|---------------------------------------|----------|--------------------|-----------------------|
| Simulation:          | Plateau h [ $S_w$ 0.50 – $S_w$ 0.85]: |          | $S_{zero-cross}$ : | $S_{or}$ :            |
| Name:                | [ Pa ]                                |          | [ 1 ]              | [ 1 ]                 |
| B1.1                 | 1932.8                                |          | 0.36               | 0.21                  |
| B1.2                 | 1750.3                                |          | 0.35               | 0.20                  |
| B1.3                 | 1629.3                                |          | 0.33               | 0.20                  |
| B1.4                 | 1328.3                                |          | 0.30               | 0.17                  |
| Wettability Indices: |                                       |          |                    |                       |
| Name:                | $A_1$                                 | $A_2$    | $A_1/A_2$          | WI                    |
|                      | [ Area ]                              | [ Area ] | [ - ]              | $\text{Log}(A_1/A_2)$ |
| B1.1                 | 821.06                                | 261.37   | 3.14               | 0.50                  |
| B1.2                 | 674.86                                | 271.40   | 2.49               | 0.40                  |
| B1.3                 | 543.65                                | 226.97   | 2.40               | 0.38                  |
| B1.4                 | 418.25                                | 302.30   | 1.38               | 0.14                  |

Additionally, Figure 4-9 is illustrating the simulation results.

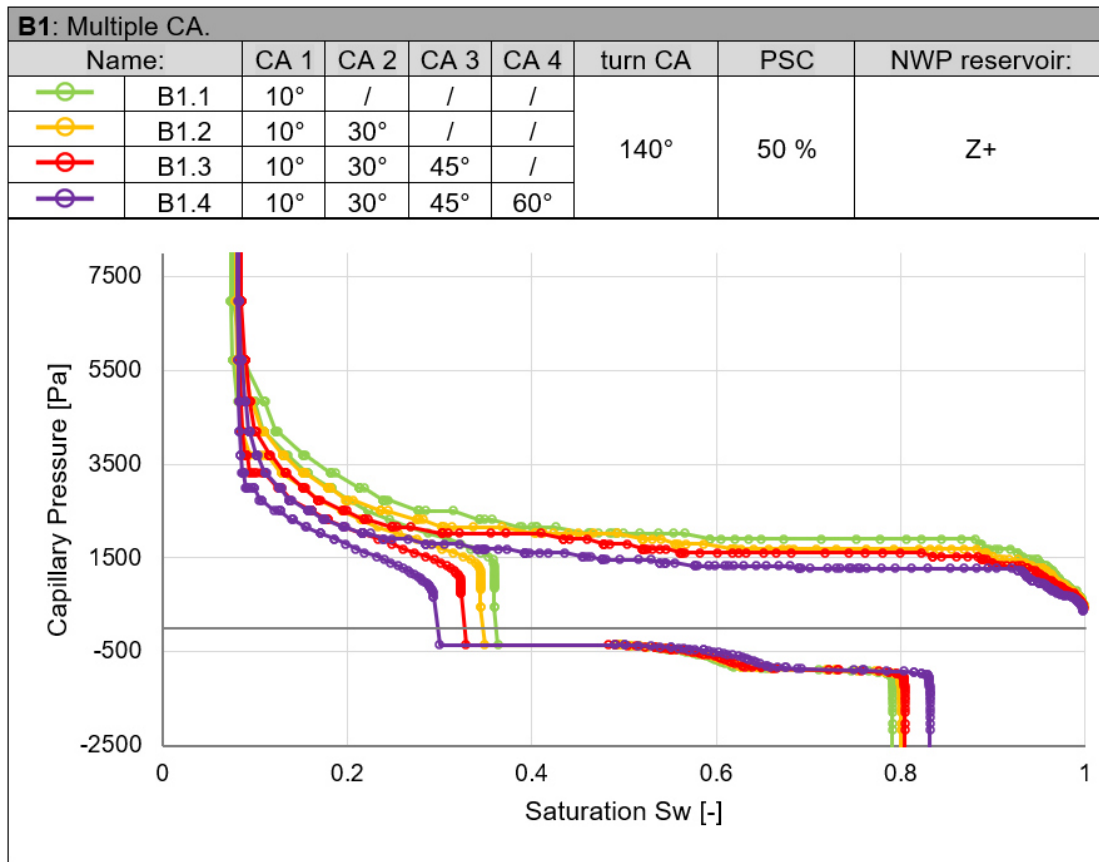


Figure 4-9 Case B, Scenario B1, Results.

The results of case (B) does not only underpin the effect of the CA itself but also relates the influence on the computed capillary pressure curves to the number of CA present in the structure.

## 4.4 Case C: Multiple solid materials

Case C ties in with the last simulation of Case B. It is set up to more precisely investigate how the alteration of the PSC value, the turning CAs, and the number of turning CAs impacts the CPH run on a structure consisting out of four solid materials. Moreover, it should determine whether the trends from the previous cases can also be observed.

### 4.4.1 Utilized structure

The utilized structure for this case is the same as for the last simulation of Case B [B1.4], with the same structural properties as described in section 4.3.1.

### 4.4.2 Simulated scenarios

The first scenario hits the same note as scenario A1 before. By modifying the PSC parameter, it should determine whether the same trend as before occurs and whether or how far it deviates for this case. However, as before the change of the PSC is expected to have a major impact on the simulation. The corresponding simulation details are enlisted in Table 11.

Table 11 Case C, Scenario C1.

| C1: Multiple CA, different PSC. |      |      |      |      |         |      |                |
|---------------------------------|------|------|------|------|---------|------|----------------|
| Name:                           | CA 1 | CA 2 | CA 3 | CA 4 | turn CA | PSC  | NWP reservoir: |
| C1.1                            | 10°  | 30°  | 45°  | 60°  | 140     | 50 % | Z+             |
| C1.2                            |      |      |      |      |         | 75 % |                |

As expected, the simulation results show a strong influence corresponding to the different PSC values. As with scenario (A1) before, the effect does not influence the computation of the primary drainage and is mainly visible for the imbibition branch. In general, the simulation results follow the same trend as before and show a decreasing WW trend along with the increased PSC value. Correspondingly, an increase in the PSC value considers more pore space for the conversion into OW material and correspondingly increases the OW tendency. Depicted by a strong decrease in the zero-crossing saturation in the imbibition curve and a decrease in the residual oil saturation. However, since this scenario is based on a structure made of four solid materials with four individual CAs, there is an observable deviation from the single CA case (A1). The simulations differ about the plateau height of the primary drainage, the respective zero crossing saturations in the imbibition curves, the residual oil saturations, and the resulting WIs. The occurring changes are listed in Table 12.

Table 12 Comparison of Scenario A1 & C1.

|             |                          |   |                          |             |
|-------------|--------------------------|---|--------------------------|-------------|
| Simulation: | Plateau h [ Pa ]:        |   | Plateau h [ Pa ]:        | Simulation: |
| A1          | $S_w 0.50 - S_w 0.85$    | → | $S_w 0.50 - S_w 0.85$    | C1          |
|             | 1932.8                   |   | 1328.3                   |             |
| Simulation: | $S_{OR} [ 1 ]$ :         |   | $S_{OR} [ 1 ]$ :         | Simulation: |
| A1.2        | 0.21                     | → | 0.17                     | C1.1        |
| A1.3        | 0.09                     | → | 0.07                     | C1.2        |
| Simulation: | $S_{zero-cross} [ 1 ]$ : |   | $S_{zero-cross} [ 1 ]$ : | Simulation: |
| A1.2        | 0.36                     | → | 0.30                     | C1.1        |
| A1.3        | 0.17                     | → | 0.09                     | C1.2        |
| Simulation: | WI [ - ]                 |   | WI [ - ]                 | Simulation: |
| A1.2        | 0.50                     | → | 0.14                     | C1.1        |
| A1.3        | -0.33                    | → | -1.30                    | C1.2        |

The increase in the number of solid materials and their associated CA leads to both a more moderate WW environment (C1.1) and a strong OW environment (C1.2). Thus, increasing the energy required to displace the oil. So, the computed capillary pressure curves are shifted further to the left in comparison to the single CA and strongly WW case (A1). Figure 4-10 presents this comparison.

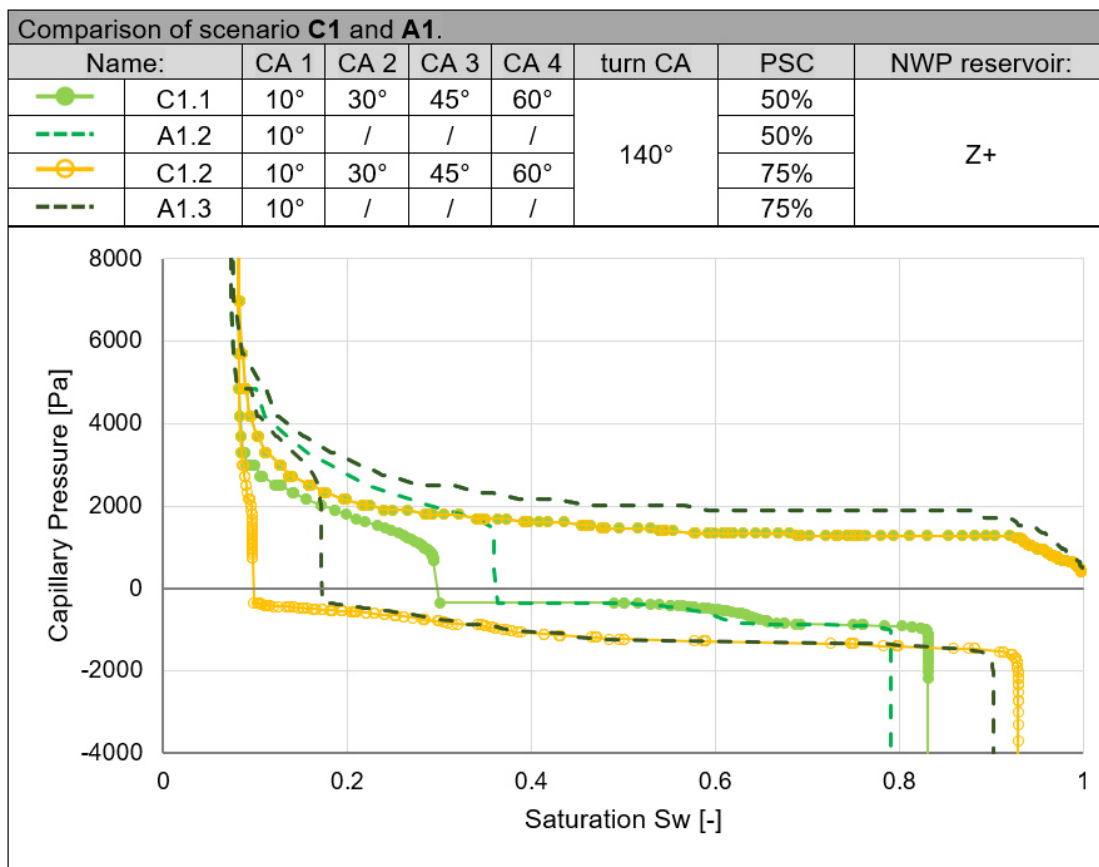


Figure 4-10 Comparison of scenario C1 and A1.

The second scenario focuses on the effect of different turning CA and is therefore comparable to scenario A3. It can be assumed that the same trends can be observed, although the different numbers and spatial distribution are likely to cause a difference. Table 13 shows the input to the individual simulations.

Table 13 Case C, Scenario C2.

| C2: Multiple CA, different turn CA. |      |      |      |      |         |      |                |
|-------------------------------------|------|------|------|------|---------|------|----------------|
| Name:                               | CA 1 | CA 2 | CA 3 | CA 4 | turn CA | PSC  | NWP reservoir: |
| C2.1                                | 10°  | 30°  | 45°  | 60°  | 120°    | 50 % | Z+             |
| C2.2                                |      |      |      |      | 140°    |      |                |
| C2.3                                |      |      |      |      | 170°    |      |                |

The simulation results show by and large the same trend as scenario A3 before. Since only the turning CA is changed in this scenario, there is no influence on the primary drainage and the effects are mainly visible for the forced imbibition part. The implementation of increasing turning CA values increases the OW tendency of the new materials. Thus, leading to larger areas above the forced imbibition curve, which in turn leads to a higher energy requirement to press the water into the structure. The decreasing WW tendency towards OW conditions is underpinned by the corresponding WIs. But also, for this scenario, the additional solid materials, and the considered angle range lead, as expected, to an additional influence on the computed results. The comparison with the single CA scenario (A3) not only shows the same general trend, but also shows a difference in the plateau heights of the primary drainage, the zero-crossing saturations in the imbibition curves, the resulting residual oil saturations, and respective WI values. The occurring changes and the respective WI values are provided in Table 14.

Table 14 Comparison of Scenario A3 & C2.

|             |                          |   |                          |             |
|-------------|--------------------------|---|--------------------------|-------------|
| Simulation: | Plateau h [ Pa ]:        |   | Plateau h [ Pa ]:        | Simulation: |
| A3          | $S_w 0.50 - S_w 0.85$    | → | $S_w 0.50 - S_w 0.85$    | C2          |
|             | 1932.8                   |   |                          | 1328.3      |
| Simulation: | $S_{zero-cross} [ 1 ]$ : |   | $S_{zero-cross} [ 1 ]$ : | Simulation: |
| A3          | 0.36                     | → | 0.30                     | C2          |
| Simulation: | $S_{OR} [ 1 ]$ :         |   | $S_{OR} [ 1 ]$ :         | Simulation: |
| A3.1        | 0.17                     | → | 0.10                     | C2.1        |
| A3.2        | 0.21                     | → | 0.17                     | C2.2        |
| A3.3        | 0.21                     | → | 0.18                     | C2.3        |
| Simulation: | WI [ - ]                 |   | WI [ - ]                 | Simulation: |
| A3.1        | 0.89                     | → | 0.50                     | C2.1        |
| A3.2        | 0.50                     | → | 0.14                     | C2.2        |
| A3.3        | 0.23                     | → | - 0.11                   | C2.3        |

On the one hand, these changes underpin the additional influence of additional solid materials and their associated CAs. Considering four solids and four individual CAs from the WW spectrum alter the prevailing wetting conditions in the direction of a more moderate WW environment. Thus, the computed curves are shifted more to the left side of the diagram compared to the single strong WW-CA case (A3). On the other hand, these changes capture the right physical behavior of decreasing WW tendency by increasing the OW characteristics of the implemented turning CA.

Figure 4-11 is illustrating the simulation results of this scenario and visualizes the described differences to the single CA case by direct comparison to scenario (A3).

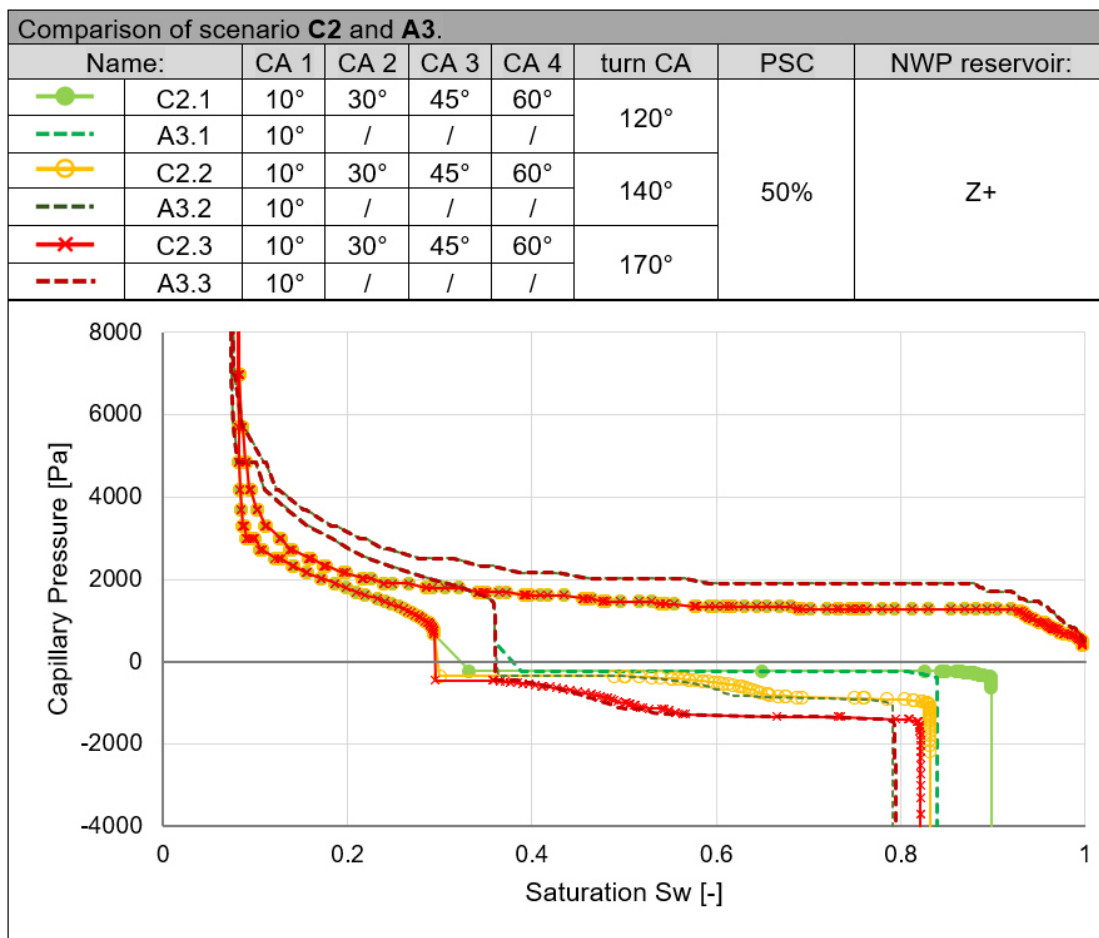


Figure 4-11 Comparison of scenario C2 and A3.

The last scenario of case C examines the influence of the implementation of the maximum possible amount of CA in the structure. As described in section 3.4, up to 8 different CAs can be assigned. Four are realized in the structure used from four solid materials, the other four as individual turning CA coupled to them. Table 15 shows the details for the two simulations of this scenario.



Table 15 Case C, Scenario C3.

| C3: 8 CA. |           |           |           |           |     |               |
|-----------|-----------|-----------|-----------|-----------|-----|---------------|
| Name:     | CA 1      | CA 2      | CA 3      | CA 4      | PSC | NWP reservoir |
| C3.1      | 10        | 20        | 30        | 40        | 50% | Z+            |
|           | turn CA 1 | turn CA 2 | turn CA 3 | turn CA 4 |     |               |
|           | 140       | 150       | 160       | 170       |     |               |
| C3.2      | 10        | 20        | 30        | 40        | 50% | Z+            |
|           | turn CA 1 | turn CA 2 | turn CA 3 | turn CA 4 |     |               |
|           | 170       | 160       | 150       | 140       |     |               |

The results of these two simulations show no visible difference. A simple change in the implemented range of the turning CA from (C3.1) to, conversely (C3.2) leads to computation of an almost identically capillary pressure curve. This observation ties in with the surface area analysis, described in section 3.5. Since the four OW materials newly introduced by the TORS algorithm have the same SVP of approximately 5% and an associated share of the surface area of approximately 12%, the influence on the computations is balanced. Thus, each implemented turning CA contributes equally to the computation regardless of the implemented sequence. Figure 4-12 shows the used structure before and after the application of the TORS algorithm and highlights the four newly generated materials. Since this is a 2D representation, it could look as if these were unevenly distributed, but Table 26 in appendix section A.2 confirms the equality that occurs.

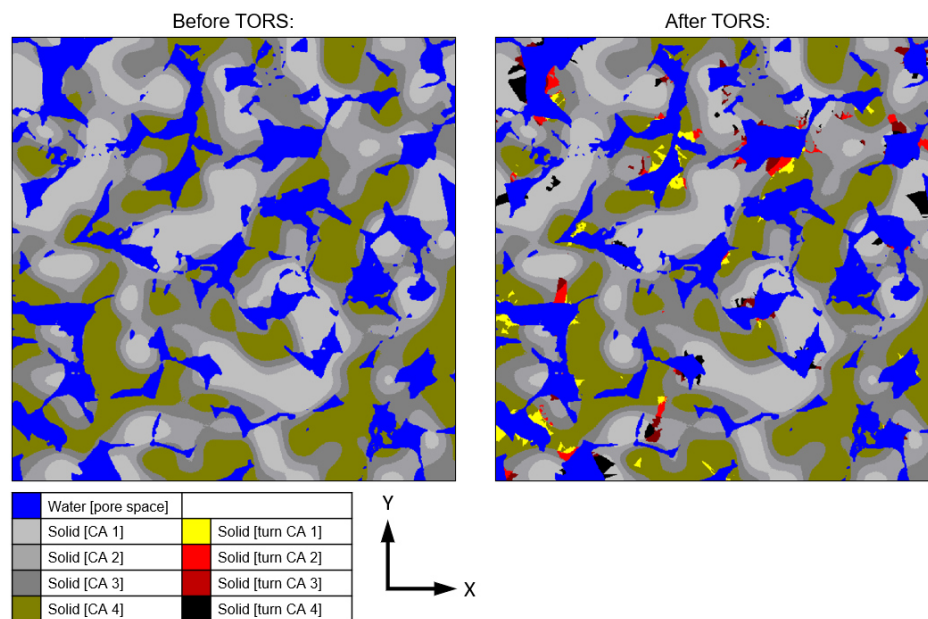


Figure 4-12 Case C, utilized structure before (left) and after (right) the applied TORS algorithm.

However, as shown in the previous cases and scenarios, the number of CAs present plays an important role. Therefore, when comparing the results with those of the single-turn CA scenario (C2), differences are observable.

These differences are related to the plateau height of the primary drainage, the zero-crossing saturation in the imbibition curve, the resulting residual oil saturation, and the corresponding WIs. These changes are listed in Table 16.

Table 16 Comparison of Scenario C2 & C3.

| Simulation: | Plateau h [ Pa ]:                         |                |          |   | Plateau h [ Pa ]:                         |                |          | Simulation: |
|-------------|---|----------------|----------|---|---|----------------|----------|-------------|
| C2.2        | S <sub>w</sub> 0.50 - S <sub>w</sub> 0.85 |                |          | → | S <sub>w</sub> 0.50 - S <sub>w</sub> 0.85 |                |          | C3.1 & C3.2 |
|             | 1328.3                                    |                |          |   | 1712.5                                    |                |          |             |
| Simulation: | S <sub>OR</sub> [ 1 ]:                    |                |          |   | S <sub>OR</sub> [ 1 ]:                    |                |          | Simulation: |
| C2.2        | 0.17                                      |                |          | → | 0.20                                      |                |          | C3.1 & C3.2 |
| Simulation: | S <sub>zero-cross</sub> [ 1 ]:            |                |          |   | S <sub>zero-cross</sub> [ 1 ]:            |                |          | Simulation: |
| C2.2        | 0.30                                      |                |          | → | 0.33                                      |                |          | C3.1 & C3.2 |
| Simulation: | A <sub>1</sub>                            | A <sub>2</sub> | WI [ - ] |   | A <sub>1</sub>                            | A <sub>2</sub> | WI [ - ] | Simulation: |
| C2.2        | 418.25                                    | 302.30         | 0.14     | → | 599.11                                    | 386.87         | 0.19     | C3.1        |
|             |   |                |          | → | 599.11                                    | 374.92         | 0.20     | C3.2        |

Increasing the number of turning CA is increasing both, the area underneath the spontaneous imbibition curve and the area above the forced imbibition, leading to a slightly higher positive WI.

On the one hand, it indicates that the coupling of the individual turning CAs to the respective materials leads to an uneven distribution of those within the structure. This indicates the emergence of regions with different OW tendencies, which in turn slightly reduce the overall OW tendency. In contrast to the Single Turning CA scenario (C2), in which only one new OW material is introduced for the oil-rock contacts and thus the entire OW tendency runs evenly over the structure. On the other hand, the slightly increased areas above the forced imbibition curves indicate a higher energy requirement to displace the oil. This is due to the higher attraction of the oil onto the newly introduced OW materials.

However, since both areas are slightly enlarged, the respective WI's are also enlarged somewhat. As a result, compared to scenario (C2), the computed curves are shifted more to the left in the direction of somewhat more moderate WW conditions. The implementation of the maximum possible amount of turning CA accordingly has a physically meaningful effect on the computations. Figure 4-13 presents the results of

the two simulations from this case and additionally illustrates the describes difference to the single turning CA case in a direct comparison with scenario (C2).

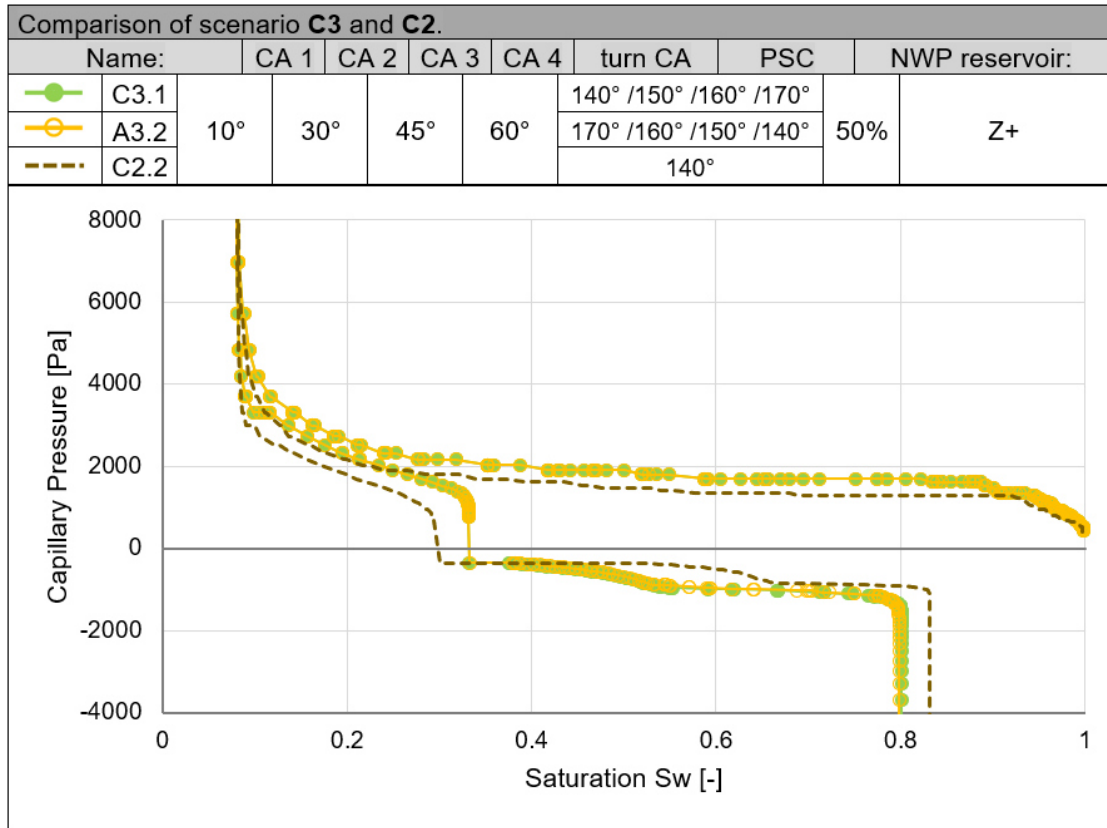


Figure 4-13 Comparison of scenario C3 and C2.

The results from case (C) support the observations from case (A). However, they show that the observed effects are intensified with an increasing number of solids and thus an increasing number of CAs. In addition, scenario (C3) indicates that the coupling of the individual turning CAs to the respective materials leads to an uneven distribution of the CAs within the structure. This indicates the emergence of regions with different OW tendencies, which in turn slightly reduce the total OW tendency.

## 4.5 Case D: Multiple solid materials, differing RS

Case D is to investigate the influence that is exerted when the expansion of the spatial distribution of four implemented CAs, based on four solid materials within a structure, is changed. To get an idea of the corresponding influences, this case is subjected to three scenarios.

### 4.5.1 Utilized structure

For this case, four structures, consisting out of four solid materials, are generated with the DCA algorithm described in section 3.2. In contrast to the previous cases, the creation of the structures now differs in terms of the region size applied to generate a deviation in the regional distribution of the individual solid materials.

To generate comparable scenarios, each structure shows the same volumetric share of solid materials and is based on the same random seed. As for the previous cases, the transition between the individual solid materials follows a smooth sequence. The corresponding input parameters for the DCA algorithm are enlisted in Table 17.

*Table 17 Case D, DCA input parameters of the utilized structures.*

| Structure: | Region Size:      | SVP:            | Random Seed: |
|------------|-------------------|-----------------|--------------|
| D 10       | 10 $\mu\text{m}$  | Each solid 25 % | 84           |
| D 50       | 50 $\mu\text{m}$  | Each solid 25 % |              |
| D 100      | 100 $\mu\text{m}$ | Each solid 25 % |              |
| D 500      | 500 $\mu\text{m}$ | Each solid 25 % |              |

Figure 4-14 shows these four structures together with the associated legend and perspective in a 2D representation.

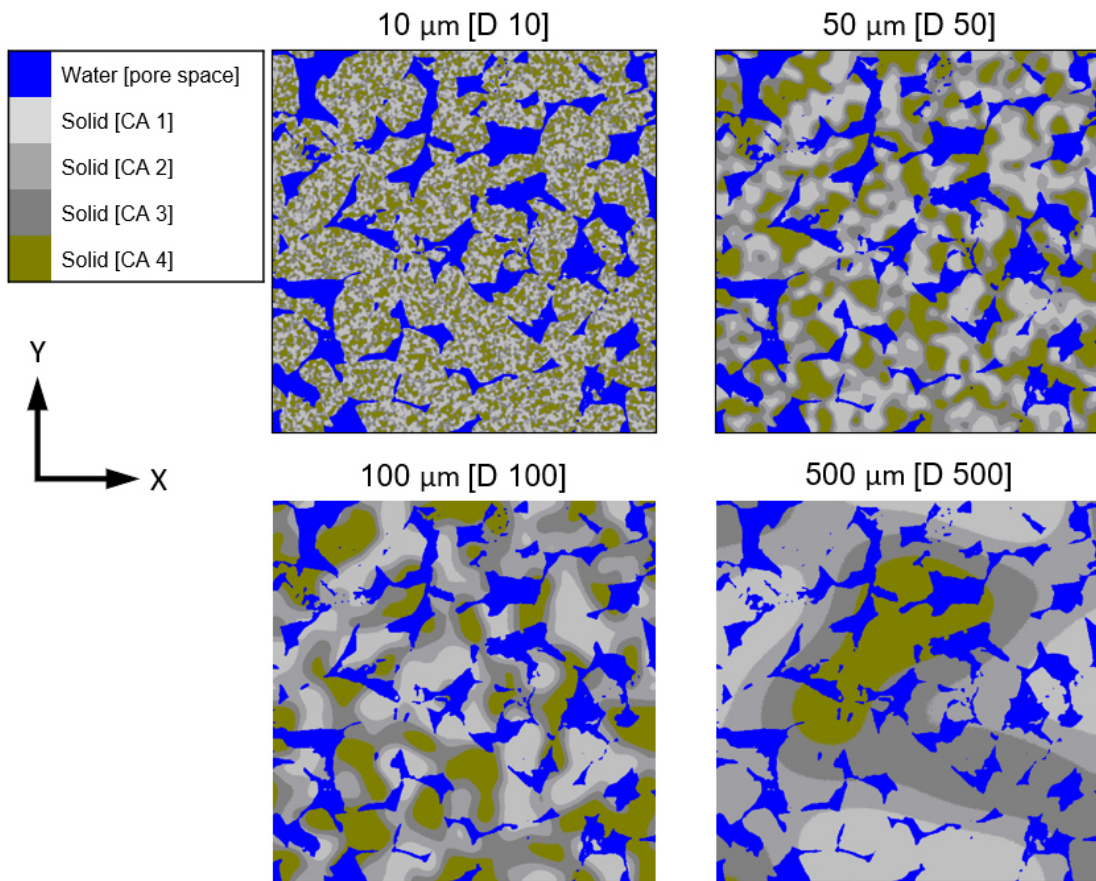


Figure 4-14 Utilized structures for Case D.

Here, too, the exact procedure for generating these structures follows the same principle as for the structures used in case B, which are explained in section A.1 of the appendix.

### 4.5.2 Simulated scenarios

As a first scenario, the four presented structures are subjected to the same simulation conditions. The aim is to determine whether the different spatial sizes of the respective solid phases have a correspondingly different influence on the computed capillary pressure curves. These simulation conditions are shown in Table 18.

Table 18 Case D, Scenario D1

| D1: Multiple CA, different region sizes. |            |      |      |      |      |         |      |                |
|--|------------|------|------|------|------|---------|------|----------------|
| Name:                                    | Structure: | CA 1 | CA 2 | CA 3 | CA 4 | turn CA | PSC  | NWP reservoir: |
| D1.1                                     | D 10       | 10°  | 30°  | 45°  | 60°  | 140     | 50 % | Z+             |
| D1.2                                     | D 50       |      |      |      |      |         |      |                |
| D1.3                                     | D 100      |      |      |      |      |         |      |                |
| D1.4                                     | D 500      |      |      |      |      |         |      |                |

The simulation results show less significant differences than the visualizations of the individual structures suggest. Although, the differing region sizes are affecting each hysteresis step. The main influences are exerted on both, the early phase of the primary drainage, and the residual oil saturations through the forced imbibition. But, in contrast to the other cases and scenarios, also a high influence on the connate water saturation is observable. The differences in the early phase of the primary drainage are most likely due to the different starting conditions. Or more precisely, how much of the individual solid materials are to be faced in the first few steps of the simulation, and thus how many different CA need to be considered in the computations. The influence exerted on the residual oil saturation is presumably based on the spatial distribution of individual solid materials as well. Since structure (D10) introduces a lot of wetting variation across the entire domain when compared to (D500) with its quite noticeable partitioning. The assumption here is that this variation brings a higher potential to trap the oil. According to the WI of (D1.1), the smaller region size is representing a slightly more WW environment than the larger region size. Therefore, the corresponding curve shows slightly stronger WW tendencies in relation to a higher zero-crossing saturation in the imbibition curve, a higher residual oil saturation, and a higher connate water saturation. While the simulations on the structures with a closer region size, especially recognizable for 50  $\mu\text{m}$  (D1.2) and 100  $\mu\text{m}$  (D1.3), come to similar results, a clear difference can be seen for the two extreme cases of 10  $\mu\text{m}$  (D1.1) and 500  $\mu\text{m}$  (D1.4). The influences exerted are in turn expressed in different plateau heights of the primary drainage, different zero-crossing saturations in the imbibition curves, different residual saturations, and the corresponding change in WI values. These changes and the respective WI values are provided in Table 19.

Table 19 Occurring changes & WI for Scenario D1.

| Occurring changes:   |                                       |                           |                   |                       |
|----------------------|---------------------------------------|---------------------------|-------------------|-----------------------|
| Simulation:          | Plateau h [ $S_w$ 0.50 – $S_w$ 0.85]: | $S_{\text{zero-cross}}$ : | $S_{\text{or}}$ : | $S_{\text{wc}}$ :     |
| Name:                | [ Pa ]                                | [ 1 ]                     | [ 1 ]             | [ 1 ]                 |
| D1.1                 | 1738.9                                | 0.34                      | 0.20              | 0.09                  |
| D1.2                 | 1494.5                                | 0.31                      | 0.18              | 0.09                  |
| D1.3                 | 1380.9                                | 0.30                      | 0.17              | 0.08                  |
| D1.4                 | 1250.3                                | 0.30                      | 0.16              | 0.07                  |
| Wettability Indices: |                                       |                           |                   |                       |
| Name:                | $A_1$                                 | $A_2$                     | $A_1/A_2$         | WI                    |
|                      | [ Area ]                              | [ Area ]                  | [ - ]             | $\text{Log}(A_1/A_2)$ |
| D1.1                 | 544.77                                | 277.04                    | 1.97              | 0.29                  |
| D1.2                 | 400.24                                | 297.17                    | 1.35              | 0.13                  |
| D1.3                 | 424.46                                | 302.17                    | 1.40              | 0.15                  |
| D1.4                 | 470.35                                | 310.64                    | 1.51              | 0.18                  |

Figure 4-15 shows the resulting capillary pressure curves of these simulations.

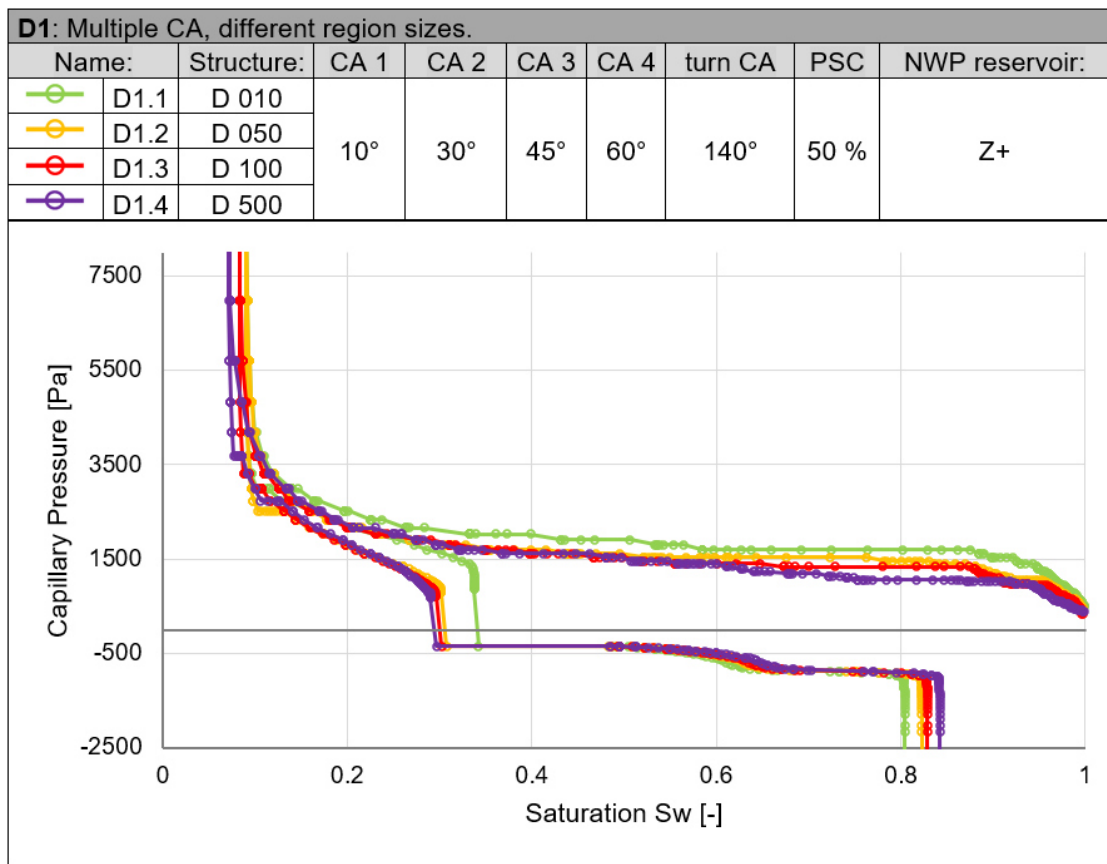


Figure 4-15 Case D, Scenario D1, Results.

Since the two extreme scenarios (10  $\mu\text{m}$  & 500  $\mu\text{m}$ ) lead to discernible differences, these two are further analyzed in the next scenario. Both structures differ greatly in their regional distribution and a change in process direction could affect the computations. Thus, this scenario goes in the same direction as previously scenario (A4), and a comparable trend is to be expected. The simulation details are listed in Table 20.

Table 20 Case D, Scenario D2.

| D2: Multiple CA, different NWP reservoir. |            |      |      |      |      |         |      |                |
|---|------------|------|------|------|------|---------|------|----------------|
| Name:                                     | Structure: | CA 1 | CA 2 | CA 3 | CA 4 | turn CA | PSC  | NWP reservoir: |
| D2.1                                      | D 10       | 10°  | 30°  | 45°  | 60°  | 140     | 50 % | Z+             |
| D2.2                                      |            |      |      |      |      |         |      | Z-             |
| D2.3                                      |            |      |      |      |      |         |      | X+             |
| D2.4                                      |            |      |      |      |      |         |      | Y+             |
| D2.5                                      | D 500      |      |      |      |      |         |      | Z+             |
| D2.6                                      |            |      |      |      |      |         |      | Z-             |
| D2.7                                      |            |      |      |      |      |         |      | X+             |
| D2.8                                      |            |      |      |      |      |         |      | Y+             |

The simulation results on the respective utilized structures show only small deviations for the covered process directions. Accordingly, trending in the same direction as scenario (A4) before.

As also these simulations on more complex structures come to comparable results, the previous statement on the influence of homogeneity from scenario (A4) is underpinned. Although, as expected, there is an observable difference between the simulations on the two utilized structures. The modification of the region sizes, and thus the regional distribution of the individual CA results in several impacts on the resulting curves. The plateau height of the primary drainage, the zero-crossing saturations in the imbibition curves, the residual oil saturations, the corresponding WI values, and the connate water saturations differ. The average changes are listed in Table 21.

*Table 21 Average difference between the simulation on D10 & D500.*

| Average difference:                  |        | Simulations on D10 |   | Simulations on D500 |
|--------------------------------------|--------|--------------------|---|---------------------|
| Plateau h ( $S_w 0.50 - S_w 0.85$ ): | [ Pa ] | 1719.1             | → | 1219.5              |
| $S_{OR}$ :                           | [ 1 ]  | 0.20               | → | 0.16                |
| $S_{zero-cross}$ :                   | [ 1 ]  | 0.34               | → | 0.30                |
| $S_{wc}$ :                           | [ 1 ]  | 0.09               | → | 0.07                |
| WI                                   | [ - ]  | 0.29               | → | 0.18                |

These differences lead to a slightly stronger WW tendency of the capillary pressure curves from the simulations that were carried out on structure (D10). However, these are most likely related to the different utilized region sizes and thus the effects observed in the previous scenario (D1) and not to the changed process directions.



Figure 4-16 shows the resulting capillary pressure curves for all simulations of this scenario.

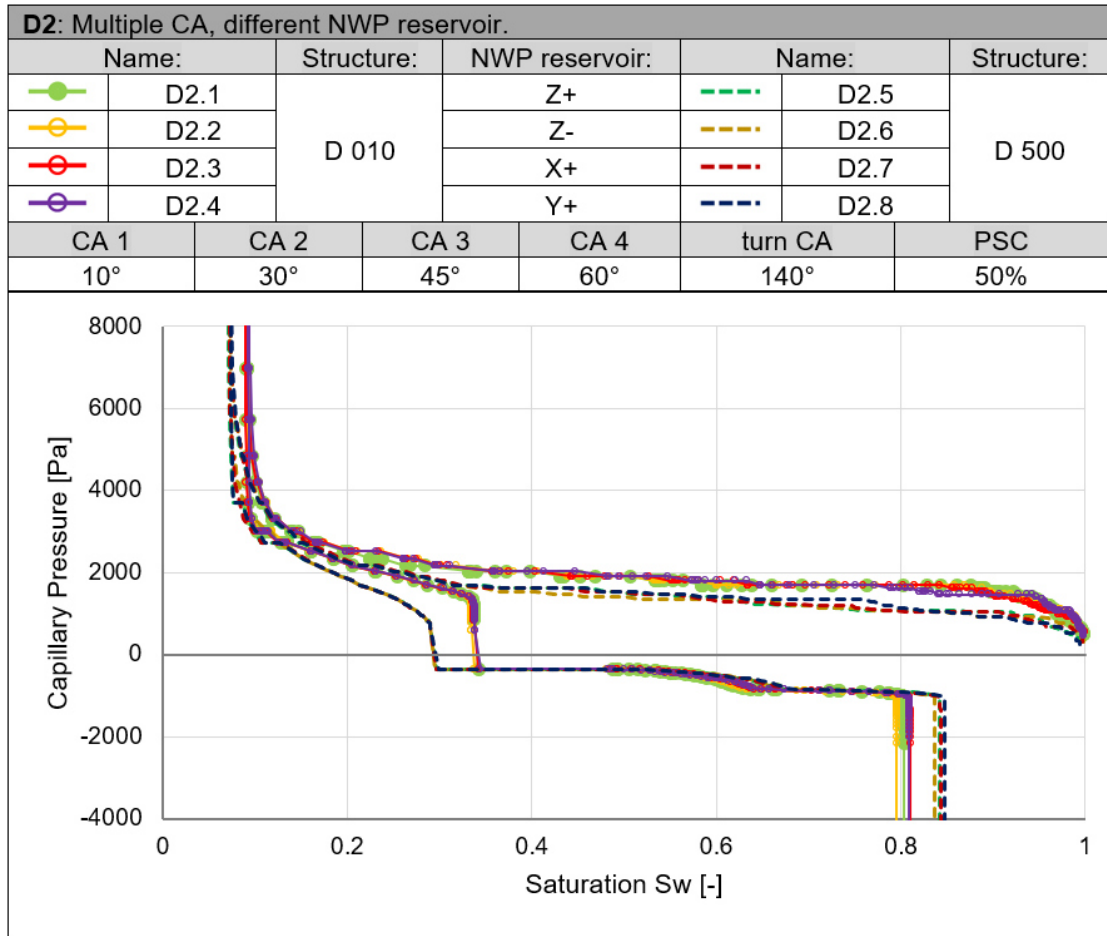


Figure 4-16 Case D, Scenario D2, Results.

A separate illustration of the resulting capillary pressure curves of both, the simulation on structure (D10) and structure (D500) is provided by Figure 6-6 and Figure 6-7, in appendix section B.2.

Considering the working principle of the DCA algorithm, with which the two utilized structures are generated, not only does the region size influence the different spatial distribution of new solids, but also the selected random seed.

Therefore, the next scenario introduces two new structures that were created with different random seeds (1 and 2). Which creates different realizations for the 500 μm structure (D500). Figure 4-17 visualizes these two next to the so far used structure [D 500 (84)].

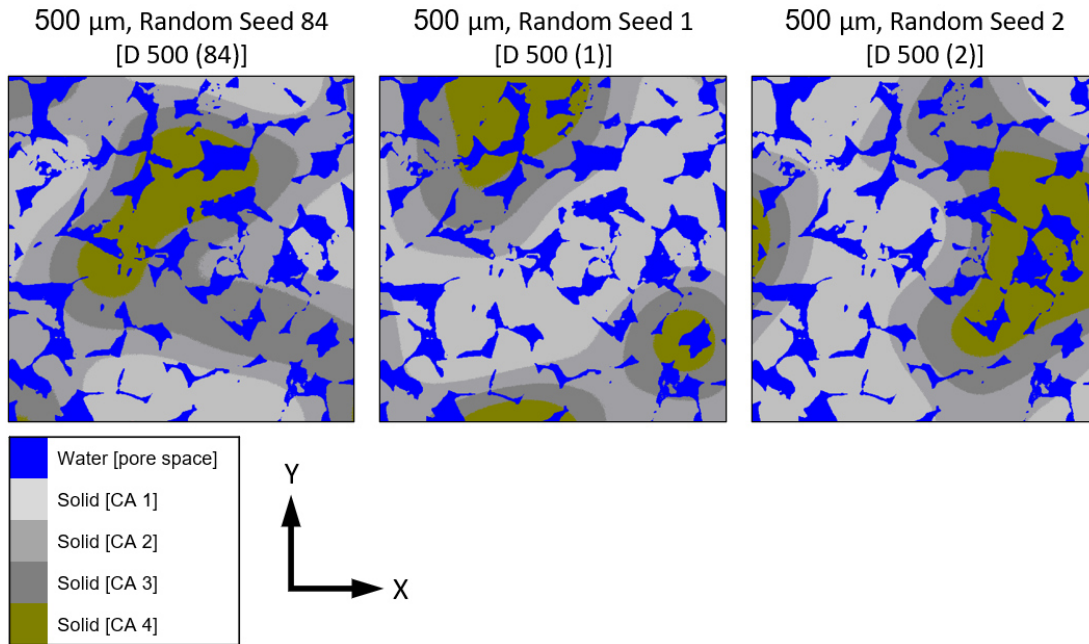


Figure 4-17 Case D, Scenario D3, Utilized structures.

This scenario aims to determine how these different realizations affect the computations. The implemented parameters from the individual simulations are shown in Table 22.

Table 22 Case D, Scenario D3.

| D3: Multiple CA, different random seed. |            |      |      |      |      |         |      |                |
|---|------------|------|------|------|------|---------|------|----------------|
| Name:                                   | Structure: | CA 1 | CA 2 | CA 3 | CA 4 | turn CA | PSC  | NWP reservoir: |
| D3.1                                    | D 500 (84) | 10°  | 30°  | 45°  | 60°  | 140     | 50 % | Z+             |
| D3.2                                    | D 500 (1)  |      |      |      |      |         |      |                |
| D3.3                                    | D 500 (2)  |      |      |      |      |         |      |                |

The results of these simulations show that an altered realization according to a varying random seed does not have a strong influence on the computations. However, there is a slight deviation in the early phase of the primary drainage and an observable influence on the individual residual oil saturations. So, the results are somehow comparable to scenarios (D1) and (A4). These occurrences are also most likely due to the changed initial conditions in the first steps of the simulation process and to the changed trapping potential. This is due to the different spatial distribution and expansion of the individual solid materials.

On the one hand, this repeated observation indicates that different invasion routes arise due to the different spatial distributions. But on the other hand, the repeatedly observed minor deviations on the capillary pressure curve underpin the homogeneity

of structure used. Which ultimately reduces the range of possible capillary pressures and leads to similar values regardless of the spatial variations introduced.

The resulting capillary pressure curves of this scenario are illustrated in Figure 4-18.

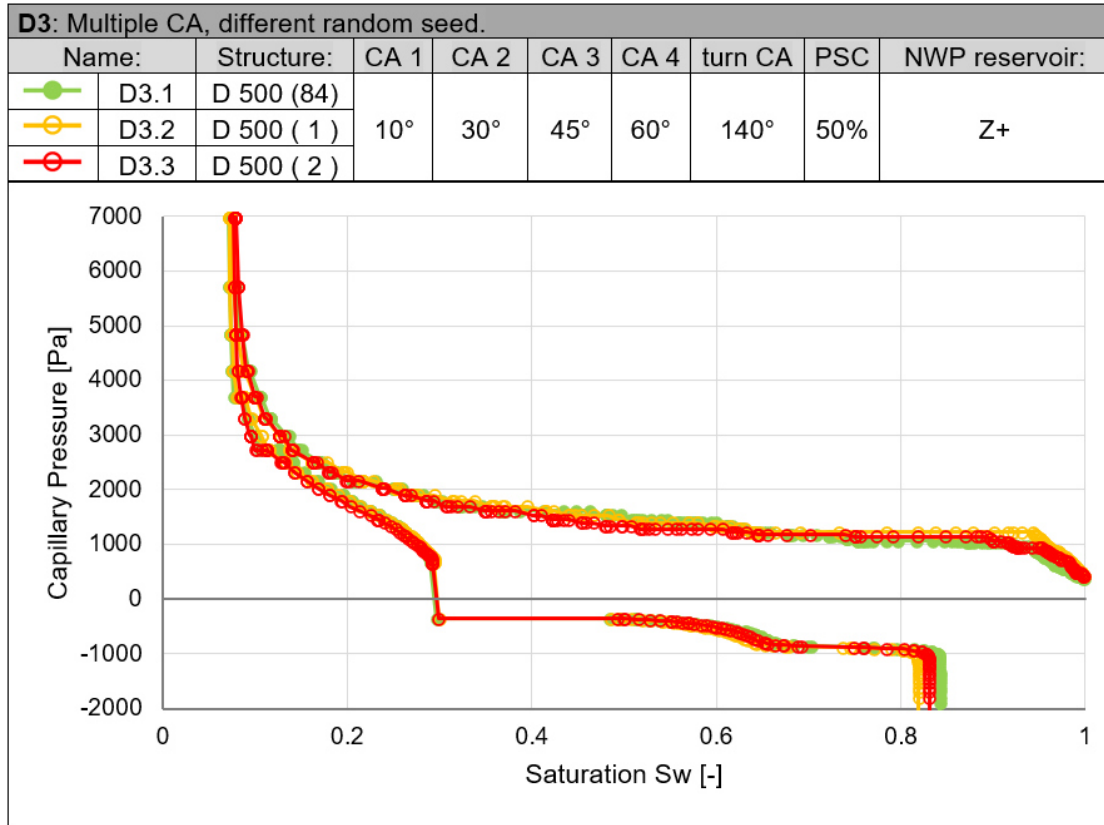


Figure 4-18 Case D, Scenario D3, Results.

The results from case (D) show that the different spatial distributions of solid regions and thus of individual contact angles affect the simulations. These effects influence residual saturations, pressure plateau heights for the primary drainage, and zero-crossing in the imbibition curve. But in contrast to the other cases, the highest influence can be observed on the connate water saturation. The changes that occur relate to the allocation of regions with differing wetting conditions, which ultimately influences the invasion sequence. Decreasing the region size leads to a mitigation of the heterogeneous effects due to the broad distribution of the CA. However, the homogeneity of the structure only leads to minor changes in the capillary pressure curves due to the similar energy requirements for displacing the oil.

## 4.6 Case E: Distinct spatial separation

To better understand the influences of the spatial distribution of different CAs, these are examined using a somewhat simpler setup. Therefore, this case is based on a certain set of structures that contain two solid materials with distinct spatial separation.

### 4.6.1 Utilized structure

In this case, six modifications of the original structure are used, each of which contains a layer located in different positions within the domain. This layer of each structure makes up 50% of the total solid material and shows a clear boundary between the two solid materials. These structures are named after the corresponding position of the layer and are shown in Figure 4-19 with material legend and perspective.

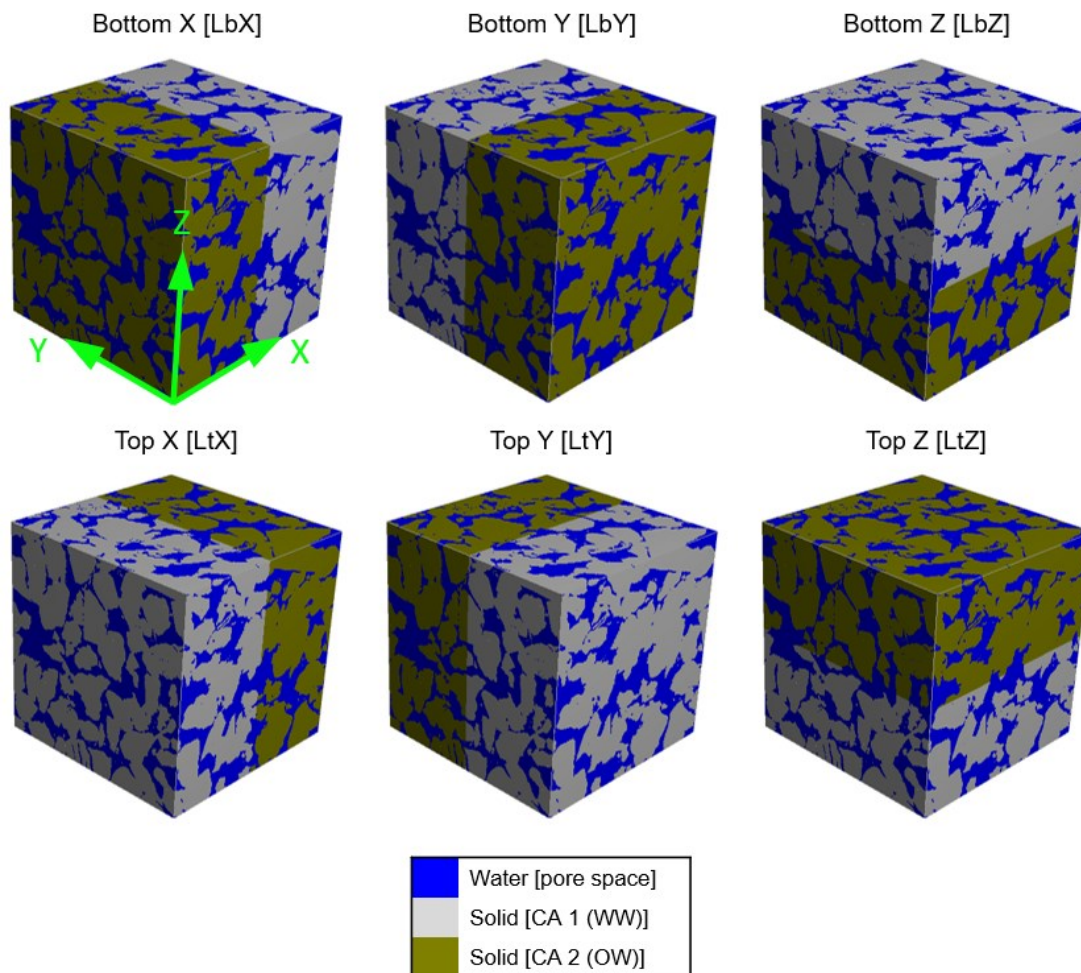


Figure 4-19 Case E, utilized structures.

### 4.6.2 Simulated scenario

To keep the scenario simple, and to really observe the impact extended by the different layer locations, the six structures are subjected to the same simulation conditions, which are enlisted in Table 23.

Table 23 Case E, Scenario E2.

| E1: Distinct spatial separation. |            |      |      |         |      |                |
|----------------------------------|------------|------|------|---------|------|----------------|
| Name:                            | Structure: | CA 1 | CA 2 | turn CA | PSC  | NWP reservoir: |
| E2.1                             | LbX        | 10°  | 60°  | 140°    | 50 % | Z+             |
| E2.2                             | LbY        |      |      |         |      |                |
| E2.3                             | LbZ        |      |      |         |      |                |
| E2.4                             | LtX        |      |      |         |      |                |
| E2.5                             | LtY        |      |      |         |      |                |
| E2.6                             | LtZ        |      |      |         |      |                |

The results of these six simulations show recognizable trends for the respective layer locations. While all the computed results are in proximity, one simulation is strongly deviating from the rest. This deviating simulation is the one with the layer located at the bottom of the Z-axis (LbZ). The corresponding result shows a higher plateau of the primary drainage remaining constant until reaching a water saturation of about (0.40). Additionally, the related spontaneous imbibition shows a steep decline followed by a short plateau, resulting in a zero-crossing saturation of about (0.24). Compared to the other simulations, also the residual oil saturation is decreased by about 4 % to (0.13).

Considering the hysteresis sequence with the associated locations of the WP and NWP reservoirs, described in section 3.4, this occurrence follows a logical trend. In contrast to the other structures, the layer at the bottom of the Z-axis creates a strong WW zone, due to the assigned CA of (10°), in the upper half of the structure. As the NWP reservoir for the primary drainage is located above this zone, it must be dealt with first. Once the capillary pressure is built up, it remains constant until the transition to the next zone with the more moderate WW conditions is reached. At this point, the simulation ties in with the others till the primary drainage is completed. Since the following spontaneous imbibition run is not changing the WP and NWP reservoir locations, the process is first facing the more moderate WW conditions of (60°). Which in turn explains the initial steep decline. Once the process reaches the transition to the upper, strongly WW, zone, a plateau is forming until the spontaneous part is completed. As the forced imbibition is conducted as a drainage process, with the reservoirs set up accordingly, but a changed invading phase from oil to water, the computed process is resulting in a lower residual oil saturation. This is due to the lower

trapping potential of this structural setup. Accordingly, the rest of the simulations on the other respective structures, follows a logical trend as well, with the difference of not having this strong WW zone across the respective process direction. The proximity of these simulations is most likely based on the homogeneity of the original structure. These observations go hand in hand with the calculated WI values of the respective simulations. Except for the simulation (LbZ), each of them shows a moderate WW tendency. Simulation (LbZ) is the only one with a negative WI and thus shows OW characteristics. Which, in turn, ties in with the previous explanation. The respective WI values are listed in Table 24.

*Table 24 Wettability indices Scenario E1.*

| Name: | A <sub>1</sub> | A <sub>2</sub> | A <sub>1</sub> /A <sub>2</sub> | WI                                   |
|-------|----------------|----------------|--------------------------------|--------------------------------------|
| /     | [ Area ]       | [ Area ]       | [ - ]                          | Log(A <sub>1</sub> /A <sub>2</sub> ) |
| LbX   | 478.89         | 310.65         | 1.54                           | 0.19                                 |
| LbY   | 488.18         | 311.12         | 1.57                           | 0.20                                 |
| LbZ   | 186.02         | 343.04         | 0.54                           | -0.27                                |
| LtX   | 469.41         | 315.38         | 1.49                           | 0.17                                 |
| LtY   | 451.17         | 312.32         | 1.44                           | 0.16                                 |
| LtZ   | 472.14         | 313.15         | 1.51                           | 0.18                                 |

Figure 4-20 illustrates all the simulation results of this scenario and clearly visualizes the observations described.

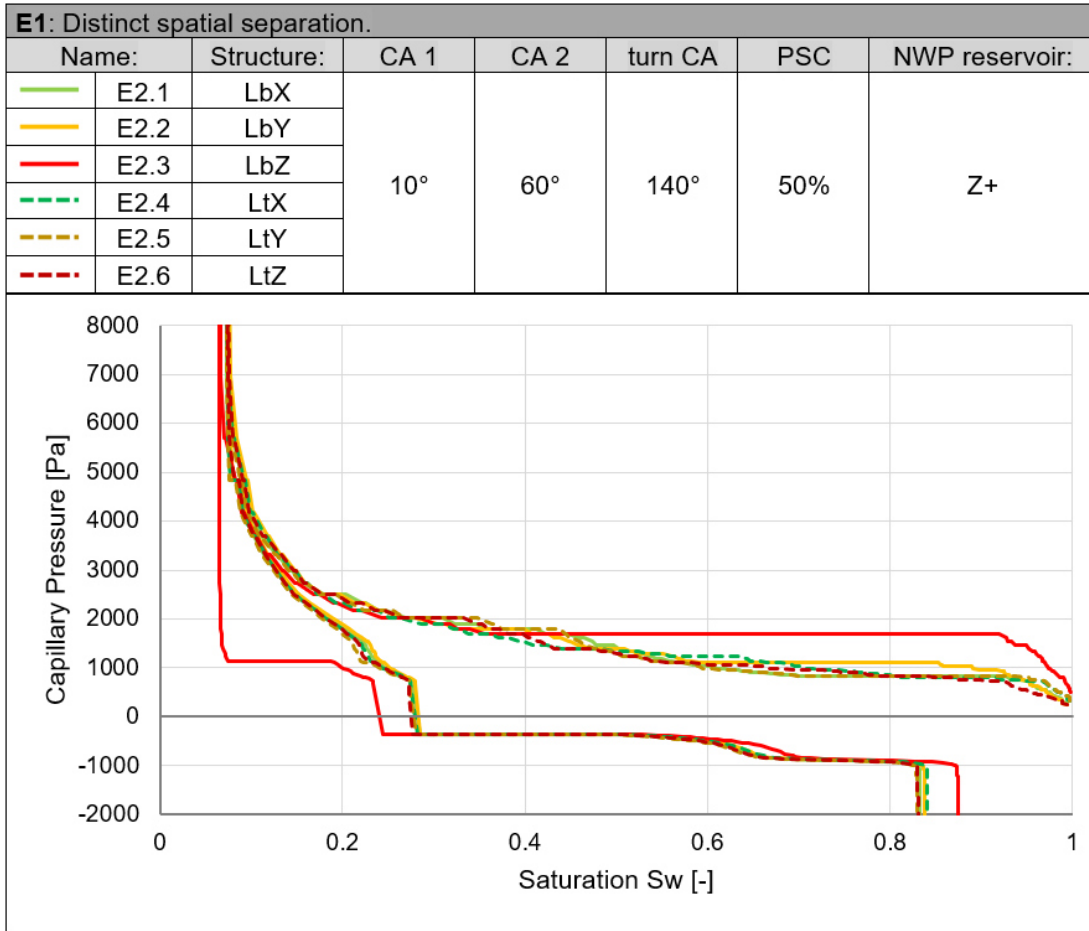


Figure 4-20 Case E, Scenario E1, Results.





# Chapter 5

## Conclusion

### 5.1 Summary

The achievement of realistic relative-permeability and capillary-pressure saturation functions crucially depends on the respective fluid distributions within the investigated pore structure. A common method of obtaining those is the morphological approach. However, its applicability has so far met limitations when the aim is to determine the forced portion of imbibition and the spontaneous portion of drainage of a capillary pressure curve. Therefore, this thesis presents a new approach, based on three recently implemented features in the software toolbox GeoDict.

The combination of these implemented features introduces, on the one hand, the possibility to mimic forced imbibition as an inverse drainage process, thus extending the achievable saturation range. On the other hand, it allows the introduction of multiple contact angles to study the impact of contact angle distribution and its spatial correlation.

The presented simulation results show that this new approach can model the saturation distributions and thus compute the corresponding capillary pressure curves.

The first simulation case (A) presents the most influential parameters of this new implementations, the implemented PSC value and the chosen CA, and their respective impacts on the varying simulation conditions. The results show that the modification of these parameters always introduces an alteration of the prevailing wetting conditions, which in turn are captured correctly within the simulation process. Hence, modifying the prevailing wetting conditions from strongly WW to more moderate WW results in capillary pressure curves depicting the right physical behavior. The indicators are a lower pressure plateau for the primary drainage, a lower zero-crossing saturation in

the imbibition curve, and lower residual oil saturation. Furthermore, the respective wettability indices show the right trend. In contrast, the spatial modifications of the boundary layers show only minor influence due to the homogeneity of the structure.

The simulations of cases (B) and (C) investigate the influence of the mentioned parameters, but on more complex structural modifications. These structures consist out of up to four solid materials, coupled with four individual CA, and thus introduce different wetting conditions based on different contact angle distributions and spatial variations. The corresponding results show the same trends as for the previous case A, but with the difference that the newly introduced increasing number of CAs within the structure is exerting additional influence on the computations. Consequently, the accounting for multiple CA covering a whole spectrum of WW angular range is further decreasing the WW tendency of the resulting capillary pressure curves. Since the prevailing wetting conditions are altered even more.

As the last step, cases (D) and (E) examine the influences occurring due to differing spatial and extensional distribution of individual solid materials and their associated CA. The results from case (D) show corresponding influences on residual saturations, pressure plateau heights for the primary drainage and zero-crossing in the imbibition curve. But in contrast to the other cases the highest influence can be observed on the connate water saturation. The changes that occur relate to the allocation of regions with differing wetting conditions, which ultimately influences the invasion sequence. Decreasing the region size leads to a mitigation of the heterogeneous effects due to the broad distribution of the CA. However, the homogeneity of the structure only leads to minor changes in the capillary pressure curves due to the similar energy requirements for displacing the oil. The results from case (E) show the strong influence of the spatial arrangement of the respective solids and CAs. In addition, they show that this new approach follows a logical physical trend in dealing with clearly separated arrangements.

Overall, this new approach captures important physical trends and points in the right direction, although it is still in its infancy and further studies are required to fully confirm both the accuracy and the physical correctness of the generated results.

## 5.2 Future work

The simulation cases and scenarios covered in this thesis are intended to serve as a starting point for further investigations. The provided information and data show that this new approach is quite able to model multi-phase flow saturation functions and thus to compute capillary pressure curves in a physically meaningful way. But there are remaining issues that need further attention.

First, the approach is to be tested on digital structures of different rock types with various degrees of heterogeneity to investigate the influences shown for structures with different pore throat sizes and thus allow for varying capillary pressure ranges. For such further investigations, the question of the representative elementary volume (REV) must also be clarified. The simulations within the scope of this work do not meet the REV criteria and therefore only provide basic information about the functionality and the reflected physical behavior.

Second, the introduction of different wetting conditions based on the varying number, region sizes, and distributions of individual CAs needs to be further refined. The DCA and TORS algorithms are not yet able to model scenarios with discrete CA and thus only generate continuous CA distributions.

And finally, it must be checked whether the results generated with this approach represent a meaningful basis for further DRP applications. Typically, these two-phase flow saturation functions are used as the basis for relative permeability simulations due to the corresponding relationship. A detailed study should clarify whether this approach can be used as a starting point to obtain meaningful and realistic data on relative permeability. Since these are specifically required for many processes in the field of Reservoir Engineering and their classic determination is time-consuming and labor-intensive.



# Chapter 6

## References

- Ahrenholz, B., Tölke, J., Lehmann, P., Peters, A., Kaestner, A., Krafczyk, M. & Durner, W. (2008). Prediction of capillary hysteresis in a porous material using lattice-Boltzmann methods and comparison to experimental data and a morphological pore network model. *Advances in Water Resources*, 31(9), 1151–1173. <https://doi.org/10.1016/j.advwatres.2008.03.009>
- Andrä, H., Combaret, N., Dvorkin, J., Glatt, E., Han, J., Kabel, M., Keehm, Y., Krzikalla, F., Lee, M., Madonna, C., Marsh, M., Mukerji, T., Saenger, E. H., Sain, R., Saxena, N., Ricker, S., Wiegmann, A. & Zhan, X. (2013). Digital rock physics benchmarks—Part I: Imaging and segmentation. *Computers & Geosciences*, 50, 25–32. <https://doi.org/10.1016/j.cageo.2012.09.005>
- Berg, S., Rücker, M., Ott, H., Georgiadis, A., van der Linde, H., Enzmann, F., Kersten, M., Armstrong, R. T., With, S. de, Becker, J. & Wiegmann, A. (2016). Connected pathway relative permeability from pore-scale imaging of imbibition. *Advances in Water Resources*, 90, 24–35. <https://doi.org/10.1016/j.advwatres.2016.01.010>
- Blunt, M. J. (2001). Flow in porous media — pore-network models and multiphase flow. *Current Opinion in Colloid & Interface Science*, 6(3), 197–207. [https://doi.org/10.1016/S1359-0294\(01\)00084-X](https://doi.org/10.1016/S1359-0294(01)00084-X)
- Blunt, M. J. (2017). *Multiphase Flow in Permeable Media*. Cambridge University Press. <https://doi.org/10.1017/9781316145098>
- Boas, F. E. & Fleischmann, D. (2012). CT artifacts: causes and reduction techniques. *Imaging in Medicine*, 4(2), 229–240. <https://doi.org/10.2217/IIM.12.13>
- Brown, H. W. (1951). Capillary Pressure Investigations. *Journal of Petroleum Technology*, 3(03), 67–74. <https://doi.org/10.2118/951067-G>

- Chen, S. & Doolen, G. D. (1998). LATTICE BOLTZMANN METHOD FOR FLUID FLOWS. *Annual Review of Fluid Mechanics*, 30(1), 329–364. <https://doi.org/10.1146/annurev.fluid.30.1.329>
- Cuevas, E., Zaldivar, D. & Pérez-Cisneros, M. (2010). A novel multi-threshold segmentation approach based on differential evolution optimization. *Expert Systems with Applications*, 37(7), 5265–5271. <https://doi.org/10.1016/j.eswa.2010.01.013>
- D. Koroteev, O. Dinariev, N. Evseev, D. Klemin, A. Nadeev, S. Safonov, O. Gurpinar, S. Berg, C. V. Kruijsdijk, R. Armstrong, M. Myers, L. Hathon & H. D. Jong (2014). Direct Hydrodynamic Simulation of Multiphase Flow in Porous Rock. *Petrophysics*, 55, 294–303.
- Dumore, J. M. & Schols, R. S. (1974). Drainage Capillary-Pressure Functions and the Influence of Connate Water. *Society of Petroleum Engineers Journal*, 14(05), 437–444. <https://doi.org/10.2118/4096-PA>
- Fatt, I. (1956). The Network Model of Porous Media. *Transactions of the AIME*, 207(01), 144–181. <https://doi.org/10.2118/574-G>
- Ferrari, A. & Lunati, I. (2013). Direct numerical simulations of interface dynamics to link capillary pressure and total surface energy. *Advances in Water Resources*, 57, 19–31. <https://doi.org/10.1016/j.advwatres.2013.03.005>
- Hilpert, M. & Miller, C. T. (2001). Pore-morphology-based simulation of drainage in totally wetting porous media. *Advances in Water Resources*, 24(3-4), 243–255. [https://doi.org/10.1016/S0309-1708\(00\)00056-7](https://doi.org/10.1016/S0309-1708(00)00056-7)
- Hussain, F., Pinczewski, W. V., Cinar, Y., Arns, J. Y., Arns, C. H. & Turner, M. L. (2014). Computation of Relative Permeability from Imaged Fluid Distributions at the Pore Scale. *Transport in Porous Media*, 104(1), 91–107. <https://doi.org/10.1007/s11242-014-0322-7>
- Laplace, P. S. (1805). *Traité de mécanique céleste* (4. Aufl.). Crapelet.
- Math2Market GmbH. SatuDict User Guide, 2021. <https://doi.org/10.30423/userguide.geodict2021-SatuDict>
- Mees, F., Swennen, R., van Geet, M. & Jacobs, P. (2003). Applications of X-ray computed tomography in the geosciences. Geological Society, London, Special Publications, 215(1), 1–6. <https://doi.org/10.1144/GSL.SP.2003.215.01.01>

- Pan, C., Hilpert, M. & Miller, C. T. (2004). Lattice-Boltzmann simulation of two-phase flow in porous media. *Water Resources Research*, 40(1). <https://doi.org/10.1029/2003WR002120>
- Pardo, A. (2011). Analysis of non-local image denoising methods. *Pattern Recognition Letters*, 32(16), 2145–2149. <https://doi.org/10.1016/j.patrec.2011.06.022>
- Sankur, B. (2004). Survey over image thresholding techniques and quantitative performance evaluation. *Journal of Electronic Imaging*, 13(1), 146. <https://doi.org/10.1117/1.1631315>
- Schulz, V. P., Wargo, E. A. & Kumbur, E. C. (2015). Pore-Morphology-Based Simulation of Drainage in Porous Media Featuring a Locally Variable Contact Angle. *Transport in Porous Media*, 107(1), 13–25. <https://doi.org/10.1007/s11242-014-0422-4>
- Schulz, V. P., Becker, J., Wiegmann, A., Mukherjee, P. P. & Wang, C.-Y. (2007). Modeling of Two-Phase Behavior in the Gas Diffusion Medium of PEFCs via Full Morphology Approach. *Journal of The Electrochemical Society*, 154(4), B419. <https://doi.org/10.1149/1.2472547>
- Shan & Chen (1993). Lattice Boltzmann model for simulating flows with multiple phases and components. *Physical review. E, Statistical physics, plasmas, fluids, and related interdisciplinary topics*, 47(3), 1815–1819. <https://doi.org/10.1103/PhysRevE.47.1815>
- Vogel, H.-J., Tölke, J., Schulz, V. P., Krafczyk, M. & Roth, K. (2005). Comparison of a Lattice-Boltzmann Model, a Full-Morphology Model, and a Pore Network Model for Determining Capillary Pressure-Saturation Relationships. *Vadose Zone Journal*, 4(2), 380–388. <https://doi.org/10.2136/vzj2004.0114>
- Wang, J., Zhang, L., Ge, K. & Dong, H. (2021). Capillary pressure in the anisotropy of sediments with hydrate formation. *Fuel*, 289, 119938. <https://doi.org/10.1016/j.fuel.2020.119938>
- Young, T. (1805). III. An essay on the cohesion of fluids. *Philosophical Transactions of the Royal Society of London*, 95, 65–87. <https://doi.org/10.1098/rstl.1805.0005>





# Appendix A

## Appendix Chapter 2

### A.1 Multiple solid structures with a smooth transition

To generate a structure consisting out of up to four solid materials with a smooth transitioning in between, the DCA algorithm is combined with the GeoDict modules ProcessGeo and LayerGeo. Thereby, following a simple three-step procedure:

#### Step 1:

First, the DCA algorithm is used to generate three individual structures with constant region size and random seed but differing SVP and related Material ID of the newly introduced sub-region. This step results in three different modifications of the original structure, where the respective newly introduced material has a different SVP and different material ID, illustrated by Figure 6-1.

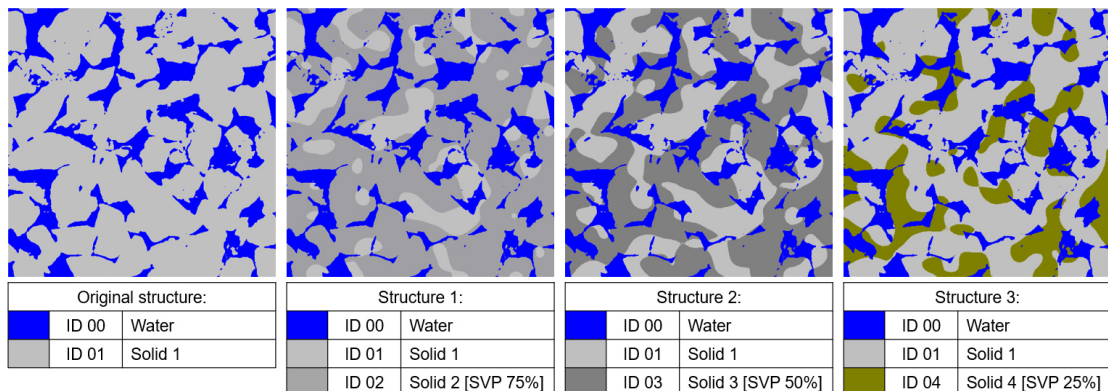


Figure 6-1 Step 1.

### Step 2:

As a next step, structure 2 and structure 3 from step 1, are subjected to the “Reassign Material ID” feature of the ProcessGeo module. Thereby, the rest of the preexisting solid material, ID 01, is reassigned to be material ID 00, hence water. This step results in the structure modifications showing again only two materials, and correspondingly the two related material IDs, illustrated by Figure 6-2.

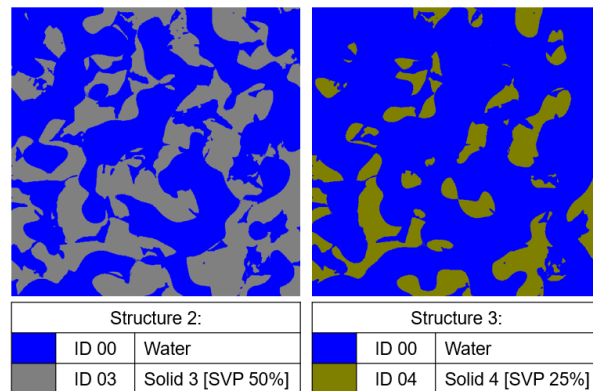


Figure 6-2 Step 2.

### Step 3:

For the final step, Structure 1 from step 1, consisting out of (ID 00: water), (ID 01: Solid 1), and (ID 02: Solid 2 [SVP 75%]), is required as a starting point. This step is utilizing the structures from step 2 within the “Add” feature of the LayerGeo module. Therein, it is possible to add a material according to its respective material ID. Hence, this step is adding, one after another, the individual materials with their corresponding SVP and material ID. Or more precisely, this step is stacking the individual materials onto the original structure in order according to their ID, illustrated by Figure 6-3.

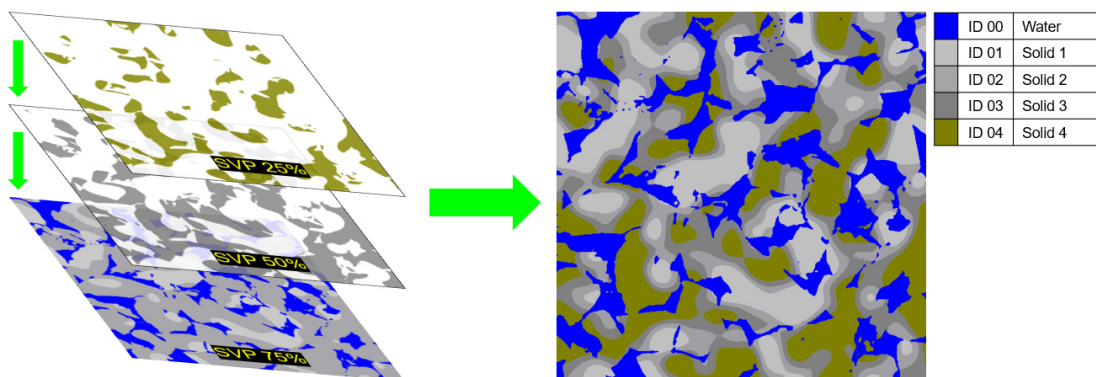


Figure 6-3 Step 3.

This step results in the desired structure modification showing four independent solid materials with a smooth transitioning between them. In case a structure consisting out

of three solid materials is desired, the same three-step procedure is used, but the respective SVP values must be adjusted accordingly.

## A.2 Surface Area Analysis

Table 25 Surface Area Analysis, DCA algorithm.

| Case:   | Structure: | Number of solids: | Region size:      | Solid ID: | SVP:    | Surface Area to pore space: | Surface Area percentage: |
|---------|------------|-------------------|-------------------|-----------|---------|-----------------------------|--------------------------|
|         | [ Name ]   |                   | [ $\mu\text{m}$ ] |           | [ % ]   | [ $\text{m}^2$ ]            | [ % ]                    |
| A       | original   | 1                 | /                 | Solid     | 100     | 2.27E-04                    | 100                      |
| B       | B1.2       | 2                 | 100               | Solid 1   | 50.1    | 1.12E-04                    | 49.5                     |
|         |            |                   |                   | Solid 2   | 49.9    | 1.15E-04                    | 50.5                     |
|         | B1.3       | 3                 | 100               | Solid 1   | 34.3    | 7.63E-05                    | 33.7                     |
|         |            |                   |                   | Solid 2   | 32.9    | 7.46E-05                    | 32.9                     |
|         |            |                   |                   | Solid 3   | 32.9    | 7.57E-05                    | 33.4                     |
|         | B / C      | B1.4              | 4                 | 100       | Solid 1 | 25.1                        | 5.61E-05                 |
| Solid 2 |            |                   |                   |           | 25.0    | 5.60E-05                    | 24.7                     |
| Solid 3 |            |                   |                   |           | 24.8    | 5.67E-05                    | 25.0                     |
| Solid 4 |            |                   |                   |           | 25.0    | 5.79E-05                    | 25.5                     |
| D       | D 10       | 4                 | 10                | Solid 1   | 24.9    | 5.64E-05                    | 24.9                     |
|         |            |                   |                   | Solid 2   | 24.9    | 5.65E-05                    | 24.9                     |
|         |            |                   |                   | Solid 3   | 25.0    | 5.66E-05                    | 25.0                     |
|         |            |                   |                   | Solid 4   | 25.2    | 5.71E-05                    | 25.2                     |
|         | D 50       | 4                 | 50                | Solid 1   | 25.0    | 5.61E-05                    | 24.7                     |
|         |            |                   |                   | Solid 2   | 24.9    | 5.66E-05                    | 25.0                     |
|         |            |                   |                   | Solid 3   | 25.0    | 5.71E-05                    | 25.2                     |
|         |            |                   |                   | Solid 4   | 25.1    | 5.69E-05                    | 25.1                     |
|         | D 100      | 4                 | 100               | Solid 1   | 24.8    | 5.61E-05                    | 24.8                     |
|         |            |                   |                   | Solid 2   | 24.9    | 5.60E-05                    | 24.7                     |
|         |            |                   |                   | Solid 3   | 25.1    | 5.67E-05                    | 25.0                     |
|         |            |                   |                   | Solid 4   | 25.2    | 5.79E-05                    | 25.5                     |
|         | D 500      | 4                 | 500               | Solid 1   | 25.1    | 5.96E-05                    | 26.3                     |
|         |            |                   |                   | Solid 2   | 24.5    | 5.71E-05                    | 25.2                     |
|         |            |                   |                   | Solid 3   | 24.9    | 5.68E-05                    | 25.1                     |
|         |            |                   |                   | Solid 4   | 25.4    | 5.31E-05                    | 23.4                     |

Table 26 Surface Area Analysis after TORS, 50 % PSC.

| Case: | Structure: | Number of solids: | Region size:      | Solid ID:    | SVP:  | Surface Area to pore space: | Surface Area percentage: |
|-------|------------|-------------------|-------------------|--------------|-------|-----------------------------|--------------------------|
|       | [ Name ]   |                   | [ $\mu\text{m}$ ] |              | [ % ] | [ $\text{m}^2$ ]            | [ % ]                    |
| A     | original   | 1                 | /                 | Solid        | 100   | 2.27E-04                    | 100                      |
| B     | B1.2       | 2 + 1 turn        | 100               | Solid 1      | 47.7  | 9.87E-05                    | 43.6                     |
|       |            |                   |                   | Solid 2      | 47.4  | 1.01E-04                    | 44.5                     |
|       |            |                   |                   | Solid turn   | 4.9   | 2.71E-05                    | 12.0                     |
|       | B1.3       | 3 + 1 turn        | 100               | Solid 1      | 32.5  | 6.73E-05                    | 29.7                     |
|       |            |                   |                   | Solid 2      | 31.3  | 6.55E-05                    | 28.9                     |
|       |            |                   |                   | Solid 3      | 31.3  | 6.67E-05                    | 29.4                     |
|       |            |                   |                   | Solid turn   | 4.9   | 2.72E-05                    | 12.0                     |
| B / C | B1.4       | 4 + 1 turn        | 100               | Solid 1      | 23.9  | 4.94E-05                    | 21.8                     |
|       |            |                   |                   | Solid 2      | 23.8  | 4.93E-05                    | 21.7                     |
|       |            |                   |                   | Solid 3      | 23.6  | 4.97E-05                    | 21.9                     |
|       |            |                   |                   | Solid 4      | 23.8  | 5.10E-05                    | 22.5                     |
|       |            |                   |                   | Solid turn   | 4.9   | 2.72E-05                    | 12.0                     |
| C     | B1.4       | 4 + 4turn         | 100               | Solid 1      | 23.8  | 4.94E-05                    | 21.8                     |
|       |            |                   |                   | Solid 2      | 23.8  | 4.93E-05                    | 21.7                     |
|       |            |                   |                   | Solid 3      | 23.6  | 4.97E-05                    | 21.9                     |
|       |            |                   |                   | Solid 4      | 23.8  | 5.10E-05                    | 22.5                     |
|       |            |                   |                   | Solid turn 1 | 1.2   | 6.83E-06                    | 3.0                      |
|       |            |                   |                   | Solid turn 2 | 1.2   | 6.97E-06                    | 3.1                      |
|       |            |                   |                   | Solid turn 3 | 1.2   | 6.68E-06                    | 2.9                      |
|       |            |                   |                   | Solid turn 4 | 1.3   | 6.67E-06                    | 2.9                      |
| D     | D 10       | 4 + 1 turn        | 10                | Solid 1      | 23.7  | 4.96E-05                    | 21.9                     |
|       |            |                   |                   | Solid 2      | 23.7  | 4.98E-05                    | 22.0                     |
|       |            |                   |                   | Solid 3      | 23.8  | 4.99E-05                    | 22.0                     |
|       |            |                   |                   | Solid 4      | 23.9  | 5.02E-05                    | 22.2                     |
|       |            |                   |                   | Solid turn   | 4.9   | 2.72E-05                    | 12.0                     |
|       | D 50       | 4 + 1 turn        | 50                | Solid 1      | 23.7  | 4.90E-05                    | 21.6                     |
|       |            |                   |                   | Solid 2      | 23.7  | 4.97E-05                    | 21.9                     |
|       |            |                   |                   | Solid 3      | 23.8  | 5.04E-05                    | 22.2                     |
|       |            |                   |                   | Solid 4      | 24    | 5.04E-05                    | 22.3                     |
|       |            |                   |                   | Solid turn   | 4.9   | 2.71E-05                    | 12.0                     |
|       | D 100      | 4 + 1 turn        | 100               | Solid 1      | 23.5  | 4.94E-05                    | 21.8                     |
|       |            |                   |                   | Solid 2      | 23.7  | 4.93E-05                    | 21.7                     |
|       |            |                   |                   | Solid 3      | 23.9  | 4.97E-05                    | 21.9                     |
|       |            |                   |                   | Solid 4      | 24.1  | 5.10E-05                    | 22.5                     |
|       |            |                   |                   | Solid turn   | 4.9   | 2.72E-05                    | 12.0                     |
|       | D 500      | 4 + 1 turn        | 500               | Solid 1      | 24.1  | 5.37E-05                    | 23.7                     |
|       |            |                   |                   | Solid 2      | 23.2  | 4.97E-05                    | 21.9                     |
|       |            |                   |                   | Solid 3      | 23.7  | 4.98E-05                    | 22.0                     |
|       |            |                   |                   | Solid 4      | 24.1  | 4.62E-05                    | 20.4                     |
|       |            |                   |                   | Solid turn   | 4.9   | 2.72E-05                    | 12.0                     |

Table 27 Surface Area Analysis after TORS, varying PSC.

| Case: | Structure: | Number of solids: | PSC:  | Solid ID:  | Surface Area to pore space: | Surface Area percentage: |
|-------|------------|-------------------|-------|------------|-----------------------------|--------------------------|
|       | [ Name ]   |                   | [ % ] |            | [ m <sup>2</sup> ]          | [ % ]                    |
|       | original   | 1                 |       | Solid      | 2.27E-04                    | 100                      |
| A     | original   | 1 + 1 turn        | 1     | Solid 1    | 2.27E-04                    | 100.0                    |
|       |            |                   |       | Solid turn | 0.00E+00                    | 0.0                      |
|       |            | 1 + 1 turn        | 50    | Solid 1    | 2.00E-04                    | 88.0                     |
|       |            |                   |       | Solid turn | 2.71E-05                    | 12.0                     |
|       |            | 1 + 1 turn        | 99    | Solid 1    | 7.08E-05                    | 31.3                     |
|       |            |                   |       | Solid turn | 1.56E-04                    | 68.7                     |

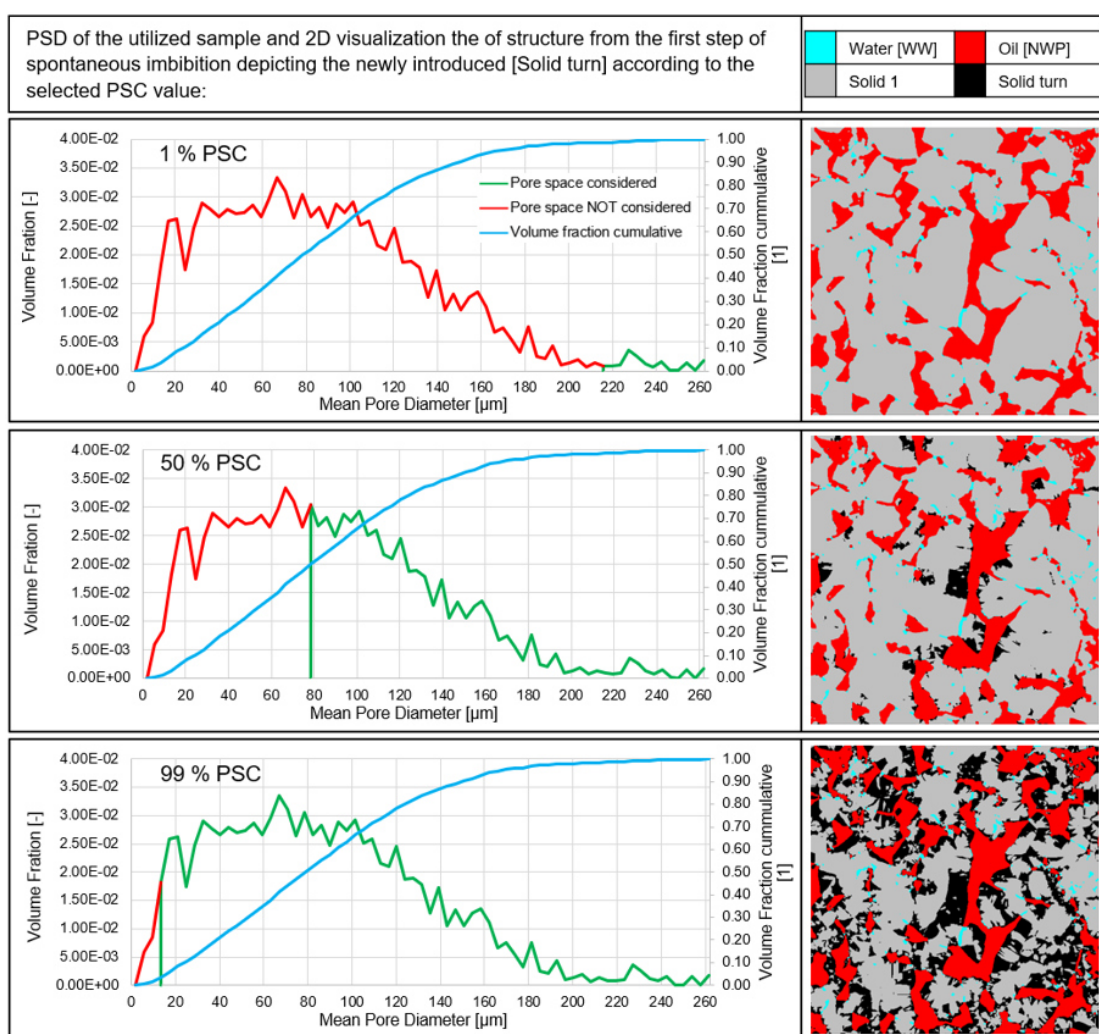


Figure 6-4 Influence of PSC value on newly introduced Solid material.



# Appendix B

## Appendix Chapter 4

This Appendix section provides additional illustrations of the conducted simulation cases and scenarios.

### B.1 Simulation results Case A, Scenario A4

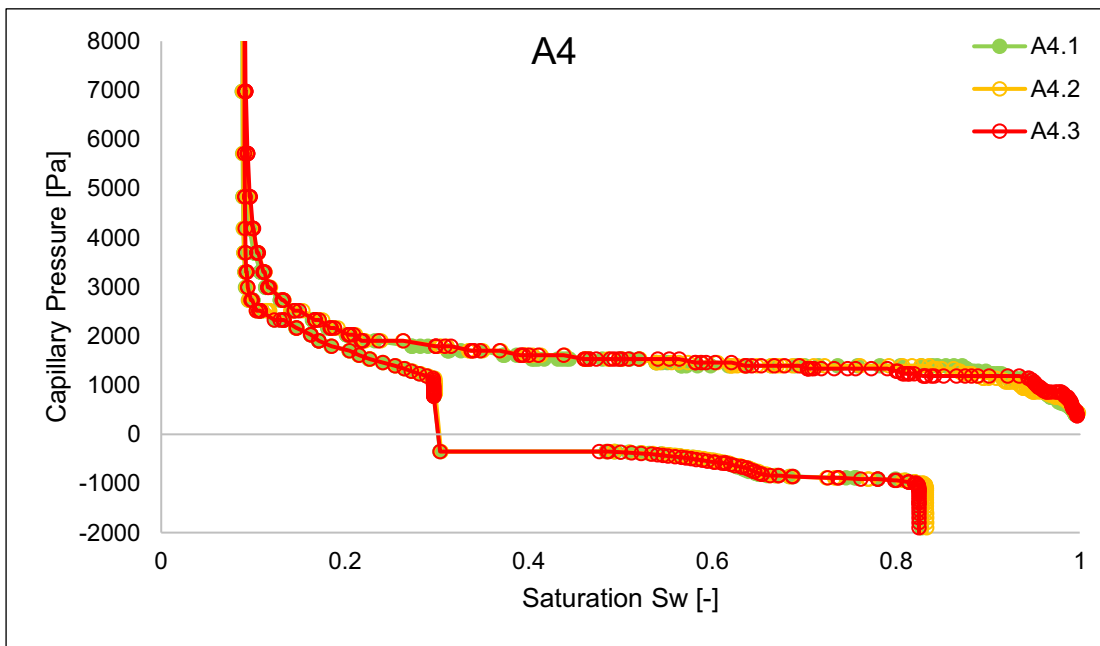


Figure 6-5 Case A, Scenario A4, Results, full view.

## B.2 Simulation results Case D, Scenario D2

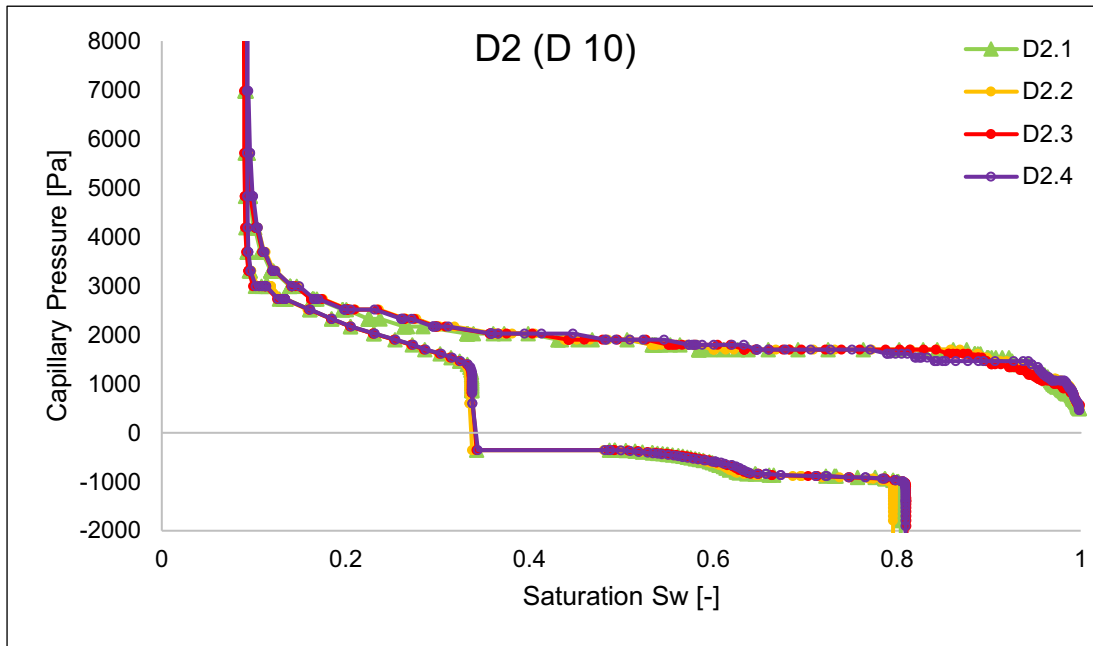


Figure 6-6 Case D, Scenario D2, Results on structure D 10.

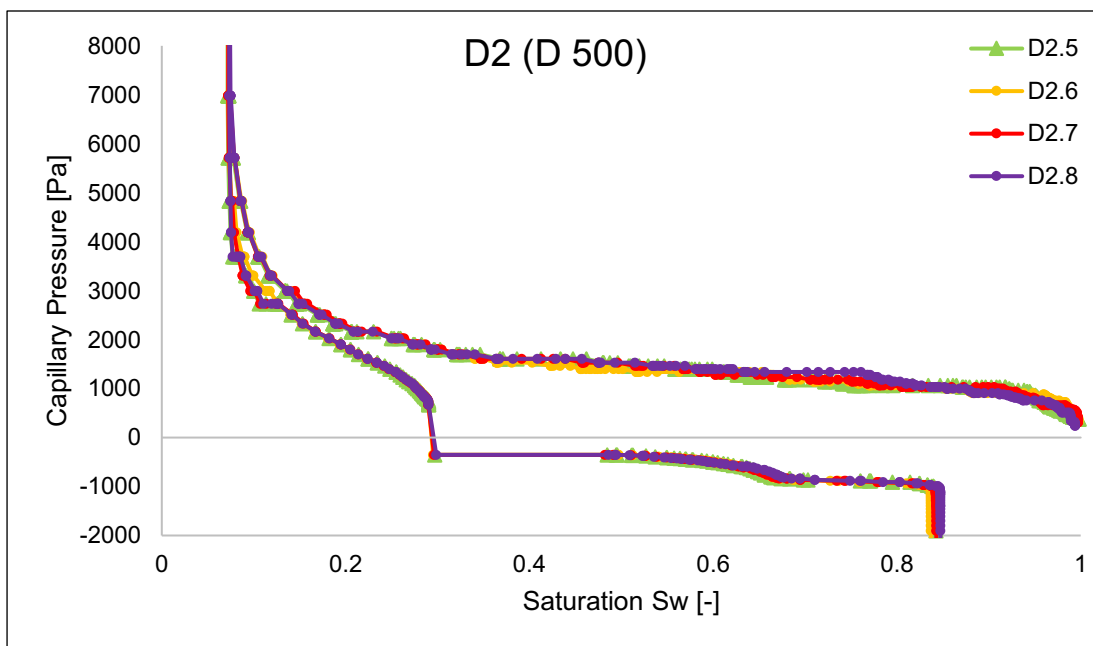


Figure 6-7 Case D, Scenario D2, Results on structure D 500.